Freeze-Cast Porous Ceramics: Tailoring Chemistry and Porosity for Functionality

Thesis by

Laura K. Quinn

In Partial Fulfillment of the Requirements for

the Degree of

Doctor of Philosophy of Chemistry

CALIFORNIA INSTITUTE OF TECHNOLOGY

Pasadena, California

2024

Defended May 14th, 2024

Laura K. Quinn

ORCID: 0000-0002-6112-028X

ACKNOWLEDGEMENTS

I am incredibly fortunate to have had the help and support of so many wonderful people both at Caltech and beyond. While it wouldn't be possible to list each and every person who has helped me in reaching this point, I am grateful to them all.

First and foremost, I would like to thank my advisor, Professor Katherine Faber, for everything she's done for me in the past five years. Without her continuous and generous guidance and support, I would not have been able to grow into the scientist I am today, and her patience, trust in my ability to multitask, and advice has been invaluable along this journey.

Next, a huge thank you to my committee members, Prof. Kimberly See, Prof. Harry Gray, and Prof. Julia Kornfield for being on my thesis and candidacy committees, for reviewing my thesis, and finally for their boundless enthusiasm and invaluable advice and encouragement.

This research would not have been possible without the help of the many fantastic collaborators I've been lucky enough to work with over the past five years. First, a huge thank you to Prof. George Rossman, not only for letting me monopolize the Raman spectrometer in his lab for over two years, but also for his assistance with any question I took to him and for his enthusiasm for exploring interesting questions. Our collaborators at the University of Central Florida and Embry-Riddle Aeronautical University, Prof. Seetha Raghavan, Dr. Remelisa Esteves, and Perla Latorre-Suarez, who allowed us access to their instrumentation, were incredibly generous with their time, and kindly invited me to tour their new facilities at ERAU! Thanks also to our collaborators at the Jet Propulsion Laboratory, Nataly Chen and Araseli Cortez, for their assistance with experimentation and advice. Finally, much of this research was done in collaboration with some of the talented researchers at Caltech: Prof. Julie Kornfield and Prof. Victoria Orphan, Prof. Kriti Sharma, Dr. Yamini Jangir and Prof. Paresh Samantary, and Alex Johnson, Rebecca Wipfler, and Sergio Parra. A huge thank you especially to Prof. Kriti Sharma, for sharing her expertise and for her mentorship, and to the Orphan group and Prof. Orphan for their invitation to their cruise on the R.V. Yellowfin.

I would also like to acknowledge the funding sources that enabled this research: the President's and Director's Research and Development Fund from JPL and Caltech, the Donna and Benjamin M. Rosen Bioengineering Center Pilot Research Grant Program, and the Caltech Division of Engineering and Applied Sciences' Clinard Innovation Fund.

An enormous thank you must also go to the many wonderful members of the Faber Group during my time here, for their support, advice, and friendship: Dr. Noriaki Arai, Dr. Claire Kuo, Dr. Benjamin Herren, Dr. Celia Chari, Dr. Vince Wu, Kevin Yu, Sara Gorske, Zac Ahmad, Seneca Velling, Wes Patel, Tomas Grossmark, Mahi Gokuli, Shivani Chatterji, Juan Arvelo, Finn Sutcliffe, and Nyvia Lyles, Alice Kutsyy, and Ankita Nandi, the three phenomenal undergraduate researchers who I have been lucky enough to supervise.

None of this work would have been possible without the tireless work of Caltech's administrative staff, including Christy Jenstad, Katie Pichotta, Alison Ross Keller, Jennifer Blankenship, and Mabby Howard. Thank you to Christy and Katie, especially, not only for their help with administration, but also for their genuine support, encouragement, care, and friendship throughout these past five years.

I would also like to thank Dr. Chi Ma from Geological and Planetary Sciences, Dr. Giada Spigolon from the Caltech Biological Imaging Facility, and Nate Hart from the CCE Glass Shop for their assistance with instrumentation and for their generosity with their time.

I am also grateful to all of the staff at the Hixon Writing Center for their useful resources and help, and a particularly enormous thank you must go to Dr. Erin Burkett, who read each chapter of this thesis in its roughest draft form and helped me shape my disorganized thoughts into something more comprehensible.

Thank you to the many wonderful friends I've made at and beyond Caltech—my friends from Rice Chemistry and Sid Rich, my Caltech Chemistry cohort, my fellow Women in Chemistry board members, and the members of Caltech's Glee Club and Chamber Singers. Your friendships and support have made the last five years possible.

Lastly, thank you to my family: to the extended Wagner, Quinn, Dry, and Sparrow families, for always finding more room at the table. To my wonderful aunts, uncles, and cousins, who always make holidays a joy. To my grandparents, Bob, Jane, Sharon, and Chick, thank you for your endless love and support. To my brother, Jack, thank you for always providing a fresh perspective and a laugh. And finally, an enormous thank you to my parents, Alison and Jim. Nobody has ever believed in me as much as you have, and I never would have been able to reach this point without you.

—Laura

ABSTRACT

Porous ceramics have been created and utilized in applications ranging from the automotive industry to biomedical research, with the chemical and pore characteristics of these ceramic structures crucial to their function and design. In this work, these intertwined factors are explored for a variety of applications by controlling the chemistry through precursor preparation and heat treatments, and the porosity controlled through freeze casting, a tunable and facile pore-forming technique yielding a range of pore sizes and morphologies. First, shape memory and superelastic behaviors in ceria-doped zirconia are observed by creating porous honeycomb structures that can accommodate the volume change of the martensitic transformation enabling such performance. By controlling dopant concentration, powder morphology, and freezing rate, the martensitic transformation is tracked over multiple cycles and collection volumes in these bulk-scale, polycrystalline zirconia ceramics. Next, transparent porous model sediments are created through heat treatments of freeze-cast synthetic cryolite (Na_3AlF_6) powder. Fluorescent beads the same size as many bacterial cells are visualized in a range of pore morphologies over both depth and time, and these porous ceramics are deployed in a sedimentary environment and the imaging of the microbial communities contained within and are found to colonize the porous cryolite structures. Alternate porous habitats for bacterial colonization are further created using materials such as iron oxides and carbon nanotubes to produce structures that can act both as electron acceptors and as microbial habitats. Finally, thermally anisotropic Si-based porous ceramics are developed with a potential use in optical devices. Using two contrasting preceramic polymers and both traditional and UV-assisted freeze-casting techniques, porous SiOC is produced from preceramic polymers with differing carbon contents. Together, these examples explore how the chemistry and porosity of porous ceramics can be manipulated to affect the chemical, optical, mechanical, and thermal properties of ceramic structures to best suit the intended function.

PUBLISHED CONTENT AND CONTRIBUTIONS

L.K. Quinn*, R. Esteves, P. Latorre-Suárez, G.R. Rossman, S. Ragahavan, and K.T. Faber (n.d). Shape Memory and Superelasticity in Polycrystalline Ceria-Stabilized Zirconia Honeycombs. In: *In Revision.*

L.K.Q. led the experimental work and the writing of the manuscript.

L.K. Quinn*, K. Sharma*, V.J. Orphan, and K.T. Faber (n.d.). Transparent Porous Cryolite for *In-Situ* Observation of Bacterial Populations. In: *In Preparation.*

L.K.Q. prepared and analyzed cryolite coupons and performed transparency and bead movement assessments, and co-first authored the manuscript.

L.K. Quinn*, K. Sharma, V.J. Orphan, and K.T. Faber (n.d.). Two-stage Sintering to Produce Transparent Porous Cryolite from Synthetic Cryolite Powder. In: *In Preparation.*

L.K.Q. led the experimental work and the writing of the manuscript.

TABLE OF CONTENTS

LIST OF ILLUSTRATIONS

Number *Page*

LIST OF TABLES

Chapter 1

INTRODUCTION AND BACKGROUND

1.1. Background

Ceramics, critical materials in modern industries ranging from homewares to aerospace equipment, have been in use by humans from as early as 26000 BCE[1–3]. However, the range of chemical compositions of ceramic materials and the role of porosity in ceramic structures has varied greatly over that time. The chemical composition of early ceramics was determined by the clays available, and thus varied across regions[4,5]. Likewise, the degree of chemical transformation and densification a ceramic material experienced on firing was dependent on the available furnace technology: as high-temperature heating systems evolved from early pit-firing techniques to the electric kilns and furnaces of today and higher temperatures were able to be reached, new ceramic materials requiring higher firing temperatures could be produced[6,7]. Similarly, improvements in purification technologies, development of techniques to precisely control dopants, and modern nanofabrication capabilities have all enabled more precise control of the chemistry of pure, doped, and composite ceramic materials[8–10].

In both early and modern ceramics, these factors—the materials available and the firing temperatures used—also control the porosity of the final ceramic body. The presence or absence of pore-forming materials such as trapped gasses, residual organics, or additives influences the porosity of the final fired ceramics[11]. Similarly, increasing sintering temperatures has been shown to decrease porosity, and thus firing temperature can also act as a lever to tune ceramic porosity[12]. As processing techniques including templating, additive manufacturing, and nanofabrication have developed, utilization of these techniques allows for even more control over the porosity of ceramics materials[9, 13–17].

Although pores are viewed as a defect to be avoided in some modern ceramics, other ceramic materials not only permit porosity, but in fact rely upon it to ensure functionality of the final ceramic. Porous ceramics have been utilized in applications including filters, membranes, scaffolds, and more[18–21]. In all of these applications, both the chemical composition of the ceramic and the pore size, fraction, and morphology are crucial to the ceramic's suitability for the intended application, and it is necessary to control each of these aspects to produce the desired functional materials. By tailoring these two qualities—chemical composition and porosity—together, porous ceramics can be created for applications ranging from aerospace to biological investigations.

1.2. Controlling Ceramic Chemistry

Controlling the chemical composition of a ceramic structure begins with selection of the material. Ceramics encompass a wide range of materials, including oxides, nitrides, fluorides, silicates, and carbides[14, 22–25]. The mechanical, optical, thermal, and chemical properties of the desired final product must be considered when choosing a chemical composition—for example, an oxide such as ZrO_2 is capable of operating at much higher temperatures than CaF_2 but has a lower thermal conductivity (Figure 1.1) [26–29]. The specific properties of the chosen ceramic dictate the conditions in which it is able to be used, and so careful selection of the ceramic ensures a match between chemical content and application.

Ceramics can be produced either from precursors that chemically transform into the final ceramic or simply from the same material as that of the final product. The particle size, particle shape, and functionality of ceramic precursors and materials can also be tuned in order to ensuring the correct ceramic properties. Nanofabrication techniques have also been used to produce ceramics including microarchitectured SiOC and electrospun ceramic nanofibers, among others, or else to produce ceramic nanoparticles in a range of shapes[16, 17, 30]. Ceramics can also be synthesized as

colloids or as single crystals[31, 32]. Finally, functionalizing the surface of ceramic particles provides another way to more finely tune the ceramic chemistry[33].

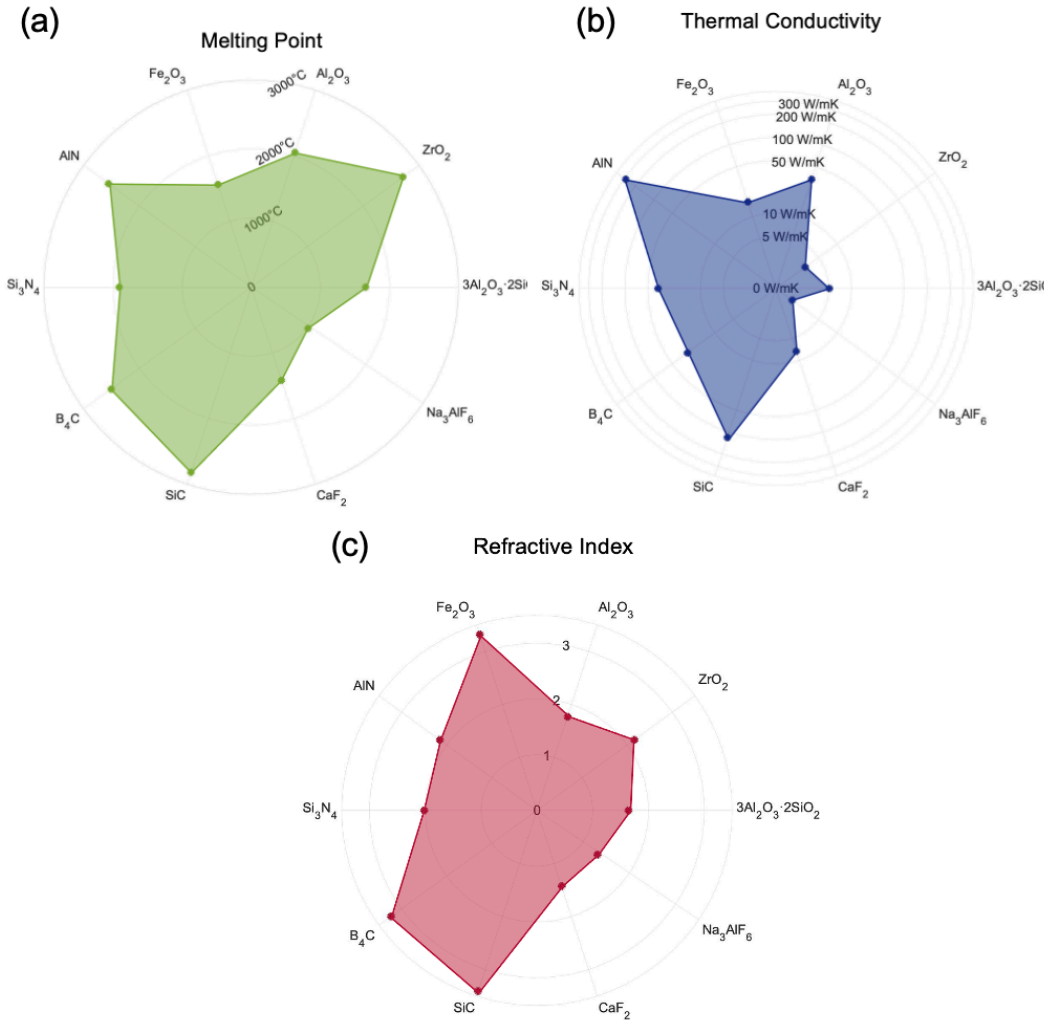

Figure 1.1. Selected ceramics' (ZrO_2, Al_2O_3, Fe_2O_3, AlN, Si_3N_4, B_4C, SiC, CaF_2, Na_3AlF_6, and $3Al_2O_3·2SiO_2$) (a) melting points, (b) thermal conductivities, and (c) refractive indices[28–48].

Precursors to the desired final ceramic can also be used in ceramic synthesis techniques, and this work will explore two such examples of utilizing precursors to

control ceramic chemistry: sol-gel preparation of oxide powders, and use of preceramic polymers. Techniques such as these provide an advantage over simply mixing constituent species together, which often leads to inhomogeneous distribution of component species[51]. Sol-gel synthesis techniques allow for atomistic mixing of multiple different species by trapping homogeneously distributed compounds in a gel[55,56]. In these processes, atomistically mixed precursors in a liquid solution are transformed first through hydrolysis and condensation reactions into first sols (colloidal suspensions) and then through polycondensation processes into gels, where a solid network permeates through a fluid (Figure 1.2) [51, 53]. Finally, continued heating of the gel ensures complete expulsion of the solvent from the gel network, and calcination is used to transform the atomistically mixed precursors into homogeneous ceramics or inorganic polymers[53].

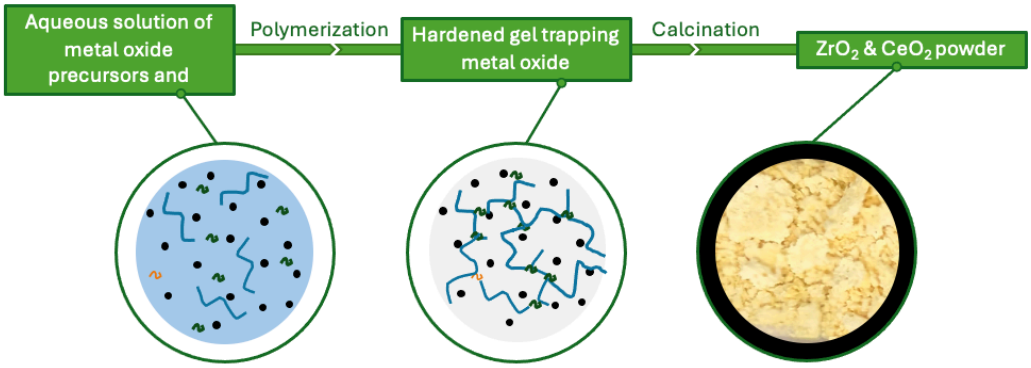

Figure 1.2. Schematic of sol-gel synthesis method to produce atomistically mixed ZrO_2 - CeO_2 powders.

A variety of precursors and polymerization mechanisms can be used to produce gels, resulting in gels connected by bonds ranging in strength from Van der Waals interactions to covalent bonds of polymer networks[53–58]. Factors such as solution pH and concentrations of complexing agents further impact the chemical structure of the gel and the shape of the resulting particles[59–61]. For example, increasing the pH of the solution or the concentration of a complexing agent to polymer precursor in a

Pechini-style synthesis will shift the mechanism of gel growth from a spinodal decomposition mechanism to a nucleation mechanism (Figure 1.3) [60]. Through these compositional and morphological controls, sol-gel syntheses act not only as techniques to produce homogeneous mixtures, but also control the size and shape of the ceramic powders produced.

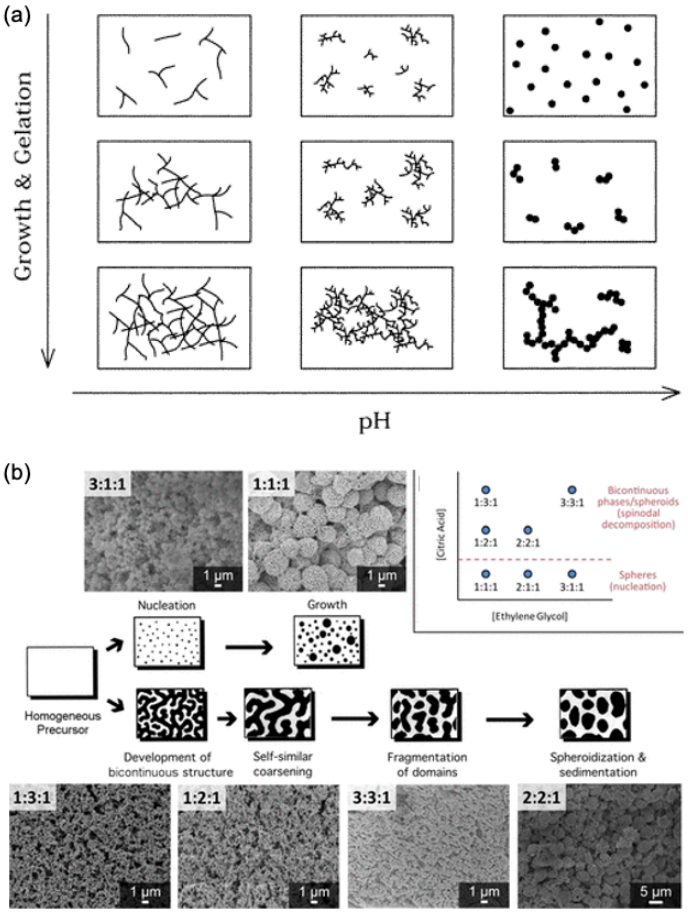

Figure 1.3. Growth mechanisms in sol-gel syntheses. (a) Growth mechanisms shift from spinodal decomposition to nucleation as pH increases, reprinted from Cushing et al. with permission, © 2004, The American Chemical Society[59]. Original figure from Gallagher and Ring, © 1996, the Swiss Chemical Society[62]. (b) Different growth mechanisms and resulting particle morphologies from sol-gel syntheses with differing ratios of chelating agent (citric acid) to polymer precursor (ethylene glycol), reprinted from Rudisill et al. with permission, © 2013, The American Chemical Society[60].

Use of preceramic polymers in ceramic processing methods presents another method through which ceramic chemistries can be controlled. These polymers, which have been studied since the 1970s, transform on pyrolysis into robust ceramics and allow for easier shaping of the preceramic materials using well-defined polymer manipulation strategies such as injection molding, extrusion, and spray-coating[63–65]. Once formed, the material can be transformed through pyrolysis into a ceramic, producing ceramic structures at temperatures that are typically much lower than the sintering temperature of the final product[66]. Organosilicon preceramic polymers, a commonly used class of preceramic polymer, have been utilized in applications ranging from biomedical scaffolds to membranes and catalyst supports[67–69]. The variety of organosilicon preceramic polymers available gives rise to a range of silicon-based ceramic chemistries (Figure 1.4), many of which require high-temperature processing to produce the desired ceramic simply from the raw materials. Instead, preceramic polymers can be fired at lower temperatures, and enable fabrication of ceramic structures through techniques such as tape casting, additive manufacturing, injection molding, and more[63, 70, 71].

Whether or not precursor compounds are used during processing, the temperature and atmosphere in which the ceramics are fired also affect ceramic chemistries, by way of the reactions that take place during heating. One such possible mechanism that can occur during heating is sintering, in which particles fuse and densify into a stronger structure[72]. Either heat or a combination of heat and pressure can be used to sinter unfired green bodies into dense, strengthened ceramics, but it is crucial to keep the material from reaching its melting point[72]. Multiple atomistic mechanisms including surface diffusion, lattice diffusion, and grain boundary diffusion can contribute to solid-state sintering processes, and sintering can occur in air or in inert atmospheres[12, 73, 74]. In contrast, pyrolysis processes, which consist of thermolysis reactions in which a precursor decomposes into a new compound, can sometimes be used to produce robust ceramic materials[75]. Generally, pyrolysis reactions occur in inert atmospheres. Calcination, in which a material is decomposed in air atmosphere

serves as a reactive-atmosphere counterpoint to pyrolysis[76]. In calcination reactions, volatile substances are removed, and/or some amount of mass is oxidized to form the final product[76]. Lastly, ceramic chemistry can also be altered by heat treating ceramics in oxidizing or reducing environments to produce alternative chemical structures from the unfired ceramic precursors[77]. In this work, these techniques will be utilized separately or in sequence to produce specific ceramic compositions, with the specific process used depending on the desired final ceramic.

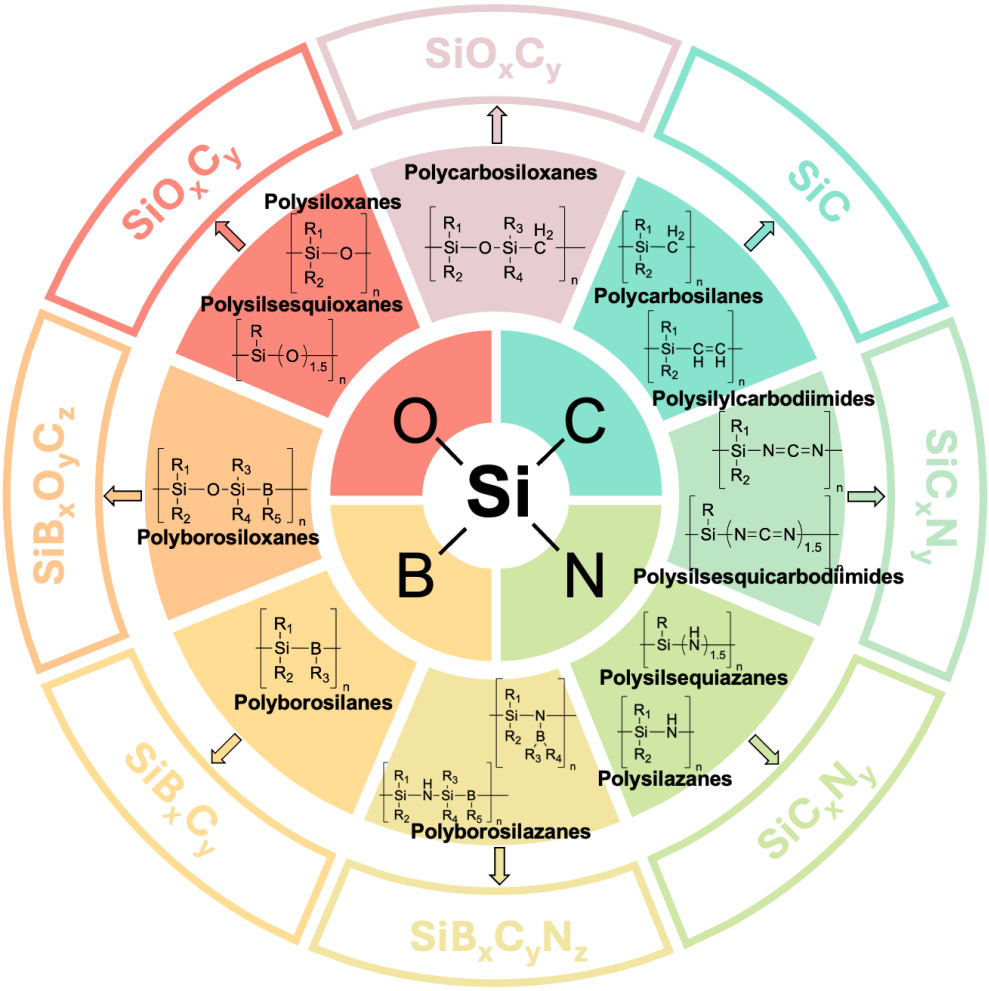

Figure 1.4. Organosilicon preceramic polymers with oxygen-, carbon-, nitrogen-, and boron-containing backbones, adapted from Colombo et al. with permission, ©2010, The American Ceramic Society[66].

Finally, the composition of ceramic materials can be altered both before and after firing through the incorporation of additional materials such as polymeric coatings or creation of ceramic nanocomposites[78–80]. These methods can adjust the surface charge of the ceramic, alter the optical, thermal, or electrical properties, and/or provide catalytic surfaces within ceramic supports. Whether the ceramic is left unaltered before, during, or after firing, however, the chemistry can be better understood through a variety of spectroscopic techniques, some of which will be further explored in this work. Through understanding and controlling the specific chemistries at play, ceramics that are well-suited to the desired application can be produced. It is not enough to simply control the chemistry of the ceramic structures produced, however: porosity, too, must be understood and coordinated to the desired use.

1.3. Controlling Ceramic Porosity

Through much of the history of ceramics, porosity was deemed a source of failure and was avoided at all costs. Some modern advanced ceramics require as few pores as possible, such as artificial joints—in which pores can act as a mechanical defect—and ceramics used in lasers—in which pores reduce optical transmission and thus efficiency[81, 82]. However, many advanced ceramics today not only incorporate, but require pores for functionality. Porous ceramics are widely utilized and studied as biomedical implants, membranes, filters, catalyst supports, and more[19, 67, 68, 83–86].

These pores can be created through a range of techniques, including additive manufacturing, direct foaming, replica methods, and sacrificial templating (Figure 1.5), each suited best to different applications and desired pore characteristics[87]. Additive manufacturing, for example, produces complex and precise microstructures (Figure 1.5a) but can be time-consuming and produce poor surface finishes[15, 88]. Direct foaming methods (Figure 1.5b) produce porous materials quickly and cheaply by bubbling gases into a ceramic or precursor suspension, with the resultant porosity a function of the amount of gas incorporated[87]. However, the suspensions must be

stabilized in order to preserve porosity, and this technique only produces spherical pores[89–92].

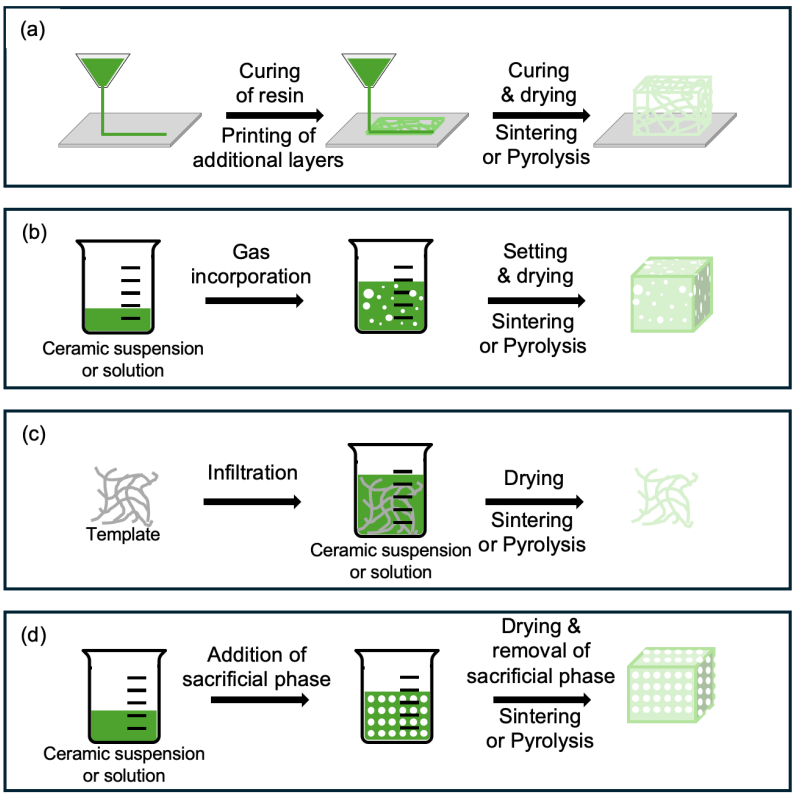

Figure 1.5. Schematics of (a) direct ink writing, (b) direct foaming, (c) replica, and (d) sacrificial templating methods of producing porous ceramics, adapted from Studart et al. with permission, © 2006, The American Ceramic Society[87].

To produce more complex pore networks, replica methods, in which a cellular structure is infiltrated with a ceramic or precursor slurry, may be used (Figure 1.5c)[87]. These methods can produce more intricate pore morphologies but tend to be limited to production of materials with pores greater than or equal to 200 μm[93]. Conversely, sacrificial templating techniques, in which the pore size depends on the size of the templating material used, allow for fabrication of porous materials with pores ranging from 1-700 μm. In these techniques, an evenly dispersed sacrificial phase is incorporated into the ceramic or precursor material to form a biphasic composite

(Figure 1.5d)[87]. The sacrificial phase is then removed through thermal processes such as pyrolysis or sublimation or through chemical routes such as washing or acidic leaching[94–97]. Not only is a range of pore sizes possible through sacrificial templating techniques, but a range of pore morphologies is also accessible.

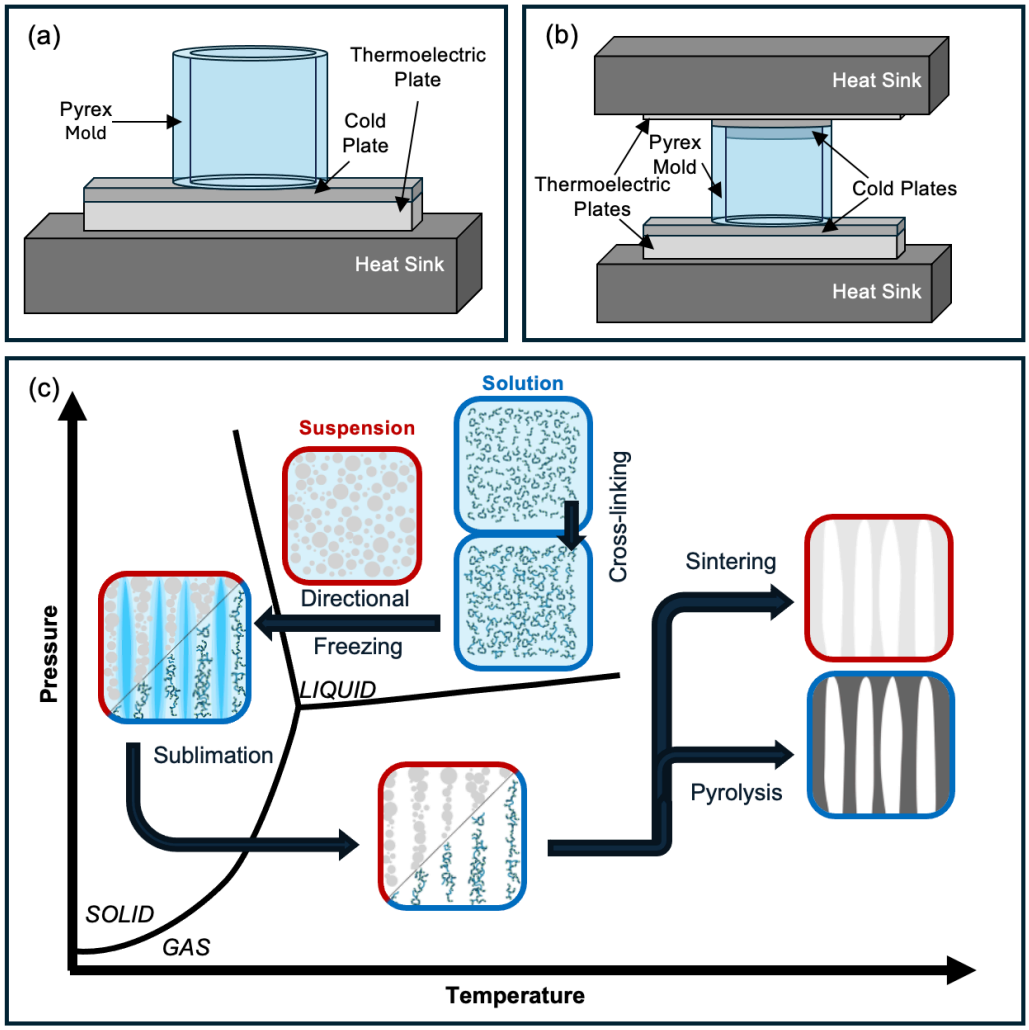

Figure 1.6. Schematics of (a) single-sided, and (b) double-sided freeze casting setups, adapted from Arai et al. with permission, © 2021 Acta Materialia Inc. Published by Elsevier Ltd. All rights reserved.[98]*. (c) Schematic of freeze casting workflow, adapted with permission from Naviroj et al, © 2017, The Materials Research Society*[99]*.*

This work will focus on freeze casting as a fabrication method for porous ceramics, a subcategory of sacrificial templating in which directionally frozen solid solvent crystals comprise as the sacrificial phase and are removed through sublimation[100]. While this technique is popular in the production of porous ceramic materials, it can also be used to create porous metallic or polymeric structures[9, 13, 101]. When considering the preparation of porous ceramics, there are two main classes of freeze casting that this work will focus on: suspension-based freeze casting of ceramic or ceramic precursor slurries, and solution-based freeze casting of preceramic polymers.

In both suspension- and solution-based freeze casting, a liquid suspension or solution is directionally frozen to form solvent crystals. These crystals separate from the suspended or dissolved material through either the rejection of particles from suspension or through phase segregation of the solute from the solvent[78]. The growth rate and morphology of the solvent crystals depend on a number of factors both intrinsic and extrinsic to the suspension or solution used in freezing. Crystal morphology, for example, depends on the relative stability of the interface between the solid and liquid states, and can be predicted through parameters such as the Jackson-α factor[99, 102]. The amount and size of crystals, however, depends upon the ratio of solvent to solute in the freezing liquid[99, 102]. Additionally, the freezing rate and thermal gradients experienced by the solution or suspension during freeze casting also impact the morphology and size of solvent crystals and thus the resulting pores[103–105]. These factors can be controlled through one-sided or two-sided freeze casting apparatuses, as seen in Figure 1.6a and b.

Following freezing, the solvent crystals in the frozen bodies are removed through sublimation, leaving behind the negative impressions of where they once were (Figure 1.6c)[99]. Frequently, binding agents or crosslinkers are incorporated into the initial freeze casting solution to lend mechanical stability to these porous green bodies before sintering or pyrolysis occurs[78]. Following the sublimation of the solvent crystals, the porous structures are sintered (in the case of suspension-based

freeze casting) or pyrolyzed (in the case of solution-based freeze casting with preceramic polymers) to create the final ceramic body.

Freeze casting of ceramics has been utilized over a wide range of industries and technologies, due to the control over the size, shape, and concentration of pores in ceramic structures that the technique affords. In concert with the chemical control discussed earlier, this method of controlling ceramic porosity affords a great deal of tunability of the pore networks in the ceramic structures. Throughout this work, both the chemistry and porosity of porous ceramics will be tuned to yield porous ceramics suited for a range of applications, thereby allowing for the study of phase transformations, bacterial colonization, and thermal properties of porous ceramic materials.

1.4. Thesis Organization

In this thesis, several examples of how the chemistry and porosity of ceramics can be tuned to create functional ceramics well-suited to their intended application are explored. In these examples, the chemistry of each ceramic is controlled not only through selection of the material to best suit the intended function, but also through its processing method. Porosity is controlled in each example through freeze casting, which provides a range of pore morphologies for tailoring to the specific system. Through these explorations, several applications of porous ceramics are explored, and the intertwined relationship between chemistry and porosity of these ceramics is probed and optimized.

The first ceramic system explored is porous ceria-stabilized zirconia ceramics for observation of shape memory and superelastic behaviors. Chapter II develops a rule-of-mixtures approach to quantitatively analyze Raman spectra of these systems so the extent of phase transformation can be tracked, and Chapter III explores shape memory and superelastic behaviors using Raman spectroscopy and X-ray diffraction. In Chapter III, the role of precursor preparation and dopant concentration in the

materials' behavior is explored, and the spectroscopic analysis method developed in Chapter II is utilized to track changes in the phase composition.

Next, sodium hexafluoroaluminate (cryolite) ceramic systems are discussed in Chapter IV as a model transparent soil to probe bacterial colonization. The effect of heat treatments and pore morphologies on the chemical and optical properties of these ceramics is explored to produce transparent, porous, biocompatible materials for deployment in soil microenvironments of interests to geobiologists. Porous ceramics as potential bacterial habitats are further explored in Chapter V with iron oxide and silicon oxycarbide systems. The roles that temperature, atmosphere, and nanoparticle additives play in chemical composition and ceramic porosity are investigated to produce porous materials that can act as electron acceptors as well as habitats for exoelectrogenic microorganisms.

In the last porous ceramic system investigated, porous SiOC is carbothermally reduced to SiC, presented in Chapter VI. Two different ceramic precursors are considered for producing porous SiOC materials that can undergo a carbothermal reduction into SiC. Finally, Chapter VII summarizes each example of porous ceramic systems, and provides suggestions for future research directions and unanswered questions.

1.5. References

1. Heimann, R.B. Classic and Advanced Ceramics: From Fundamentals to Applications. John Wiley & Sons; 2010.
2. Vandiver P.B., Soffer, O., Klima, B., Svoboda, J. The Origins of Ceramic Technology at Dolni Věstonice, Czechoslovakia. *Science*. 1989;246(4933):1002–1008. https://doi.org/10.1126/science.246.4933.1002.
3. Rathod VT, Kumar JS, Jain Anjana. Polymer and ceramic nanocomposites for aerospace applications. *Appl Nanosci*. 2017;7:519–548. https://doi.org/10.1007/s13204-017-0592-9.
4. Diko-Makia, L., Ligege, R. Composition and Technological Properties of Clays for Structural Ceramics in Limpopo (South Africa). *Minerals*. 2020;10(8):700. https://doi.org/10.3390/min10080700.
5. Kagonbé, B.P., Tsozué, D., Nzeukou, A.N., Ngos, S. Mineralogical, Physico-Chemical and Ceramic Properties of Clay Materials from Sekandé and Gashiga (North,

Cameroon) and Their Suitability in Earthenware Production. *Heliyon*. 2021;7(7):e07608. https://doi.org/10.1016/j.heliyon.2021.e07608.
6. McClellan, J.E., Dorn H. Science and Technology in World History: An Introduction. JHU Press; 2006.
7. Kingery, W.D., Vandiver, P.B. Ceramic Masterpieces: Art, Structure, and Technology. Free Press; 1986.
8. Kozerozhets, I.V., Panasyuk, G.P., Semenov, E.A., Avdeeva, V.V., Ivakin, Y.D., Danchevskaya, M.N. New Approach to Prepare the Highly Pure Ceramic Precursor for the Sapphire Synthesis. *Ceram. Int*. 2020;46(18, Part A):28961–28968. https://doi.org/10.1016/j.ceramint.2020.08.067.
9. de Hazan, Y. Porous Ceramics, Ceramic/Polymer, and Metal-Doped Ceramic/Polymer Nanocomposites via Freeze Casting of Photo-Curable Colloidal Fluids. *J Am Ceram Soc*. 2012;95(1):177–187. https://doi.org/10.1111/j.1551-2916.2011.04870.x.
10. Li, P., Chen, I.-W., Penner-Hahn, J.E. Effect of Dopants on Zirconia Stabilization—An X-ray Absorption Study: I, Trivalent Dopants. *J Am Ceram Soc*. 1994;77(1):118–128. https://doi.org/10.1111/j.1151-2916.1994.tb06964.x.
11. Reedy, C.L., Anderson, J., Reedy, T.J. Quantitative Porosity Studies of Archaeological Ceramics by Petrographic Image Analysis. *MRS Proc*. 2017;1656:337–353. https://doi.org/10.1557/opl.2014.711.
12. Leriche, A., Hampshire, S., Cambier, F. Sintering of Ceramics. Elsevier; 2017 https://doi.org/10.1016/B978-0-12-803581-8.10288-7.
13. Chen, R., Wang, C.-A., Huang, Y., Ma, L., Lin, W. Ceramics With Special Porous Structures Fabricated by Freeze-Gelcasting: Using Tert-Butyl Alcohol As a Template. *J Am Ceram Soc*. 2007;90:3478–3484. https://doi.org/10.1111/j.1551-2916.2007.01957.x.
14. Sarraf, F., Churakov, S.V., Clemens, F. Preceramic Polymers for Additive Manufacturing of Silicate Ceramics. *Polymers (Basel)*. 2023;15(22):4360. https://doi.org/10.3390/polym15224360.
15. Villa, A., Gianchandani, P.K., Baino, F. Sustainable Approaches for the Additive Manufacturing of Ceramic Materials. *Ceramics*. 2024;7(1):291–309. https://doi.org/10.3390/ceramics7010019.
16. Brigo, L., Schmidt, J.E.M., Gandin, A., Michieli, N., Colombo, P., Brusatin, G. 3D Nanofabrication of SiOC Ceramic Structures. *Advanced Science*. 2018;5(12):1800937. https://doi.org/10.1002/advs.201800937.
17. Algethami, J.S., Amna, T., S. Alqarni L., Alshahrani, A.A., Alhamami, M.A.M., Seliem, A.F., Al-Dhuwayin, B.H.A., Hassan, M.S. Production of Ceramics/Metal Oxide Nanofibers via Electrospinning: New Insights into the Photocatalytic and Bactericidal Mechanisms. *Materials*. 2023;16(14):5148. https://doi.org/10.3390/ma16145148.
18. Lee, J.-S., Lee, S.-H., Choi, S.-C. Improvement of Porous Silicon Carbide Filters By Growth of Silicon Carbide Nanowires Using a Modified Carbothermal Reduction Process. *J Alloys Compd*. 2009;467(1):543–549. https://doi.org/10.1016/j.jallcom.2007.12.042.
19. Cheng, X., Liang, H., Qu, F., Ding, A., Chang, H., Liu, B., Tang, X., Wu, D., Li, G. Fabrication of Mn Oxide Incorporated Ceramic Membranes for Membrane Fouling

Control and Enhanced Catalytic Ozonation of p-Chloronitrobenzene. *Chem Eng J*. 2017;308:1010–1020. https://doi.org/10.1016/j.cej.2016.09.127.
20. Deville, S., Saiz, E., Tomsia, A.P. Freeze Casting of Hydroxyapatite Scaffolds for Bone Tissue Engineering. *Biomaterials*. 2006;27:5480–5489. https://doi.org/10.1016/j.biomaterials.2006.06.028.
21. da Rosa Braun, P.H., Canuto de Almeida e Silva, T., Rodrigo Quejigo J., Kuchenbuch, A., Rezwan, K., Harnisch, F., Wilhelm, M. Impact of Surface Properties of Porous SiOC-Based Materials on the Performance of Geobacter Biofilm Anodes. *Chem Electro Chem*. 2021;8(5):850–857. https://doi.org/10.1002/celc.202001568.
22. Buannic, L., Naviroj, M., Miller, S.M., Zagorski, J., Faber, K.T., Llordés, A. Dense Freeze-cast $Li_7La_3Zr_2O_{12}$ Solid Electrolytes With Oriented Open Porosity and Contiguous Ceramic Scaffold. *J Am Ceram Soc*. 2019;102(3):1021–1029. https://doi.org/10.1111/jace.15938.
23. Chari, C.S., Faber, K.T. Oxidation Resistance of AlN/BN via Mullite-type $Al_{18}B_4O_{33}$. *J Eur Ceram Soc*. 2022;42(8):3437–3445. https://doi.org/10.1016/j.jeurceramsoc.2022.02.037.
24. Gredin, P., Mortier, M. 4 - Optical Properties of Fluoride Transparent Ceramics. In: Tressaud A, Poeppelmeier K, eds. *Photonic and Electronic Properties of Fluoride Materials*. Boston: Elsevier; 2016:65–87. https://doi.org/10.1016/B978-0-12-801639-8.00004-0.
25.Burns, G.T., Taylor, R.B., Xu, Y., Zangvil, A., Zank, G.A. High-temperature Chemistry of the Conversion of Siloxanes to Silicon Carbide. *Chem Mater*. 1992;4(6):1313–1323. https://doi.org/10.1021/cm00024a035.
26. Gauthier, M., editor. ASM Engineered Materials Reference Book. ASM International; 1994.
27. Lide, D.R. CRC Handbook of Chemistry and Physics: 1998-1999 ; A Ready-Reference Book of Chemical and Physical Data. 79. ed. Boca Raton: CRC Press; 1998.
28. Weast, R.C., Astle, M.J., Beyer, W.H., eds. CRC Handbook of Chemistry and Physics. 64. ed. Boca Raton: CRC Press; 1983.
29. Schneider, Jr., S.J., editor. Engineered Materials Handbook: Ceramics and glasses. ASM International; 1991.
30. Forest, V., Leclerc, L., Hochepied, J.-F., Trouvé, A., Sarry, G., Pourchez, J. Impact of Cerium Oxide Nanoparticles Shape on Their *In-Vitro* Cellular Toxicity. *Toxicology in Vitro*. 2017;38:136–141. https://doi.org/10.1016/j.tiv.2016.09.022.
31. Lewis, J.A. Colloidal Processing of Ceramics. *J Am Ceram Soc*. 2000;83(10):2341–2359. https://doi.org/10.1111/j.1151-2916.2000.tb01560.x.
32. Crystal, I.R., Lai, A., Schuh, C.A. Cyclic Martensitic Transformations and Damage Evolution in Shape Memory Zirconia: Single Crystals vs Polycrystals. *J Am Ceram Soc*. 2020;103(8):4678–4690. https://doi.org/10.1111/jace.17117.
33. Kroll, S. Surface Modification of Ceramic Materials. *Surface-Functionalized Ceramics*. John Wiley & Sons, Ltd; 2023:85–118. https://doi.org/10.1002/9783527698042.ch3.
34. Wood, D.L., Nassau, K. Refractive Index of Cubic Zirconia Stabilized with Yttria. *Appl Opt, AO*. 1982;21(16):2978–2981. https://doi.org/10.1364/AO.21.002978.

35. Munro, M. Evaluated Material Properties for a Sintered alpha-Alumina. *J Am Ceram Soc*. 1997;80(8):1919–1928. https://doi.org/10.1111/j.1151-2916.1997.tb03074.x.
36. Weber, M.J., editor. CRC Handbook of Laser Science & Technology, Vol. 4: Optical Materials, Part 2. Boca Raton, Fla: CRC Press; 1986.
37. Shayganpour, A., Clausi, M., Bayer, I.S. Flexible Hematite (α-Fe2O3)-Graphene Nanoplatelet (GnP) Hybrids with High Thermal Conductivity. *Appl Phys Lett.* 2021;118(9):091903. https://doi.org/10.1063/5.0042404.
38. Querry, M.R. Optical Constants. US Army Armament, Munitions & Chemical Command, Chemical Research; 1985.
39. Pastrňák, J., Roskovcová, L. Refraction Index Measurements on AlN Single Crystals. *Physica Status Solidi (B)*. 1966;14(1):K5–K8. https://doi.org/10.1002/pssb.19660140127.
40. Larruquert, J.I., Pérez-Marín, A.P., García-Cortés, S., Marcos, L.R., Aznárez, J.A., Méndez, J.A. Self-consistent Optical Constants of Sputter-Deposited B_4C Thin Films. *J Opt Soc Am A*. 2012;29(1):117–123. https://doi.org/10.1364/JOSAA.29.000117.
41. Larruquert, J.I., Pérez-Marín, A.P., García-Cortés S., Marcos, L.R., Aznárez, J.A., Méndez, J.A. Self-consistent Optical Constants of SiC Thin Films. *J Opt Soc Am A*. 2011;28(11):2340–2345. https://doi.org/10.1364/JOSAA.28.002340.
42. Munro, R.G. Material Properties of a Sintered α-SiC. *Journal of Physical and Chemical Reference Data*. 1997;26(5):1195–1203. https://doi.org/10.1063/1.556000.
43. Gasch, M.J., Ellerby, D.T., Johnson, S.M. Ultra High Temperature Ceramic Composites. In: Bansal NP, ed. *Handbook of Ceramic Composites*. Boston, MA: Springer US; 2005:197–224. https://doi.org/10.1007/0-387-23986-3_9.
44. Memon, F.A., Morichetti, F., Abro, M.I., Iseni, G., Somaschini, C., Aftab, U., Melloni, A. Synthesis, Characterization and Optical Constants of Silicon Oxycarbide. *EPJ Web Conf*. 2017;139:00002. https://doi.org/10.1051/epjconf/201713900002.
45. Li, H.H. Refractive Index of Alkaline Earth Halides and its Wavelength and Temperature Derivatives. *J Phys Chem Ref Data*. 1980;9(1):161–290. https://doi.org/10.1063/1.555616.
46. Gheribi, A.E., Salanne, M., Chartrand, P. Formulation of Temperature-Dependent Thermal Conductivity of NaF, β-Na_3AlF_6, $Na_5Al_3F_{14}$, and Molten Na_3AlF_6 Supported by Equilibrium Molecular Dynamics and Density Functional Theory. *J Phys Chem C*. 2016;120(40):22873–22886. https://doi.org/10.1021/acs.jpcc.6b07959.
47. Ullmann, F., Gerhartz, W., Yamamoto, Y.S., Campbell, F.T., Pfefferkorn, R., Rounsaville, J.F. Ullmann's Encyclopedia of Industrial Chemistry. 5th ed. Weinheim, Federal Republic of Germany: VCH; 1985.
48. Klein, C., Hurlbut, C.S., Dana, J.D. Manual of Mineralogy. Wiley; 1993.
49. Mahnicka-Goremikina, L., Svinka, R., Svinka. V., Grase, L., Juhnevica, I., Rundans, M., Goremikins, V., Tolendiuly, S., Fomenko, S. Thermal Properties of Porous Mullite Ceramics Modified with Microsized ZrO_2 and WO_3. *Materials*. 2022;15(22):7935. https://doi.org/10.3390/ma15227935.
50. Musikant, S. Development of A New Family Of Improved Infrared (IR) Dome Ceramics. *Emerging Optical Materials*. Vol. 0297. SPIE; 1982:2–12. https://doi.org/10.1117/12.932477.

51. Danks, A.E., Hall, S.R., Schnepp, Z. The Evolution of "Sol–Gel" Chemistry as a Technique for Materials Synthesis. *Mater Horiz*. 2016;3(2):91–112. https://doi.org/10.1039/C5MH00260E.
52. Kakihana, M. "Sol-Gel" Preparation of High Temperature Superconducting Oxides. *J Sol-Gel Sci Techn*. 1996;6(1):7–55. https://doi.org/10.1007/BF00402588.
53. Brinker, C.J., Scherer, G.W. Sol-Gel Science: The Physics and Chemistry of Sol-Gel Processing. Academic Press; 2013.
54. Avnir, D., Coradin, T., Lev, O., Livage, J. Recent Bio-Applications of Sol–Gel Materials. *J Mater Chem*. 2006;16(11):1013–1030. https://doi.org/10.1039/B512706H.
55. Haijun, Z., Xiaolin, J., Yongjie, Y., Zhanjie, L., Daoyuan, Y., Zhenzhen, L. The Effect of the Concentration of Citric Acid and pH Values on the Preparation of $MgAl_2O_4$ Ultrafine Powder by Citrate Sol–Gel Process. *Mater Res Bull.* 2004;39(6):839–850. https://doi.org/10.1016/j.materresbull.2004.01.006.
56. Pechini, M.P. Method of Preparing Lead and Alkaline Earth Titanates and Niobates and Coating Method Using the Same to Form a Capacitor. United States US3330697A. 1967.
57. Lin, J., Yu, M., Lin, C., Liu, X. Multiform Oxide Optical Materials via the Versatile Pechini-Type Sol−Gel Process: Synthesis and Characteristics. *J Phys Chem C*. 2007;111(16):5835–5845. https://doi.org/10.1021/jp070062c.
58. Hall, S.R. Biomimetic Synthesis of High-Tc, Type-II Superconductor Nanowires. *Adv Mater.* 2006;18(4):487–490. https://doi.org/10.1002/adma.200501971.
59. Cushing, B.L., Kolesnichenko, V.L., O'Connor, C.J. Recent Advances in the Liquid-Phase Syntheses of Inorganic Nanoparticles. *Chem Rev*. 2004;104(9):3893–3946. https://doi.org/10.1021/cr030027b.
60. Rudisill, S.G., Hein, N.M., Terzic, D., Stein, A. Controlling Microstructural Evolution in Pechini Gels through the Interplay between Precursor Complexation, Step-Growth Polymerization, and Template Confinement. *Chem Mater*. 2013;25(5):745–753. https://doi.org/10.1021/cm303761z.
61. Sakka, S. Handbook of Sol-Gel Science and Technology. 1. Sol-gel processing. Springer Science & Business Media; 2005.
62. Gallagher, D., Ring, T. Sol-Gel Processing of Ceramic Films. *Chimia*. 1989;43(10):298–304.
63. Zhang, T., Evans, J.R.G., Woodthorpe, J. Injection Moulding of Silicon Carbide Using an Organic Vehicle Based on a Preceramic Polymer. *J Eur Ceram Soc.* 1995;15(8):729–734. https://doi.org/10.1016/0955-2219(95)00049-Z.
64. Mutsuddy, B.C. Use of Organometallic Polymer for Making Ceramic Parts by Plastic Forming Techniques. *Ceram Int*. 1987;13(1):41–53. https://doi.org/10.1016/0272-8842(87)90037-X.
65. Goerke, O., Feike, E., Heine, T., Trampert, A., Schubert, H. Ceramic Coatings Processed by Spraying of Siloxane Precursors (Polymer-Spraying). *J Eur Ceram Soc*. 2004;24(7):2141–2147. https://doi.org/10.1016/S0955-2219(03)00362-5.
66. Colombo, P., Mera, G., Riedel, R., Sorarù, G.D. Polymer-Derived Ceramics: 40 Years of Research and Innovation in Advanced Ceramics. *J Am Ceram Soc*. 2010;93(7):1805–1837. https://doi.org/10.1111/j.1551-2916.2010.03876.x.
67. Yang, Y., Kulkarni, A., Soraru, G.D., Pearce, J.M., Motta, A. 3D Printed SiOC(N) Ceramic Scaffolds for Bone Tissue Regeneration: Improved Osteogenic Differentiation

of Human Bone Marrow-Derived Mesenchymal Stem Cells. *Int J Mol Sci*. 2021;22(24):13676. https://doi.org/10.3390/ijms222413676.
68. Dong, B.-B., Wang, F.-H., Yang, M.-Y., Yu, J.-L., Hao, L.-Y., Xu, X., Wang, G., Agathopoulos, S.. Polymer-Derived Porous SiOC Ceramic Membranes for Efficient Oil-Water Separation and Membrane Distillation. *J Membr Sci*. 2019;579:111–119. https://doi.org/10.1016/j.memsci.2019.02.066.
69. Schumacher, D., Wilhelm, M., Rezwan, K. Porous SiOC Monoliths with Catalytic Activity by *In-Situ* Formation of Ni Nanoparticles in Solution-Based Freeze Casting. *J Am Ceram Soc.* 2020;103(5):2991–3001. https://doi.org/10.1111/jace.16988.
70. Cromme, P., Scheffler, M., Greil, P. Ceramic Tapes from Preceramic Polymers. *Adv Eng Mater*. 2002;4(11):873–877. https://doi.org/10.1002/1527-2648(20021105)4:11<873::AID-ADEM873>3.0.CO;2-G.
71. Mott, M., Evans, J.R.G. Solid Freeforming of Silicon Carbide by Inkjet Printing Using a Polymeric Precursor. *J Am Ceram Soc.* 2001;84(2):307–13. https://doi.org/10.1111/j.1151-2916.2001.tb00655.x.
72. Kingery, W.D., Bowen, H.K., Uhlmann, D.R. Introduction to Ceramics. Wiley; 1976.
73. Plucknett, K.P., Lin, H.-T. Sintering Silicon Nitride Ceramics in Air. *J Am Ceram Soc.* 2005;88(12):3538–3541. https://doi.org/10.1111/j.1551-2916.2005.00631.x.
74. Li, H., Liu, Y., Liu, Y., Zeng, Q., Hu, K., Lu, Z., Liang, J. Effect of Sintering Temperature in Argon Atmosphere on Microstructure and Properties of 3D-Printed Alumina Ceramic Cores. *J Adv Ceram*. 2020;9(2):220–231. https://doi.org/10.1007/s40145-020-0362-0.
75. Soltes, E.J., Elder, T.J. Pyrolysis. *Organic Chemicals From Biomass*. CRC Press; 1981.
76. Rand, B. Calcination. In: Brook R, ed. *Concise Encyclopedia of Advanced Ceramic Materials*. Oxford: Pergamon; 1991:49–51. https://doi.org/10.1016/B978-0-08-034720-2.50023-X.
77. Colomer, M.T., Simenas, M., Banys, J., Vattier, F., Gagor, A., Maczka, M. Effect of Sintering Under $CO+N_2/H_2$ and CO_2+Air Atmospheres on the Physicochemical Features of a Commercial Nano-YSZ. *J Alloys Compd.* 2022;904:163976. https://doi.org/10.1016/j.jallcom.2022.163976.
78. Arai, N. Freeze Casting of Ceramics: Pore Design from Solidification Principles. Ph.D.; California Institute of Technology; 2021 https://doi.org/10.7907/3rmr-cz93.
79. Bateman, O.C.L. Design and Application of Novel Membrane Materials. Ph.D.; California Institute of Technology; 2022 https://doi.org/10.7907/9w23-ax66.
80. Kuo, C.T., Faber, K.T. Permeable Carbon Nanotube-Reinforced Silicon Oxycarbide via Freeze Casting with Enhanced Mechanical Stability. *J Eur Ceram Soc*. 2020;40(6):2470–2479. https://doi.org/10.1016/j.jeurceramsoc.2019.12.059.
81. Messing, G.L., Stevenson, A.J. Toward Pore-Free Ceramics. *Science*. 2008;322(5900):383–384. https://doi.org/10.1126/science.1160903.
82. Ikesue, A., Aung, Y.L., Taira, T., Kamimura, T., Yoshida, K., Messing, G.L. Progress in Ceramic Lasers. *Ann Rev Mater Res.* 2006;36(Volume 36, 2006):397–429. https://doi.org/10.1146/annurev.matsci.36.011205.152926.

83. Jia, C., Liu, Y., Li, L., Song, J., Wang, H., Liu, Z., Li, Z., Li, B., Fang, M., Wu, H. A Foldable All-Ceramic Air Filter Paper with High Efficiency and High-Temperature Resistance. *Nano Lett*. 2020. https://doi.org/10.1021/acs.nanolett.0c01107.
84. Keller, N., Pham-Huu, C., Roy, S., Ledoux, M.J., Estournes, C., Guille, J. Influence of the Preparation Conditions on the Synthesis of High Surface Area SiC for Use as a Heterogeneous Catalyst Support. *J Mater Sci.* 1999;34(13):3189–3202. https://doi.org/10.1023/A:1004681806843.
85. Konegger, T., Williams, L.F., Bordia, R.K. Planar, Polysilazane-Derived Porous Ceramic Supports for Membrane and Catalysis Applications. *J Am Ceram Soc*. 2015;98(Copyright (C) 2020 American Chemical Society (ACS). All Rights Reserved.):3047–3053. https://doi.org/10.1111/jace.13758.
86. Barrow, M., Eltmimi, A., Ahmed, A., Myers, P., Zhang, H. Frozen Polymerization for Aligned Porous Structures with Enhanced Mechanical Stability, Conductivity, and as Stationary Phase for HPLC. *J Mater Chem*. 2012;22:11615–11620. https://doi.org/10.1039/c2jm31425h.
87. Studart, A.R., Gonzenbach, U.T., Tervoort, E., Gauckler, L.J. Processing Routes to Macroporous Ceramics: A Review. *J Am Ceram Soc*. 2006;89:1771–1789. https://doi.org/10.1111/j.1551-2916.2006.01044.x.
88. Zhang, F., Li, Z., Xu, M., Wang, S., Li, N., Yang, J. A Review of 3D Printed Porous Ceramics. *J Eur Ceram Soc*. 2022;42(8):3351–3373. https://doi.org/10.1016/j.jeurceramsoc.2022.02.039.
89. Sepulveda, P. Gelcasting Foams for Porous Ceramics. *Am Ceram Soc Bull*. 1997;76(10):61–65.
90. Saggio-Woyansky, J., Scott, C., Minnear, W.P. Processing of Porous Ceramics. *Am Ceram Soc Bull*. 1992.
91. Innocentini, M.D.M., Sepulveda, P., Salvini, V.R., Pandolfelli, V.C., Coury, J.R. Permeability and Structure of Cellular Ceramics: A Comparison between Two Preparation Techniques. *J Am Ceram Soc.* 1998;81(12):3349–3352. https://doi.org/10.1111/j.1151-2916.1998.tb02782.x.
92. Colombo, P., Hellmann, J.R. Ceramic Foams from Preceramic Polymers. *Mater Res Innov*. 2002;6(5–6):260–272. https://doi.org/10.1007/s10019-002-0209-z.
93. Lange, F.F., Miller, K.T. Open-cell, Low-density Ceramics Fabricated from Reticulated Polymer Substrates. *Adv Ceram Mater.* 1987;2:4. https://doi.org/10.1111/j.1551-2916.1987.tb00156.x.
94. Colombo, P., Bernardo, E., Biasetto, L. Novel Microcellular Ceramics from a Silicone Resin. *J Am Ceram Soc*. 2004;87(1):152–154. https://doi.org/10.1111/j.1551-2916.2004.00152.x.
95. Fukasawa, T., Deng, Z.-Y., Ando, M., Ohji, T., Kanzaki, S. Synthesis of Porous Silicon Nitride with Unidirectionally Aligned Channels Using Freeze-Drying Process. *J Am Ceram Soc*. 2002;85(9):2151–2155. https://doi.org/10.1111/j.1151-2916.2002.tb00426.x.
96. Fitzgerald, T.J., Michaud, V.J., Mortensen, A. Processing of Microcellular SiC Foams. *J Mater Sci*. 1995;30(4):1037–1045. https://doi.org/10.1007/BF01178442.
97. Kim, H., da Rosa, C., Boaro, M., Vohs, J.M., Gorte, R.J. Fabrication of Highly Porous Yttria-Stabilized Zirconia by Acid Leaching Nickel from a Nickel-Yttria-

Stabilized Zirconia Cermet. *J Am Ceram Soc*. 2002;85(6):1473–1476. https://doi.org/10.1111/j.1151-2916.2002.tb00299.x.
98. Arai, N., Stan, T., Macfarland, S., Voorhees, P., Muyanja, N., Shahani, A., Faber, K.T. Coarsening of Dendrites in Solution-based Freeze-cast Ceramic Systems. *Acta Mater*. 2021;215:117039. https://doi.org/10.1016/j.actamat.2021.117039.
99. Naviroj, M., Voorhees, P.W., Faber, K.T. Suspension- and Solution-Based Freeze Casting for Porous Ceramics. *J Mater. Res*. 2017;32(17):3372–3382. https://doi.org/10.1557/jmr.2017.133.
100. Deville, S.. Freeze-casting of Porous Ceramics: A Review of Current Achievements and Issues. *Adv Eng Mater*. 2008;10:155–169. https://doi.org/10.1002/adem.200700270.
101. Chino, Y., Dunand, D.C. Directionally Freeze-cast Titanium Foam with Aligned, Elongated Pores. *Acta Mater*. 2007;56:105–113. https://doi.org/10.1016/j.actamat.2007.09.002.
102. Naviroj, M., Miller, S.M., Colombo, P., Faber, K.T. Directionally Aligned Macroporous SiOC via Freeze Casting of Preceramic Polymers. *J Eur Ceram Soc.* 2015;35(8):2225–2232. https://doi.org/10.1016/j.jeurceramsoc.2015.02.013.
103. Arai, N., Faber, K.T. Hierarchical Porous Ceramics via Two-stage Freeze Casting of Preceramic Polymers. *Scr Mater*. 2019;162:72–76. https://doi.org/10.1016/j.scriptamat.2018.10.037.
104. Arai, N., Faber, K.T. Freeze-Cast Honeycomb Structures via Gravity-Enhanced Convection. *J Am Ceram Soc*. 2021;104(9):4309–4315. https://doi.org/10.1111/jace.17871.
105. Arai, N., Faber, K.T. Gradient-Controlled Freeze Casting of Preceramic Polymers. *J Eur Ceram Soc*. 2023;43(5):1904–1911. https://doi.org/10.1016/j.jeurceramsoc.2022.12.016.

Chapter 2

RAMAN SPECTROSCOPY FOR ANALYSIS OF MONOCLINIC AND TETRAGONAL PHASE CONTENT IN CERIA-STABILIZED ZIRCONIA

Parts of the contents of this chapter comprise a section of a manuscript in revision titled "Shape Memory and Superelasticity in Polycrystalline Ceria-Stabilized Zirconia Honeycombs" by L.K. Quinn, R. Esteves, P. Latorre-Suárez, G.R. Rossman, S. Ragahavan, and K.T. Faber. In this work, L.K. Quinn designed and executed the experimental work, with assistance from R. Esteves, P. Latorre-Suárez, G.R. Rossman, and S. Raghavan in carrying out experiments utilizing specialized compression setups. K.T. Faber supervised the experimental work and edited the manuscript. All authors assisted in reviewing the manuscript.

2.1. Introduction

Shape memory materials encompass alloyed, polymeric, and ceramic materials that can experience stress- or heat-induced deformation and return to their original shape[1–3]. In alloys and ceramics, this behavior is underpinned by the martensitic transformation: a diffusionless phase transformation between the austenite and martensite phases[4–7]. Widely exploited in shape memory alloys such as nitinol, the martensitic transformation enables accommodation of significant strains through the simultaneous shifting of atoms without diffusion across large length scales[8]. While this behavior is well-studied and commercialized in alloys, it has been more difficult to observe in ceramic systems such as zirconia (ZrO_2) until recently, despite reports on zirconia's ability to undergo such martensitic transformations in the 1980s[2, 6, 7, 9–13]. This is due to the large volume expansion (approximately 4%) that accompanies the martensitic transformation in zirconia, leading to strain mismatches at grain

boundaries that cause cracking and premature failure in polycrystalline ceramic systems[2, 13].

Recently, however, advances in processes such as nano-scale fabrication and freeze casting have enabled exploration of the martensitic transformation in zirconia systems[14–20] (these techniques will be discussed in further detail in Chapter III). As such, the conditions under which this transformation can be induced can now be probed in greater detail. Zirconia's ability to exhibit shape memory behavior is due to its transformation between the monoclinic and tetragonal phases, which in pure zirconia occurs around 1170°C. The relationship between these two phases is characterized by the temperatures at which the forward transformation from tetragonal to monoclinic starts and finishes, M_s and M_f, and the temperatures at which the reverse transformation from monoclinic to tetragonal start and finish, A_s and A_f, described in Table 1[21–24]. However, these transformation temperatures are lowered when dopants such as Y_2O_3, MgO, TiO_2, and CeO_2 are incorporated into the zirconia matrix (Table 1). As a result, compositions of zirconia may be developed such that the martensitic transformation can be induced at or below room temperature[24, 25]. This work will utilize two compositions of ceria-doped zirconia to explore two different behavioral regimes at room temperature, shape memory behavior and superelastic behavior, as discussed in Chapter III.

Table 2.1. Characteristic transformation temperatures of zirconia compositions.

	Tetragonal to monoclinic		***Monoclinic to Tetragonal***		
Composition	*M_f (°C)*	*M_s (°C)*	*A_s (°C)*	*A_f (°C)*	**Ref**
ZrO_2	1032	1053	1202	1223	[21]
2% Y_2O_3 – 5% TiO_2 – 93% ZrO_2	311	397	436	540	[22]
12.5% CeO_2 – 87.5% ZrO_2	-31	43	186	263	[23]

Once the characteristic martensitic transformation temperature has been tuned to the relevant temperature range, the phase transformation between monoclinic and tetragonal zirconia can be tracked using a range of techniques, each with benefits and challenges. Electron backscatter diffraction (EBSD) can be used to identify crystallographic orientations and phases, and thus track how grain sizes and orientations interface with martensitic transformations[24, 26]. However, it requires precise machining of small samples or polishing of larger-scale samples to extremely flat surfaces. Differential scanning calorimetry (DSC) has traditionally been used to identify characteristic transformation temperatures, and thus identify the temperature ranges in which martensitic transformations can be observed[22]. While helpful in identifying the characteristic transformation temperatures, DSC on its own does not enable other crystallographic studies of the relevant phase transformations, and only allows for heat-induced transformations. Mechanical load frames can be used to trigger stress-induced transformations but like DSC, do not, on their own, enable study of the relevant phases without additional external instrumentation[14, 27]. The use of mechanical load frames to study stress-induced martensitic transformations in zirconia systems will be discussed in greater depth in Chapter III.

X-ray diffraction (XRD) is a popular and accessible technique for assessing the phase content of zirconia systems before, during, and after martensitic transformations[28, 29]. Used to gauge the extent of the martensitic transformation in early work on the subject, much of the current research into shape memory effects in ceramic systems utilizes XRD to track the extent of the phase transformation. In crystalline zirconia, the $(\bar{1}11)$ and (111) monoclinic peaks at $2\theta = 28°$ and $31°$, respectively, and the (011) tetragonal peak at $2\theta = 30°$ are clearly discernible from one another, and thus can be used to calculate the relative fraction of monoclinic and tetragonal zirconia present in the collection volume[29].

Powder X-ray diffractometers, unlike the more powerful X-ray sources at beamline facilities, are able to penetrate only a few microns deep in the surface of zirconia,

depending on the specific radiation source, zirconia composition, and 2θ range[30]. The size of the surface area scanned will likewise depend upon these factors, but generally powder X-ray diffraction yields data from a collection volume on the order of 10^{-1} mm^3, depending on the specific dopant composition of the ZrO_2 system[3,30,31]. Doping zirconia with other oxides, necessary for studying phase transformations in zirconia systems at room temperatures, will also cause a slight shift in the 2θ values of the peaks but will not impact the background noise intensity of the collected spectra.

While XRD is a valuable experimental tool for determining the phase content over a volume on the order of 10^{-1} mm^3, the polycrystalline zirconia systems studied in this chapter and in Chapter III are comprised of grains on the order of 10^1 μm. As such, XRD provides a holistic look at the overall behavior of a polycrystalline sample. To track the extent of the phase transformation on a smaller volume scale, this work turns to Raman spectroscopy. As tetragonal zirconia has six characteristic Raman peaks and monoclinic zirconia has at least eighteen, many of which don't overlap, it is possible to distinguish between these two phases in the Raman spectrum of a zirconia sample[32]. Like XRD, Raman spectroscopy can be used to probe a few microns deep in the surface of a zirconia sample[33]. Depending on the porosity of the sample and the laser fluence used, the spot size of the laser on the sample can be tuned such that the collection volume is on the order of 10^{-5} mm^3.

While the XRD and Raman spectra of zirconia are both slightly shifted on the addition of dopants, such dopants impact the appearance and analysis of Raman spectra far more than they do XRD traces. As dopants are added to zirconia systems, as is required for room temperature studies of martensitic transformations, they increase the overall disorder of the crystal lattice, and thus increase the relative intensity of the background in the Raman spectra. As a result, previous literature seeking to use Raman spectra to determine relative phase contents in zirconia systems primarily focused on those systems with at most 10 mol% dopants[9,34–37]. The 12.5

mol% and 16.0 mol% ceria-stabilized zirconia (CSZ) systems studied in this work, then, are well past that boundary. To quantitatively analyze the relative amounts of monoclinic and tetragonal phase present in these systems, it was necessary to develop a process for analysis specific to these high-ceria compositions. In this work, a process to quantitatively analyze the relative monoclinic and tetragonal phase contents in ceria-stabilized zirconia through Raman spectroscopy was produced.

2.2. Materials and Methods

2.2.1. Sol-gel synthesis

Ceria-stabilized zirconia (CSZ) was prepared through a sol-gel synthesis adapted from the Pechini method preparation outlined by Pang et al.[23]. Stoichiometric amounts of cerium (III) nitrate hexahydrate (Thermo Fisher Scientific, Waltham, MA, USA) and zirconyl chloride octahydrate (Sigma-Aldrich, St. Louis, MO, USA) were stirred with deionized water to atomistically mix the metal oxide precursors. Citric acid monohydrate (VWR International, Radnor, PA, USA) and ethylene glycol (Thermo Fisher Scientific, Waltham, MA, USA) were then added in a molar ratio of 24:4:1 ethylene glycol: citric acid: total precursor powders. The solution was stirred at 100°C for 1 h, then heated at 130°C without stirring until the gel was hardened. The gels were then calcined in a CTF 17/300 tube furnace (Carbolite Gero, Sheffield, UK) at 600 °C under flowing air for 2 h.

2.2.2. Sample preparation

2.2.2.1. Freeze-cast samples

To create samples with a range of phase contents, 12.5 mol% CeO_2-ZrO_2 powders were first freeze cast to create ceramic structures with highly aligned, columnar pores. To do so, the powders were suspended in cyclohexane (VWR International, Radnor, PA, USA) at a concentration of 10 vol% after fully dissolving 10 wt.% of the powder mass of Hypermer KD4 dispersant (Croda, Inc., Yorkshire, UK) in the

cyclohexane. The suspensions were ball milled until fully mixed, then freeze cast using an apparatus described previously (Figure 1.6b)[27,38]. Gradient-controlled freeze casting was performed at a constant freezing rate of 1 μm/s. Samples were then freeze dried in a SP Scientific AdVantage 2.0 Benchtop lyophilizer (SP Scientific Warminster, PA, USA) for at least 24 h and sintered in a CM Rapid Temp 1700°C box furnace (CM Furnaces, Inc, Bloomfield, NJ, USA) using the temperature profile described in Section 2.2.2.1. The process of freeze casting and analyzing these samples will be discussed in greater detail in Chapter III.

2.2.2.2. Compression of freeze-cast samples

In order to observe both highly monoclinic and highly tetragonal regions of the sintered, freeze-cast samples, the samples were first machined such that 9.6 mm diameter cylindrical samples were core drilled out of sintered samples, then the top and bottom were sliced off using a IsoMet 5000 Linear Precision Saw (Buehler, Lake Bluff, IL, USA) so that cylindrical specimens with parallel faces were produced. The samples were then compressed to loads up to 50MPa using the Instron universal testing machine and analyzed using XRD and Raman spectroscopy.

2.2.2.3. Pellets

To create samples with a range of ceria concentrations, ceria-zirconia powders of compositions ranging from 0 to 18 mol% CeO_2 were prepared by loading powders of each composition into a die and applying pressure using an Instron universal testing machine (Instron, Norwood, MA, USA). The samples were then sintered in air in a CM Rapid Temp 1700 °C box furnace (CM Furnaces, Inc, Bloomfield, NJ, USA) at 550 °C for 2 h, then 1500 °C for 10 h.

2.2.3. Phase analysis

2.2.3.1. X-ray diffraction

X-ray diffraction traces were collected using a Panalytical X'Pert Pro Powder X-ray Diffractometer using Cu K-α radiation (Malvern Panalytical, Worcestershire, UK). The volume fraction of monoclinic phase present in each sample, V_m, was calculated from XRD traces through the method outlined by Toraya et al., which utilizes a ratio of the integrated area under the monoclinic and tetragonal peaks to calculate the V_m[29].

2.2.3.2. Raman spectroscopy

Approximately 100 Raman spectra were collected at different regions across the flat face of a freeze-cast cylindrical sample after compression to loads ranging from 0-50MPa using a 50X lens in a Renishaw Raman InVia microscope (Renishaw Inc, Wotton-under-Edge, UK) with a 532 nm laser at 10% power. As the size of the collection area is dependent on the laser power and lens used, these factors were kept consistent across all ex-situ analyses so that the collection area was always approximately 100mm in diameter. The fluorescent background of each spectrum was defined as a spline between the value of the spectrum intensity at 50 cm-1, 800 cm-1, 1030 cm-1, and 1400 cm-1, and was subtracted from the spectrum before peak intensities were calculated.

2.3. Results and Discussion

2.3.1. Phase quantification using equations from prior literature

In seeking to quantify the relative volumes of monoclinic and tetragonal phases in ceria-stabilized zirconia samples, four equations from previous literature quantifying the monoclinic volume fractions (V_m) were tested on spectra collected from 12.5 mol% CSZ samples, as seen in Figure 2.1. In these tests, 100 spectra were collected from different regions on a sample, and their monoclinic volume fractions calculated

through equations developed by Clarke & Adar (1984), Kontoyannis et al. (1994), Katagiri et al. (1988), and Lim et al. (1992) (Equations 2.1-4). In all of these equations, the intensity of monoclinic peaks at 181 cm^{-1} and 192 cm^{-1} (I_m^{181} and I_m^{192}) and the intensity of tetragonal peaks at 148 cm^{-1}, 260 cm^{-1}, and 630 cm^{-1} (I_t^{141}, I_t^{260}, and I_t^{630}) were related to the molar (X_m) or volume fraction (V_m) of monoclinic phase present. The average of these 100 monoclinic volume fraction values was then plotted against the V_m calculated from the XRD traces of the same sample using the Toraya et al. method (1984). (Equations 2.5 and 2.6)

Clarke & Adar[9] (1984)

$$V_M = \frac{I_m^{181} + I_m^{192}}{0.97(I_t^{148} + I_t^{260}) + I_m^{181} + I_m^{192}} \quad (2.1)$$

Kontoyannis et al.[34] (1994)

$$\frac{(I^{630} - 0.47I^{260})}{I^{181}} = \frac{1}{x_m} 0.16 + .27 \quad (2.2)$$

Katagiri et al.[36] (1988)

$$V_M = \frac{I_m^{181} + I_m^{192}}{2.2(I_t^{148}) + I_m^{181} + I_m^{192}} \quad (2.3)$$

Lim et al. [37] (1992)

$$V_M = \frac{I_m^{181} + I_m^{192}}{0.33(I_t^{148} + I_t^{260}) + I_m^{181} + I_m^{192}} \quad (2.4)$$

Toraya et al.[29] (1984)

$$X_m = \frac{A_m^{(111)} + A_m^{(\bar{1}11)}}{A_m^{(111)} + A_m^{(\bar{1}11)} + A_t^{(101)}} \quad (2.5)$$

$$V_m = \frac{1.311X_m}{1 + 0.311X_m} \quad (2.6)$$

An accurate calculation of V_m from Raman spectra should trend with that from XRD traces—that is, samples with high monoclinic content as determined via XRD should have more randomly-selected regions with highly monoclinic spectra and thus have higher average V_m as calculated from Raman spectra, and vice versa. While the number of spectra collected and the polycrystalline nature of the samples should have yielded a degree of error given the differing monoclinic contents of the regions

scanned, the overall trend should have matched that of the V_m as calculated through XRD. As seen in Figure 2.1, however, this was not the case. None of the four methodologies tested showed an increase in monoclinic content as XRD-derived V_m increased over the full monoclinic content, rather, the V_m as calculated through each of the four Raman-based methods stayed relatively constant. While some of the methods estimated the V_m as higher than that calculated from XRD, and others calculated the average V_m as lower than that calculated from XRD, the Raman-derived values remained relatively constant using many of the method. This disagreement indicated that the high-ceria composition of the samples under study here were poorly suited to analysis using these equations.

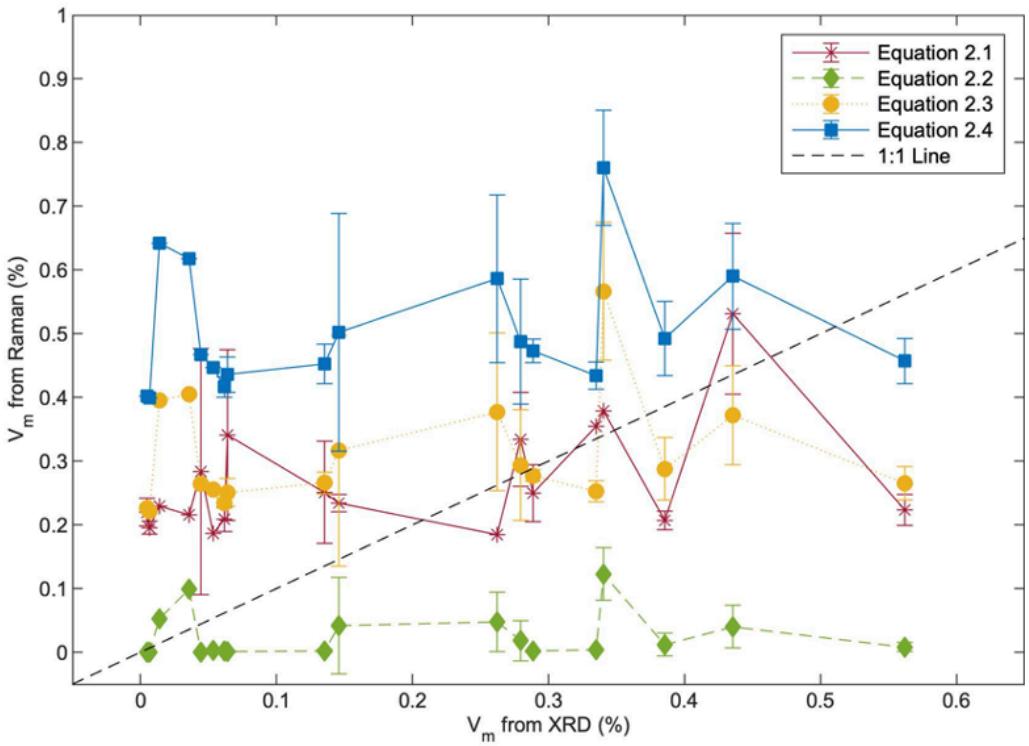

Figure 2.1. Calculated monoclinic phase content from Raman spectra using Equations 2.1-2.4, compared to the monoclinic phase content as calculated through XRD traces using Equations 2.5-6. The line where the two values would be equal is shown in black.

The differences in composition between the samples studied here and those studied in the previous literature (generally doped at concentrations less than 10 mol%) meant that the different compositions would have different levels of background intensity. Background intensity in Raman spectra can be caused by a range of factors, including inadequate focus on the sample, highly fluorescent impurities, and large quantities of dopants. The first two factors, an example of which is shown in Figure 2.2, can be easily corrected for by applying background removal programs common to most spectrometer or spectra-processing software. Accounting for high dopant concentrations, however, can be more difficult.

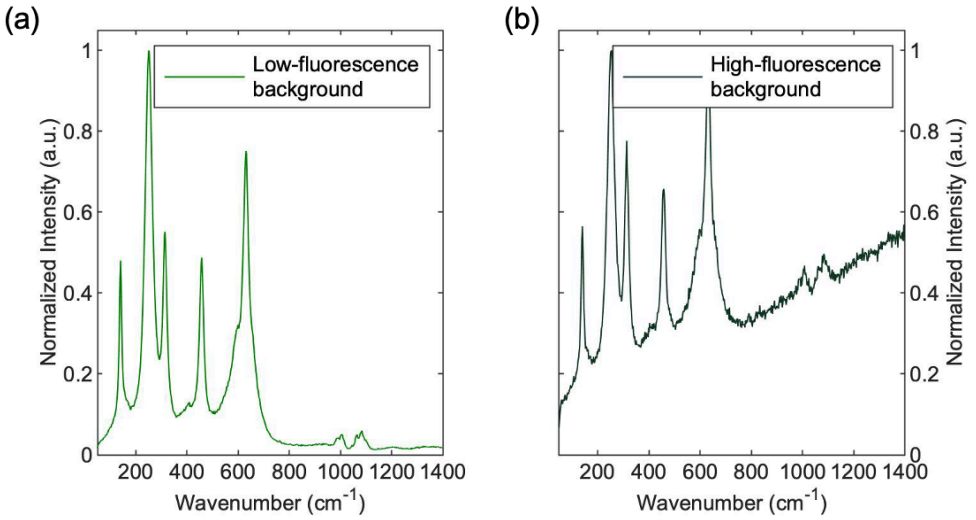

Figure 2.2. Raman spectra of 12.5 mol% ceria-stabilized zirconia samples exhibiting (a) low background intensity and (b) high background intensity.

2.3.2. Effects of cerium doping on spectral characteristics

To explore the effect of dopants on Raman spectral background more closely, samples with compositions ranging from 0-18 mol% CeO_2-stabilized ZrO_2 were prepared through a sol-gel synthesis method discussed in further detail in Chapter III. XRD and Raman traces of each composition, shown in Figure 2.3, revealed both the

stabilization effect of CeO_2 on the tetragonal phase of ZrO_2, and the increase in background intensity as Ce concentration increased.

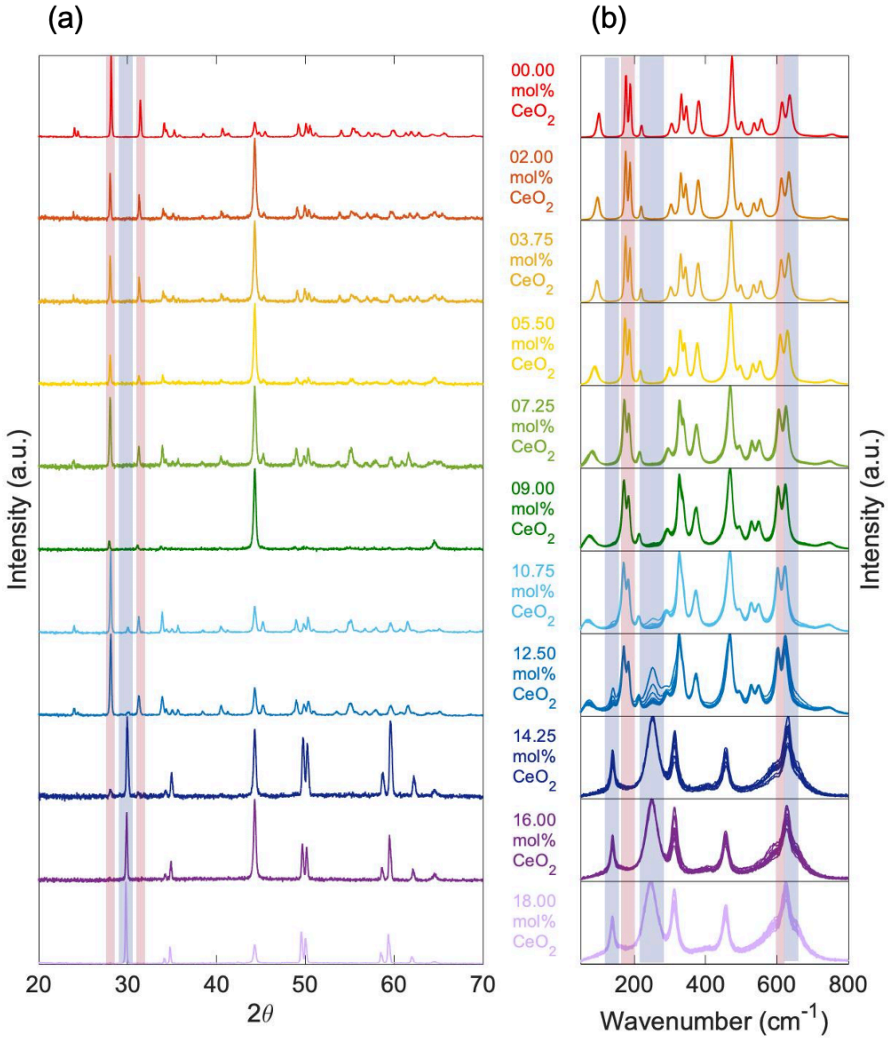

Figure 2.3. Sintered CSZ pellets ranging from 0-18 mol % CeO_2 show increasing tetragonal phase stabilization with Ce content. (a) XRD traces and (b) Raman spectra of sintered CSZ pellets ranging from 0-18 mol% CeO_2. Monoclinic peaks used in Equations 2.1-2.6 are highlighted in red, and tetragonal peaks used in Equations 2.1-6 are highlighted in blue.

Pure ZrO_2, as expected, exhibited fully monoclinic XRD and Raman traces. As the Ce content was increased, the spectra showed that the tetragonal phase was first partially, then fully stabilized at room temperature, and at the highest Ce concentrations, both the XRD and Raman spectra showed fully tetragonal ceria-stabilized zirconia. As the tetragonal phase became prevalent, the intensity of the background in the Raman spectra also increased with increasing Ce concentrations. At low Ce concentrations, the spectra had almost no background intensity—they were nearly perfectly flat in regions where peaks were not present. But as the Ce concentration increased, the relative background intensity in regions without peaks became higher with respect to the highest peak in the spectrum.

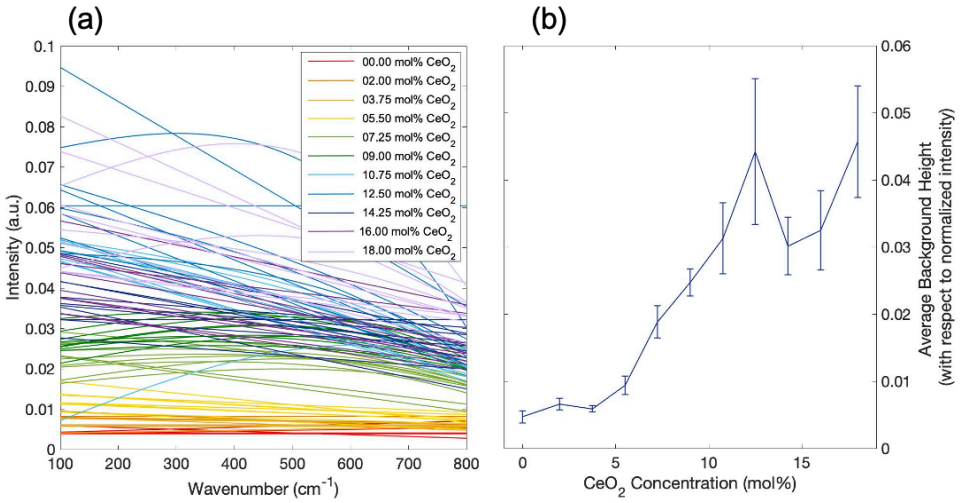

Figure 2.4. Background intensities of the Raman spectra seen in Figure 2.3b. (a) Background intensity with respect to wavenumber of ceria-stabilized zirconia pellets ranging from 0-18 mol% CeO_2. (b) The average value of the background intensities plotted as a function of CeO_2 concentration, with error bars showing one standard deviation.

This effect was also quantitatively analyzed. In Figure 2.4a, the background intensities of each composition were mapped, and the average value of those intensities was plotted in Figure 2.4b with respect to Ce concentration. This

quantitative analysis further highlighted that background intensity increased with Ce concentration up until concentrations around 11 mol% CeO_2, at which point the intensity of the background plateaued. Importantly, the background intensity values for 12.5 mol% and 16.0 mol% CeO_2-stabilized ZrO_2 were within error margins of each other, indicating that spectra of the two compositions that will be studied in greater depth in Chapter III should have similar background contributions.

This increase in background intensity underscored the difficulty of applying the equations developed by previous investigators to the high-ceria compositions in use in this work. Small peaks, especially, may be particularly complicated to resolve or deconvolute from the more intense background regions. The peak intensity ratios that were used in previous work to quantify monoclinic phase content thus did not apply to these compositions. As such, an alternative process for quantifying monoclinic phase content in high-ceria compositions of CSZ had to be developed.

2.3.3. Application of a rule-of-mixtures approach

2.3.3.1. Development of composite spectra model

To quantify the relative volume fractions of monoclinic and tetragonal phases in these compositions of ceria-stabilized zirconia, a rule of mixtures approach was applied. This approach was both simple, and specific to doping with ceria—it accounted for the peak shift and the background level of the specific composition used. Figure 2.5a shows the “pure” monoclinic and tetragonal spectra that were combined using a weighted average to produce the composite spectra shown in Figure 2.5b. To quantitatively analyze the amount of monoclinic character present in each Raman spectrum, peaks that were characteristic to only the monoclinic and tetragonal phases were identified.

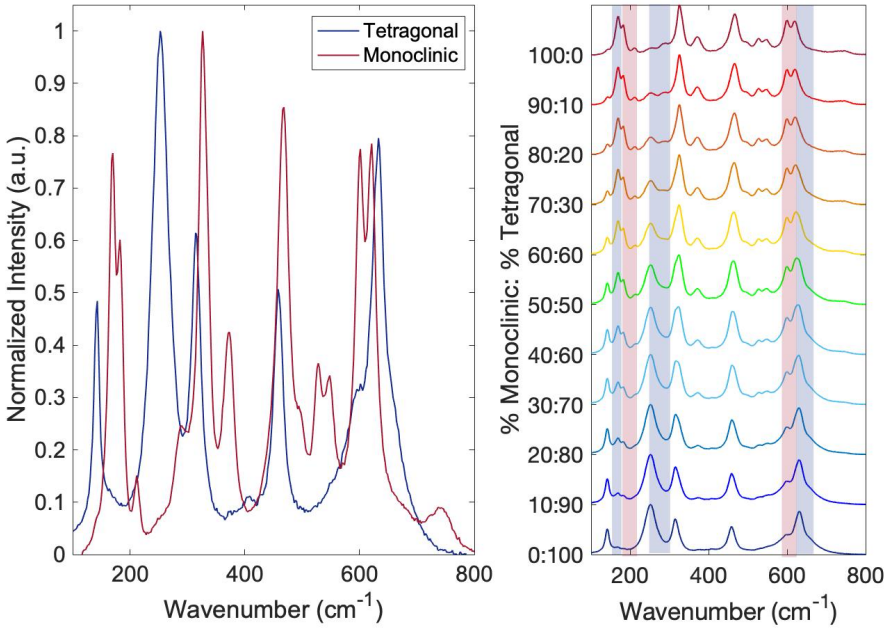

Figure 2.5. A rule-of-mixtures approach was used to generate composite spectra. (a) Raman spectra collected from 12.5 mol% CSZ samples representative of pure tetragonal (blue) and pure monoclinic (red) phases. (b) Composite spectra created through a weighted average of the pure monoclinic and tetragonal Raman spectra in the noted ratios, with monoclinic peaks used for later analysis highlighted in red and tetragonal peaks used for later analysis highlighted in blue.

The tetragonal phase of zirconia has six characteristic Raman modes, whereas the monoclinic phase has upwards of eighteen[32]. In choosing peaks to quantitatively analyze monoclinic fraction, peaks that were as intense as possible were chosen to limit the chance they would be obscured by noise or high background intensity. For this reason, the clear monoclinic doublet around 525 cm^{-1} and 550 cm^{-1} was not considered for quantitative analysis—while characteristic of the monoclinic phase, its relative lack of intensity compared to that of other monoclinic peaks in the spectrum meant that it may be difficult to discern at low monoclinic volume fractions in the background or noise. It was also necessary to select peaks that were separate from modes characteristic to other phases. The monoclinic mode around 220 cm^{-1}

was discarded for quantitative analysis for this reason, as it is very close to the tetragonal mode around 260 cm^{-1}, and these two peaks were subsequently difficult to deconvolute. Six peaks were chosen for further analysis: those at 141 cm^{-1}, 260 cm^{-1}, and 634 cm^{-1}, characteristic of the tetragonal phase, and those at 181 cm^{-1}, 191 cm^{-1}, and 614 cm^{-1}, characteristic of the monoclinic phase.

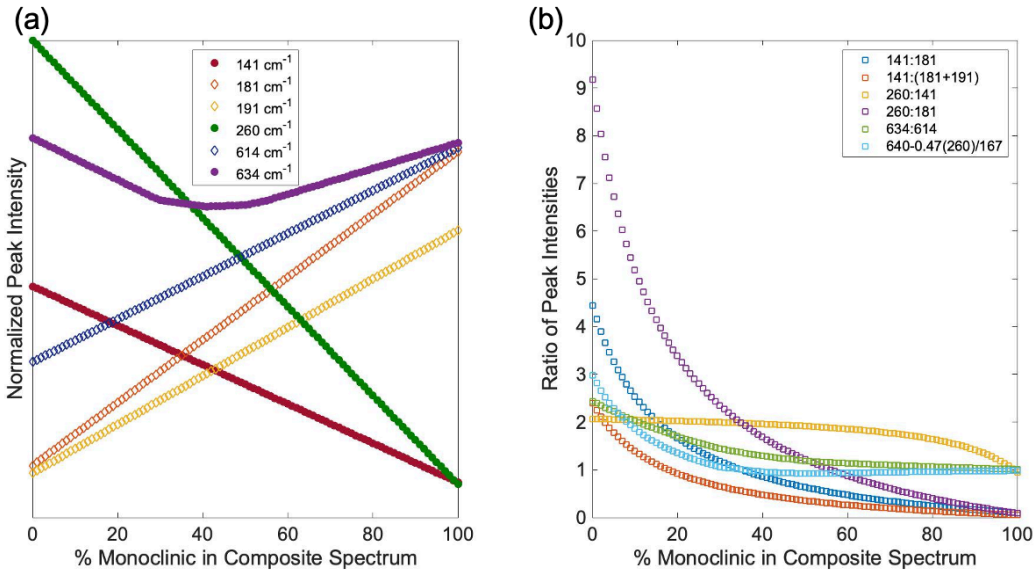

Figure 2.6. Peak intensities and ratios calculated from the composite spectra developed through a rule-of-mixtures approach. (a) Normalized Raman spectrum peak intensities of the tetragonal peaks at 141 cm^{-1} (●), 260 cm^{-1} (●), and 634 cm^{-1} (●), and of the monoclinic peaks at 181 cm^{-1} (◇), 191 cm^{-1} (◇), and 614 cm^{-1} (◇) in composite spectra with V_m from 0-100. (b) Ratios of selected Raman peak intensities with respect to the V_m of the composite spectrum.

To probe the intensities of the selected peaks over the full range of possible compositions, composite spectra were produced with monoclinic volume fractions ranging from 0 to 100, and the normalized intensity of each of the selected peaks in these composite spectra were plotted against the monoclinic volume fraction (Figure 2.6a). As expected, the intensity of the monoclinic peaks (181 cm^{-1}, 191 cm^{-1}, and 614 cm^{-1}) increased as the weighting of the monoclinic spectrum in the composite

spectrum increased. The opposite is true for the tetragonal peaks at 141 cm^{-1} and 260 cm^{-1}—as V_m increased, their peak intensity decreases. The only peak not to exhibit a linear dependence on V_m was the peak at 634 cm^{-1}, as it overlaps somewhat with the monoclinic peak at 614 cm^{-1}, which made its relationship with V_m more difficult to deconvolute. However, as this peak is easy to see on most spectrometer gratings—peaks at lower wavenumbers can be difficult to distinguish on certain spectrometers—it was not yet fully discarded for analysis, especially for systems at lower V_m.

All of the peak intensity values shown in Figure 2.6a were normalized to the highest peak in the spectrum. As the most intense peak in the spectrum can vary depending on laser fluence, focus on the sample, or fluorescent impurities in actual experimental conditions, a ratio of peak intensities were used to calculate V_m. Several different peak intensity ratios were created from the composite spectra and plotted with respect to the V_m, as shown in Figure 2.6b. As the ratio between the tetragonal peak at 260 cm^{-1} and the monoclinic peak at 181 cm^{-1} spanned the largest range of values, it was deemed best for analysis. In Figure 2.7, this ratio was fit with an exponential fit (Equation 2.7), and this relationship was used to calculate the V_m from the ratio of peak intensities of ten randomly selected spectra, also plotted. The fit of this exponential equation agreed well with the ratios of peaks from the composite spectra at low and high values of V_m. At intermediate values of V_m, the fit was less good, and tended to overestimate the percentage of monoclinic phase by about 3%. However, choosing an exponential fit rather than a complicated piecewise equation enabled simple calculations of the monoclinic phase content of a given spectrum.

$$\frac{I_t^{260}}{I_m^{181}} = 8.4749e^{-0.039V_m} \tag{2.7}$$

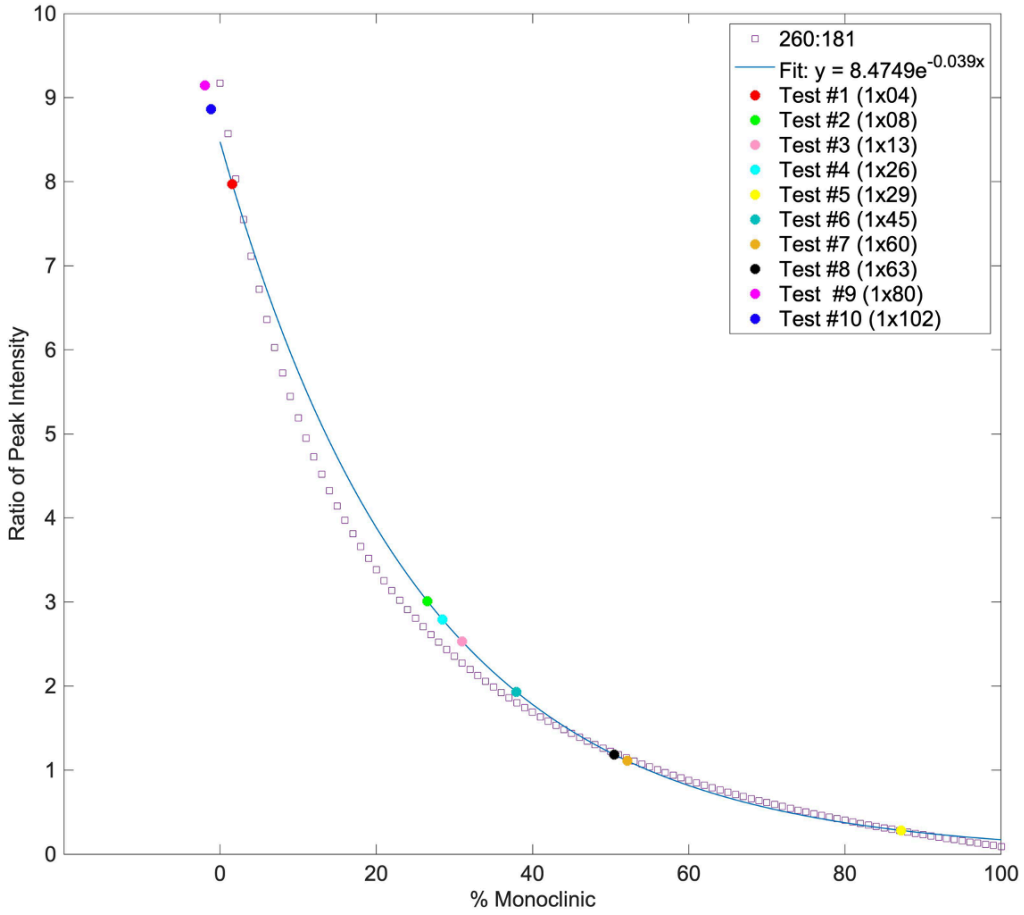

Figure 2.7. The ratio of Raman peak intensities $\frac{I_t^{260}}{I_m^{181}}$ *plotted against* V_m *of the composite Raman spectra (o), fit with Equation 2.7. The* V_m *of the test cases calculated using Equation 2.7 are shown as squares.*

2.3.3.2. Comparison with experimental data

To validate how well this composite spectra-derived equation matched experimental data, Equation 2.7 was applied to experimentally obtained spectra to calculate the V_m of those regions. Those experimentally obtained spectra were then compared to composite spectra with the same V_m. These spectra are shown in Figure 2.8, and further confirmed that this rule of mixtures approach allowed for quantitative analysis of experimental data. Figures 2.8a and 2.8b show a low- and high-monoclinic content

spectra, respectively, and the experimentally obtained and model composite spectra were in good agreement.

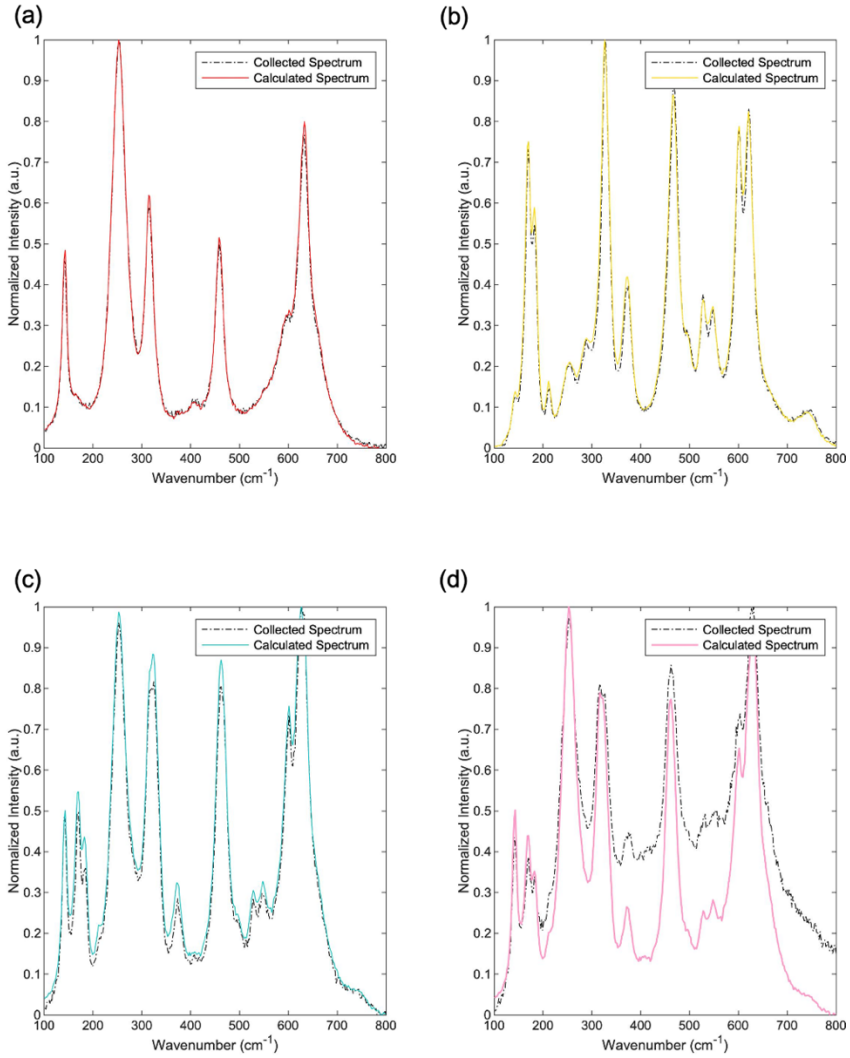

Figure 2.8. Selected Raman spectra of experimentally obtained test cases (dashed lines), with the composite spectrum corresponding to the calculated V_m overlaid (solid lines). Spectra with low (a) and high (b) V_m show good agreement with the composite spectra. (c) A spectrum with intermediate V_m exhibits slightly less intense peaks than the calculated composite spectrum. (d) An experimental spectrum exhibits peak intensities that match the calculated spectra well despite their high background intensity.

In Figure 2.8c, a spectrum with an intermediate value of V_m is shown, and while the calculated spectrum exhibited more intense monoclinic peaks than did the experimental spectrum, as was predicted by the fit line, they otherwise matched relatively well. Finally, Figure 2.8d shows a collected spectrum with an unusual background intensity, likely due to insufficient focus on the face of the sample. However, despite the large difference in background intensities between the collected and composite spectra, the peak intensities of the relevant peaks at 181 cm^{-1} and 260 cm^{-1} were still within 10% of each other. Comparisons of the other test spectra from Figure 2.7 and the corresponding composite spectra are shown in Figure A.2. Taken together, these test spectra qualitatively validate the fit of the model developed and shown in Figure 2.7: a model obtained using composite spectra matched the characteristics of experimentally obtained spectra well and allowed for the estimation of monoclinic phase contents in zirconia samples with high Ce concentrations.

2.3.3.3. Alternative peaks and ratios

One potential downside to this model, however, was that it relied upon calculating the intensity of peaks at relatively lower wavenumbers. As stated in Section 2.3.3.1, certain spectrometers and/or gratings may not be able to resolve peaks at lower wavenumbers as easily as those at higher wavenumbers. In Figure 2.9a, an alternative ratio of peak intensities was considered, using the monoclinic peak at 614 cm^{-1} instead of the peak at 181 cm^{-1}. At V_m less than 50% monoclinic phase, the fit of the quadratic equation (Equation 2.8) that best matches this peak intensity ratio was relatively good. However, at highly monoclinic compositions, the fit was noticeably poorer, and estimated the monoclinic phase fraction up to 15% lower than the composite spectra data would imply.

$$\frac{I_t^{260}}{I_m^{614}} = 0.0002\,{V_m}^2 - 0.0513\,V_m + 2.9381 \tag{2.8}$$

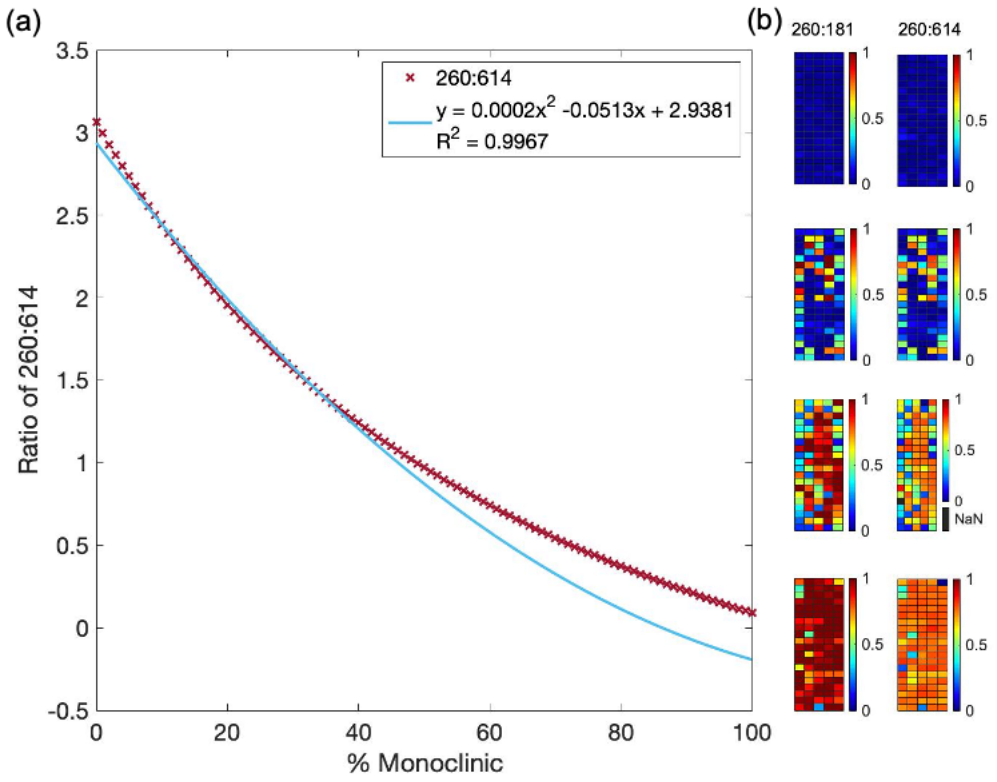

Figure 2.9. Alternate peak intensities were considered for quantitative analysis. (a) The ratio of Raman peak intensities $\frac{I_t^{260}}{I_m^{614}}$ *plotted against* V_m *of the composite spectra (x), fit with Equation 2.8 (—). (b) 20 by 5 colormaps based upon Raman spectra of the* V_m *for four different samples calculated using Equations 2.7 and 2.8, with* $V_m = 0$ *shown as dark blue, and* $V_m = 1$ *shown as dark red.*

This was seen in further detail in Figure 2.9b, in which two sets of 20x5 colormaps are shown. In these colormaps, each square corresponded to a spectrum collected from a 12.5mol% CSZ sample, and a color was assigned to a square depending on the value of V_m as calculated from Equation 2.7 and from Equation 2.8—blue corresponded to entirely tetragonal, and red corresponded to entirely monoclinic phases. When mostly tetragonal, with most V_m less than 50%, the colormaps matched well. However, in colormaps corresponding to more heavily monoclinic regions of the sample, the maps derived from Equation 2.8 showed lower monoclinic content than those derived from Equation 2.7, which corresponded with the fit line of

Equation 2.8 underestimating the value of V_m in highly monoclinic compositions by as much as 15%. More complex equations could be used to bring this peak ratio into better agreement with the collected data, but given the better fit provided by Equation 2.7, this ratio was ultimately discarded for analysis. For future work discussed in Chapter III, the spectrometers used for data collection were tested to ensure the monoclinic peak at 181 cm^{-1} was visible so that Equation 2.7 could be accurately used to calculate V_m.

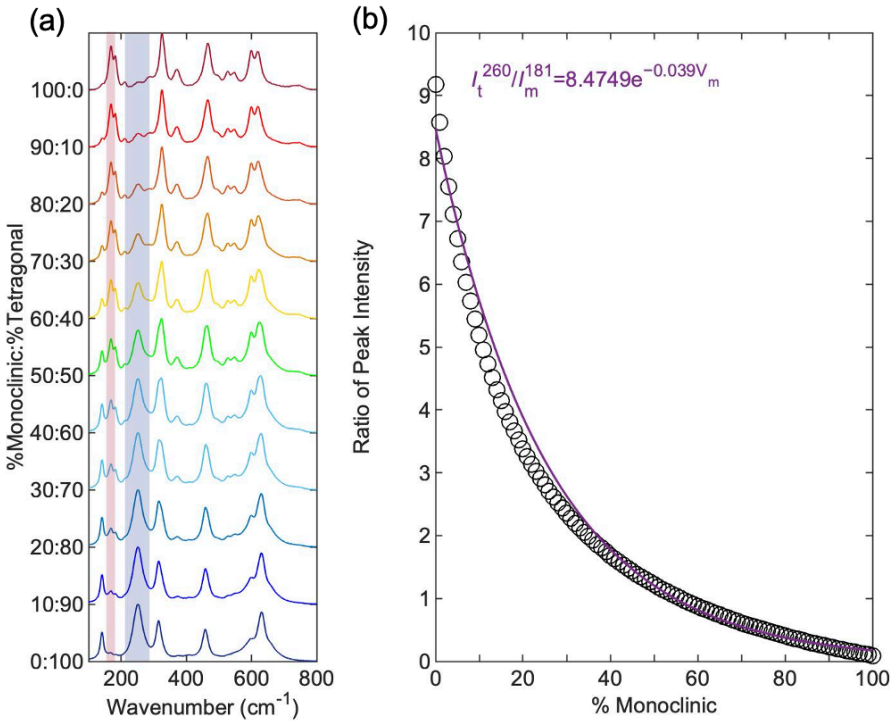

Figure 2.10. Quantification of monoclinic volume fraction in CSZ through a rule-of-mixtures approach. (a) Composite Raman spectra of 12.5mol% CSZ obtained through the rule of mixtures approach, with the peaks selected for quantitative analysis highlighted in red (monoclinic) and blue (tetragonal), and (b) the ratio of peak intensities plotted against the monoclinic content of the composite spectrum with its corresponding fit (in purple).

The ratio developed in previous sections and related to V_m in Equation 2.7 will thus be used going forward. In Figure 2.10, the peaks selected for analysis of phase

content are shown alongside the ratio of peak intensities with respect to monoclinic phase content. In Chapter III, this method will be utilized to calculate the monoclinic phase content present in a range of samples exposed to various compression and heating conditions.

2.4. Summary

Previous studies utilizing Raman spectra to calculate the relative volume fractions of monoclinic and tetragonal phases in zirconia samples had generally focused on zirconia compositions with less than 10 mol% dopants. As a result, an alternative method to quantitatively establish the monoclinic volume fraction, V_m, in high-ceria compositions of stabilized zirconia was necessary. These high dopant concentrations are needed to observe martensitic transformations in ceria-stabilized zirconia systems at room temperatures but lead to high spectral background as the dopant ions increased the lattice disorder of the system. As a result of poor matches between monoclinic volume fractions calculated from equations in previous literature and expected monoclinic volume fractions as calculated from XRD, a rule-of-mixtures approach was adopted to create a simple analytical procedure that matched well with experimentally obtained data.

This rule-of-mixtures approach utilizes composite spectra derived from a weighted average of pure monoclinic and pure tetragonal Raman spectra. A ratio of the peak intensities of these composite spectra was found to be fit by an exponential equation with less than 5% disagreement between the ratio of peak intensities and the exponential fit. This equation was then used to calculate the V_m from experimentally obtained spectra. While ratios of the intensities of other peaks were considered, ultimately the ratio between the tetragonal peak at 260 cm^{-1} and the monoclinic peak at 181 cm^{-1} was used for calculations going forward, as it provided the best match with experimental data over a wide range of monoclinic volume fractions.

This analytical procedure for calculating the monoclinic volume fraction of a polycrystalline zirconia sample is then able to be used to track martensitic

transformations through Raman spectroscopy. In Chapter III, this procedure will be used to observe the martensitic transformation on much smaller volume scales than powder X-ray diffraction techniques will allow and lend insight into spatial heterogeneity of the martensitic transformation in complex, polycrystalline systems.

2.5. References

1. Tadaki, T., Otsuka, K., Shimizu, K. Shape-Memory Alloys. *Annu Rev Mater Sci*. 1988;18:25–45. https://doi.org/10.1146/annurev.ms.18.080188.000325.
2. Swain, M.V. Shape Memory Behaviour in Partially Stabilized Zirconia Ceramics. *Nature*. 1986;322(6076):234–236. https://doi.org/10.1038/322234a0.
3. Ratna, D., Karger-Kocsis, J. Recent Advances in Shape Memory Polymers and Composites: A Review. *J Mater Sci*. 2008;43(1):254–269. https://doi.org/10.1007/s10853-007-2176-7.
4. Kim, H.Y., Ikehara, Y., Kim, J.I., Hosoda, H., Miyazaki, S. Martensitic Transformation, Shape Memory Effect and Superelasticity of Ti–Nb Binary Alloys. *Acta Mater*. 2006;54(9):2419–2429. https://doi.org/10.1016/j.actamat.2006.01.019.
5. Patel, J.R., Cohen, M. Criterion for the Action of Applied Stress in the Martensitic Transformation. *Acta Metall*. 1953;1(5):531–538. https://doi.org/10.1016/0001-6160(53)90083-2.
6. Bansal, G.K., Heuer, A.H. On a Martensitic Phase Transformation in Zirconia (ZrO_2)—I. Metallographic evidence. *Acta Metall*. 1972;20(11):1281–1289. https://doi.org/10.1016/0001-6160(72)90059-4.
7. Bansal, G.K., Heuer, A.H. On a Martensitic Phase Transformation in Zirconia (ZrO_2)—II. Crystallographic Aspects. *Acta Metall*. 1974;22(4):409–417. https://doi.org/10.1016/0001-6160(74)90093-5.
8. Duhamel, C., Venkataraman, S., Scudino, S., Eckert, J. Diffusionless Transformations. *Basics of Thermodynamics and Phase Transitions in Complex Intermetallics*. Vol. Volume 1. World Scientific; 2008:119–145. https://doi.org/10.1142/9789812790590_0006.
9. Clarke, D.R., Adar, F. Measurement of the Crystallographically Transformed Zone Produced by Fracture in Ceramics Containing Tetragonal Zirconia. *J Am Ceram Soc*. 1982;65(6):284–288. https://doi.org/10.1111/j.1151-2916.1982.tb10445.x.
10. Hayakawa, M., Kuntani, N., Oka, M. Structural Study on the Tetragonal to Monoclinic Transformation in Arc-Melted Zirconia-2 mol.% Yttria. I. Experimental Observations. *Acta Metall*. 1989;37:2223–8. https://doi.org/10.1016/0001-6160(89)90148-X.
11. Hayakawa, M., Oka, M. Structural Study on the Tetragonal to Monoclinic Transformation in Arc-Melted Zirconia-2 mol.% Yttria. II. Quantitative Analysis. *Acta Metall*. 1989;37:2229–35. https://doi.org/10.1016/0001-6160(89)90149-1.
12. Reyes-Morel, P.E., Chen, I-W. Transformation Plasticity of Ceria-Stabilized Tetragonal Zirconia Polycrystals: I. Stress Assistance and Autocatalysis. *J Am Ceram Soc*. 1988;71:343–53. https://doi.org/10.1111/j.1151-2916.1988.tb05052.x.
13. Reyes-Morel P.E., Cherng, J.S., Chen, I-W. Transformation Plasticity of Ceria-Stabilized Tetragonal Zirconia Polycrystals: II. Pseudoelasticity and Shape Memory

Effect. *J Am Ceram Soc*. 1988;71:648–57. https://doi.org/10.1111/j.1151-2916.1988.tb06383.x.
14. Lai, A., Du, Z., Gan, C.L., Schuh, C.A. Shape Memory and Superelastic Ceramics at Small Scales. *Science*. 2013;341(6153):1505–1508. https://doi.org/10.1126/science.1239745.
15. Faber, K.T. Small Volumes Create Super(elastic) Effects. *Science*. 2013;341(6153):1464–1465. https://doi.org/10.1126/science.1245097.
16. Du, Z., Zeng, X.M., Liu, Q., Lai, A., Amini, S., Miserez, A., Schuh, C.A., Gan, C.L. Size Effects and Shape Memory Properties in ZrO_2 Ceramic Micro- and Nano-Pillars. *Scr Mater*. 2015;101:40–43. https://doi.org/10.1016/j.scriptamat.2015.01.013.
17. Du, Z., Zeng, X.M., Liu, Q., Schuh, C.A., Gan, C.L. Superelasticity in Micro-Scale Shape Memory Ceramic Particles. *Acta Mater*. 2017;123:255–263. https://doi.org/10.1016/j.actamat.2016.10.047.
18. Yu, H.Z., Hassani-Gangaraj, M., Du, Z., Gan, C.L., Schuh, C.A. Granular Shape Memory Ceramic Packings. *Acta Mater*. 2017;132:455–466. https://doi.org/10.1016/j.actamat.2017.04.057.
19. Rauch, H.A., Chen, Y., An, K., Yu, H.Z. *In-Situ* Investigation of Stress-Induced Martensitic Transformation in Granular Shape Memory Ceramic Packings. *Acta Mater*. 2019;168:362–375. https://doi.org/10.1016/j.actamat.2019.02.028.
20. Crystal, I.R., Lai, A., Schuh, C.A. Cyclic Martensitic Transformations and Damage Evolution in Shape Memory Zirconia: Single Crystals vs Polycrystals. *J Am Ceram Soc*. 2020;103(8):4678–4690. https://doi.org/10.1111/jace.17117.
21. Yashima, M., Mitsuhashi, T., Takashina, H., Kakihana, M., Ikegami, T., Yoshimura, M. Tetragonal—Monoclinic Phase Transition Enthalpy and Temperature of ZrO_2-CeO_2 Solid Solutions. *J Am Ceram Soc*. 1995;78(8):2225–2228. https://doi.org/10.1111/j.1151-2916.1995.tb08642.x.
22. Zeng, X.M., Du, Z., Tamura, N., Liu, Q., Schuh, C.A., Gan, C.L. *In-situ* Studies on Martensitic Transformation and High-Temperature Shape Memory in Small Volume Zirconia. *Acta Mater*. 2017;134:257–266. https://doi.org/10.1016/j.actamat.2017.06.006.
23. Pang, E.L., McCandler, C.A., Schuh, C.A. Reduced Cracking in Polycrystalline ZrO_2-CeO_2 Shape-Memory Ceramics by Meeting the Cofactor Conditions. *Acta Mater*. 2019;177:230–239. https://doi.org/10.1016/j.actamat.2019.07.028.
24. Zeng, X. Development and Characterization of Shape Memory Ceramics at Micro/Nanoscale. Ph.D. Thesis; 2017 https://doi.org/10.32657/10356/69895.
25. Pang, E.L., Olson, G.B., Schuh, C.A. Role of Grain Constraint on the Martensitic Transformation in Ceria-Doped Zirconia. *J Am Ceram Soc*. 2021;104(2):1156–1168. https://doi.org/10.1111/jace.17526
26. Zeng, X.M., Lai, A., Gan, C.L., Schuh, C.A. Crystal Orientation Dependence of the Stress-Induced Martensitic Transformation in Zirconia-Based Shape Memory Ceramics. *Acta Mater*. 2016;116:124–135. https://doi.org/10.1016/j.actamat.2016.06.030.
27. Zeng, X., Arai, N., Faber, K.T. Robust Cellular Shape-Memory Ceramics via Gradient-Controlled Freeze Casting. *Adv Eng Mater.* 2019;21(12):1900398. https://doi.org/10.1002/adem.201900398.

28. Garvie, R.C., Nicholson, P.S. Phase Analysis in Zirconia Systems. *J Am Ceram Soc*. 1972;55(6):303–305. https://doi.org/10.1111/j.1151-2916.1972.tb11290.x.
29. Toraya, H., Yoshimura, M., Somiya, S. Calibration Curve for Quantitative Analysis of the Monoclinic-Tetragonal ZrO2 System by X-Ray Diffraction. *J Am Ceram Soc*. 1984;67(6):C-119-C–121. https://doi.org/10.1111/j.1151-2916.1984.tb19715.x.
30. Henke, B.L., Gullikson, E.M., Davis, J.C. X-Ray Interactions: Photoabsorption, Scattering, Transmission, and Reflection at E = 50-30,000 eV, Z = 1-92. *Atomic Data and Nuclear Data Tables*. 1993;54(2):181–342. https://doi.org/10.1006/adnd.1993.1013.
31. Suzuki, K., Tanaka, K. Applications on High-Energy X-Rays to Stress Measurements of Thermal Barrier Coatings. *Texture, Stress, and Microstructure*. 2003;35(3/4):207–217. https://doi.org/10.1080/0733300310001634943.
32. Zhao, X., Vanderbilt, D. Phonons and Lattice Dielectric Properties of Zirconia. *Phys Rev B*. 2002;65(7):075105. https://doi.org/10.1103/PhysRevB.65.075105.
33. Presser, V., Keuper, M., Berthold, C., Nickel, K.G. Experimental Determination of the Raman Sampling Depth in Zirconia Ceramics. *Appl Spectrosc*. 2009;63(11):1288–1292. https://doi.org/10.1366/000370209789806975.
34. Kontoyannis, C.G., Orkoula, M. Quantitative Determination of the Cubic, Tetragonal and Monoclinic Phases in Partially Stabilized Zirconias by Raman Spectroscopy. *J Mater Sci*. 1994;29(20):5316–5320. https://doi.org/10.1007/BF01171541.
35. Kontoyannis, C.G., Carountzos, G. Quantitative Determination of the Cubic-to-Monoclinic Phase Transformation in Fully Stabilized Zirconias by Raman Spectroscopy. *J Am Ceram Soc*. 1994;77(8):2191–2194. https://doi.org/10.1111/j.1151-2916.1994.tb07117.x.
36. Katagiri, G., Ishida, H., Ishitani, A., Masaki, T. Science and Technology of Zirconia. *American Ceramic Society: Westerville, OH, USA*. 1988;537–544.
37. Lim, C.S., Finlayson, T.R., Ninio, F., Griffiths, J.R. In-Situ Measurement of the Stress-Induced Phase Transformations in Magnesia-Partially-Stabilized Zirconia Using Raman Spectroscopy. *J Am Ceram Soc*. 1992;75(6):1570–1573. https://doi.org/10.1111/j.1151-2916.1992.tb04227.x.
38. Arai, N., Faber, K.T. Gradient-Controlled Freeze Casting of Preceramic Polymers. *J Eur Ceram Soc*. 2023;43(5):1904–1911. https://doi.org/10.1016/j.jeurceramsoc.2022.12.016.

Chapter 3

SHAPE MEMORY AND SUPERELASTIC EFFECTS IN POROUS CERIA-STABILIZED ZIRCONIA

Parts of the contents of this chapter comprise a section of a manuscript in revision titled "Shape Memory and Superelasticity in Polycrystalline Ceria-Stabilized Zirconia Honeycombs" by L.K. Quinn, R. Esteves, P. Latorre-Suárez, G.R. Rossman, S. Ragahavan, and K.T. Faber. In this work, L.K. Quinn designed and executed the experimental work, with assistance from R. Esteves, P. Latorre-Suárez, G.R. Rossman, and S. Raghavan in carrying out experiments utilizing specialized compression setups. K.T. Faber supervised the experimental work and edited the manuscript. All authors assisted in reviewing the manuscript.

3.1. Introduction

Shape memory materials undergo reversible, diffusionless martensitic transformations that enable them to accommodate large stresses[1,2]. Two distinct classes of behavior can result from this martensitic transformation: shape memory effects, in which a material is deformed through the application of either stress or heat but is able to return to its original state upon heating or cooling; and superelastic effects, in which a material reversibly transforms between two states. This unique behavior makes shape memory materials promising candidates for applications such as actuation and energy damping. While shape memory alloys have been widely studied and commercialized, ceramics such as zirconia (ZrO_2) can also exhibit this behavior due to a martensitic transformation between the monoclinic and tetragonal phases[1,3–5]. By adjusting the concentration of dopants in the zirconia system, such as CeO_2 or Y_2O_3, the characteristic transformation temperature can be tuned such that

zirconia-based ceramics can demonstrate either a shape memory or a superelastic effect at room temperature[2, 6–9].

While zirconia's martensitic transformation between tetragonal and monoclinic phases enables it to exhibit shape memory and superelastic behavior, this transformation is also accompanied by a 4% increase in volume[1]. In polycrystalline zirconia, this volume expansion can cause mismatched strains between grains, leading to cracking and premature failure at grain boundaries. These complications initially limited the study of these phenomena in zirconia when they were first observed[2]. To circumvent these challenges, the ratio of the ceramic's surface area to its volume can be increased, thus accommodating the volume expansion[10–17]. This has been achieved by fabricating oligocrystalline micropillars[10, 12, 13, 18], granular packings[19, 20], and even millimeter-size single crystals[21].

To create shape memory materials from bulk-scale, polycrystalline zirconia, an alternative strategy has utilized freeze casting, a facile, tunable, and easily scaled technique to create a network of directionally aligned, honeycomb-like pores[22–27]. These pores have walls from one to three grains wide, accommodating the volume expansion of the martensitic transformation. The shape memory effect was confirmed through increases in monoclinic content using X-ray diffraction (XRD) following compression, decreases in the monoclinic content following heating, and through a change in stiffness of a shape memory sample under compression[24]. But while these techniques offer a holistic look at the extent of the shape memory transformation, they do not fully capture the complexity and diversity of grain behavior in a polycrystalline system.

To observe how individual grains or small grain assemblies behave in shape memory and superelastic zirconia systems, Raman spectroscopy was used as a non-destructive analytical tool, as was discussed in greater detail in Chapter II. Monoclinic and tetragonal zirconia have distinct Raman spectra [28], as they do in XRD patterns, enabling the monitoring of the extent of the transformation using both

techniques. While the collection volume of powder X-ray diffractometry is on the order of 1.5×10-1 mm^3, that of Raman spectroscopy is on the order of 2.25×10^{-5} mm^3 (the exact collection volumes vary depending on porosity and laser fluence). In general, the depth of penetration of X-rays and that of Raman spectroscopy are in the micrometer range. However, background noise in Raman spectra can be exacerbated by factors including high-fluorescence impurities, inaccurate focus on the sample, and the presence of dopants[29–33]. This last factor is particularly relevant to the study of shape memory and superelastic ceria-stabilized zirconia (CSZ) at room temperature, as 12.5 mol% and 16.0 mol% CeO_2 are required to stabilize the zirconia enough to observe shape memory and superelastic behaviors at room temperature, respectively[14].

To introduce another lever of tunability over the sample preparation process, this work additionally utilizes a sol-gel preparation of the CeO_2-ZrO_2 powders to be used in the freeze casting process. Previous work to create porous zirconia structures utilized a mix of ZrO_2 and CeO_2 nanopowders to create the freeze casting suspension[24]. However, this technique can lead to inhomogeneous distribution of Ce within the ZrO_2 matrix. As the dopant concentration directly controls the behavioral regime that a ZrO_2 sample will inhabit, it is crucial to create samples with homogeneous dopant distributions. Subsequently, sol-gel processing—in which metal oxide precursors are atomistically mixed in an aqueous solution with complexing agents before becoming trapped in the gel through a polymerization reaction—was used to create atomistically mixed CeO_2-ZrO_2 powders[34]. Introducing this sol-gel processing step enabled further control over the powder characteristics by altering such factors as the pH of the aqueous solution to change the growth mechanisms at play during the sol-gel synthesis (Figure 1.3).

In this work, sol-gel processing and freeze casting were used to create bulk-scale porous 12.5 mol% and 16.0 mol% ceria-stabilized zirconia with columnar pores and oligocrystalline pore walls. With such microstructural tailoring, the study of shape memory effects in polycrystalline zirconia with 12.5 mol% ceria was extended over

multiple cycles, and Raman spectroscopy techniques developed in Chapter II were used to track the extent of the martensitic transformation. Moreover, relying on the models developed in Chapter II for analysis of Raman spectra, three complementary experimental setups were used to track superelastic behavior: *ex-situ* analysis, *in-situ* compression using an extended Raman probe coupled to a load frame, and *in-situ* compression using a diamond anvil cell.

3.2. Materials and Methods

3.2.1. Sol-gel synthesis

Shape memory and superelastic ceria-stabilized zirconia honeycombs were prepared using the sol-gel synthesis procedures outlined in Section 2.2.1. To investigate the effect of the pH of the aqueous medium on CeO_2-ZrO_2 powder morphologies, the pH of the deionized water was adjusted with HCl (JT Baker, Phillipsburg, NJ, USA) or NH_3OH (Sigma-Aldrich, St. Louis, MO, USA) to the noted pH before adding in the metal oxide precursors and complexing agents to produce 12.5mol% CeO_2-ZrO_2 powder. Samples that were used for analysis of microstructure, shape memory, and superelastic effects were added to unadjusted deionized water. The powders produced at a range of pH values were calcined as discussed in Section 2.2.1, and the morphology of the powders was imaged using scanning electron microscopy on a Zeiss 1550 VP (Carl Zeiss AG, Oberkochen, Germany). Pellets were then produced and sintered in the same manner as in Section 2.2.2.3 for X-ray diffraction and Raman spectroscopic analysis using a Panalytical X'Pert Pro Powder X-ray Diffractometer using Cu K-α radiation (Malvern Panalytical, Worcestershire, UK) and a Renishaw Raman InVia microscope (Renishaw Inc, Wotton-under-Edge, UK). Another set of powders prepared at pH 4 and 7 were freeze cast as discussed below and subjected to increasing compressive stress (Section 3.2.3.1).

3.2.2. Freeze casting

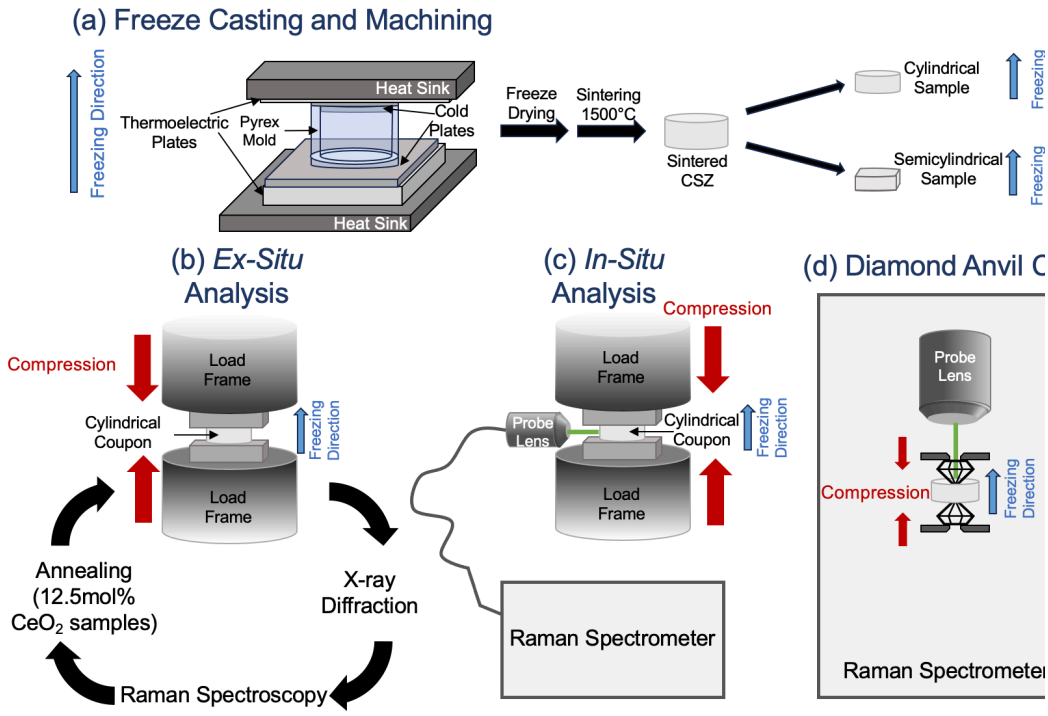

Figure 3.1. Schematics of (a) ceria-stabilized zirconia (CSZ) sample orientation during freeze casting, sintering, and machining, (b) ex-situ compression setup and workflow, (c) in-situ compression setup with Raman spectrometer probe, and (d) diamond anvil cell configuration (not to scale).

As was discussed in Section 2.2.2.2, to create porous CSZ honeycombs, 12 vol% ceria-stabilized zirconia powders of the desired composition were suspended in a mixture of cyclohexane (VWR International, Radnor, PA, USA) and 10 wt.% Hypermer KD4 dispersant (Croda, Inc., Yorkshire, UK) (here, wt.% refers to the mass of ceria-stabilized zirconia powders). The suspensions were ball milled until fully mixed, then freeze cast using an apparatus described previously and shown in Figure 3.1a[24, 35]. Gradient-controlled freeze casting was performed at a constant freezing rate of 1 µm/s through temperature control from 40°C to -30°C on the bottom freezing plate, and from 40°C to 5°C on the top freezing plate. These conditions maintain a temperature gradient of about 5°C/mm. Samples were then

freeze dried in a SP Scientific AdVantage 2.0 Benchtop lyophilizer (SP Scientific Warminster, PA, USA) for at least 24 h and sintered in a CM Rapid Temp 1700°C box furnace (CM Furnaces, Inc, Bloomfield, NJ, USA) at 550°C for 2 h, then 1500°C for 10 h. Scanning electron microscopy (SEM) images were then obtained on a Zeiss 1550 VP (Carl Zeiss AG, Oberkochen, Germany).

Once sintered, cylindrical samples 9.6 mm in diameter were core drilled out of sintered samples, then the top and bottom were sliced off using a IsoMet 5000 Linear Precision Saw (Buehler, Lake Bluff, IL, USA) to produce specimens with parallel faces, as shown in Figure 3.1a. For semicylindrical samples, the cylinder was further sliced along planes parallel to the freezing direction to produce a sample with four flat faces, as shown in Figure 3.1a.

3.2.3. Mechanical testing

3.2.3.1 Ex-situ compression

The mechanical response of the shape memory and superelastic samples was evaluated in uniaxial compression parallel to the freezing direction using an Instron universal testing machining (Instron, Norwood, MA, USA). The experimental setup for *ex-situ* analysis is shown in Figure 3.1b. The samples were placed between beveled washers attached to the compression platens to aid in alignment during the early stages of compression. They were then compressed to either 40 MPa or a crosshead extension of 10% of the sample height, at a rate of 0.06 mm/min (stresses and strains above these limits resulted in sample fracture). Samples were then analyzed for monoclinic and tetragonal zirconia content with a Panalytical X'Pert Pro Powder X-ray Diffractometer using Cu K-α radiation (Malvern Panalytical, Worcestershire, UK) and with a Renishaw Raman InVia microscope (Renishaw Inc, Wotton-under-Edge, UK) with a 532 nm laser at 10% power under a 50X lens. In the latter, the size of the collection area is dependent on the laser power and lens used

and was kept consistent across all *ex-situ* analyses to be approximately 100μm in diameter.

3.2.3.2 In-situ compression

The *in-situ* experimental setup is shown in Figure 3.1c. Superelastic samples were compressed parallel to the freezing direction using an MTS Criterion Model 43 load frame (MTS Systems Corp., Eden Prairie, MN) to a crosshead extension of 10% of the sample height at a rate of 0.008 mm/min, while a Nikon LU Plan 10X Lens (Nikon, Tokyo, Japan) connected to a 532 nm laser was focused on the curved surface of the cylinder. The probe was connected to a Renishaw InVia Raman spectrometer (Renishaw Inc, Wotton-under-Edge, UK) for analysis. As the sample was compressed, ten spectra were collected at 50% laser power, each with an exposure time of 10 s, and added together. As a result, each measurement took approximately two minutes, equivalent to 0.016 mm of crosshead extension.

3.2.3.3. Diamond anvil cell compression

The diamond anvil cell compression setup is shown in Figure 3.1d. Samples were placed between two diamonds each approximately 1440 μm^2 in area such that the flat faces of the cylinder (perpendicular to the freezing direction) were in contact with each diamond, positioned in an NBS-style diamond anvil cell, and placed in a Renishaw InVia Raman spectrometer[36]. Load was applied by twisting the external screw, so that force was transmitted through the spring and lever to the diamond anvils. The sample was mapped over a 1000 μm^2 area at 50% laser power under a 20X lens. The upper diamond window was aligned with the x-y grid upon which the spectrometer stage moves. Each map was initiated from the same position with respect to the diamond window. Each point on the map was taken on a 20x20 grid, with 50 μm spacing. The screw was then turned to exert pressure on the sample through the diamond anvils. The sample was analyzed before compression had begun, while under compression, and after the compressive load had been removed.

3.2.4. Phase analysis

X-ray diffraction traces were analyzed according to the method outlined by Toraya et al. to calculate the volume fraction of monoclinic phase present in the collection area, V_m[37]. This method utilizes a ratio of the integrated area under the monoclinic and tetragonal peaks to calculate the V_m. Raman spectra were analyzed according to the models and procedures outlined in Chapter II.

3.3. Results and Discussion

3.3.1. Effects of pH on CeO_2-ZrO_2 powder morphology

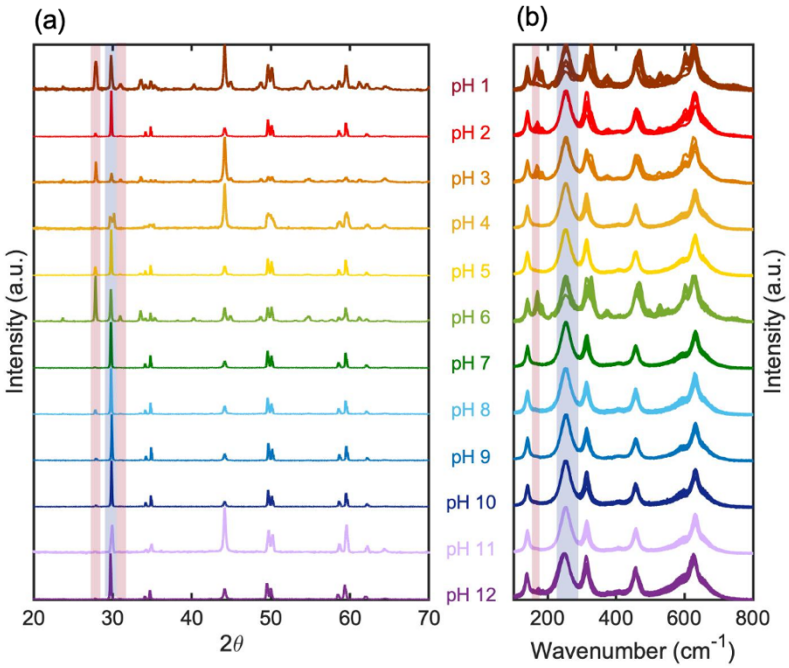

Figure 3.2. Sintered CSZ pellets were prepared in sol-gel solutions of pH ranging from 1-12. (a) XRD and (b) Raman spectra of sintered CSZ pellets. Monoclinic peaks used for quantitative phase analysis are highlighted in red, and tetragonal peaks are highlighted in blue.

One of the benefits of incorporating a sol-gel processing step into the freeze casting procedure for CSZ honeycombs is that the sol-gel synthesis introduces a lever of

control over the ceria-zirconia powder characteristics. To investigate how changing the pH of the aqueous solution used in the sol-gel synthesis might impact phase composition of the resulting CSZ, the sintered pellets were analyzed using XRD and Raman spectroscopy, as seen in Figure 3.2. These spectra revealed that all of the 12.5 mol% CSZ samples, regardless of pH, were primarily tetragonal in phase content. While some samples did also exhibit some monoclinic phase content, it was unclear whether this was attributable to the variances in pH or to martensitic transformation as a result of stresses induced during sample preparation. However, as all samples studied exhibited strong tetragonal character in their Raman spectra, it did not appear that altering the pH of the sol-gel synthesis solution significantly hindered the stabilization of the tetragonal phase in the CSZ samples.

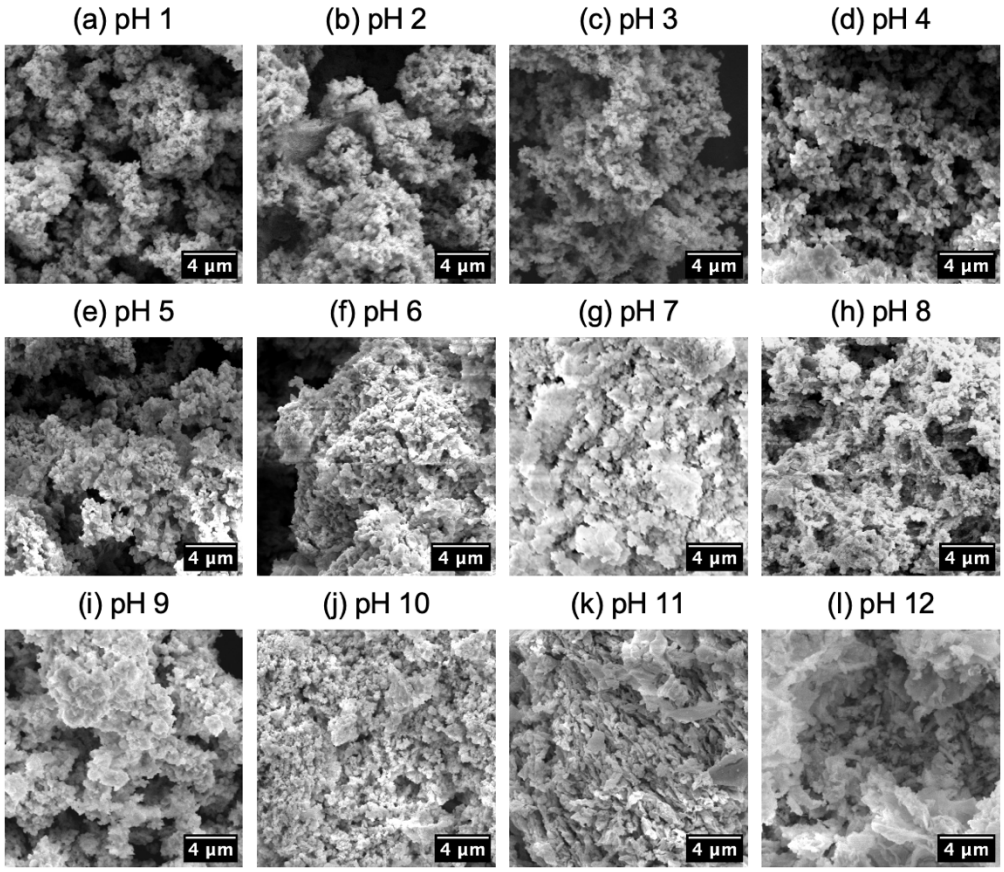

Figure 3.3. SEM images of CeO_2-ZrO_2 powders after calcination, prepared in sol-gel solutions of the indicated pH.

Altering the pH of the solution of the sol-gel synthesis did, however, alter the morphology of the CeO_2-ZrO_2 powders, as seen in Figure 3.3. The powders prepared at low pH values exhibited spherical morphologies. Conversely, powders prepared from high-pH sol-gel solutions appeared much more sheet-like, especially those prepared at pH 11 (Figure 3.3k) and pH 12 (Figure 3.3l). Those prepared at neutral pH (Figure 3.3g), like the CeO_2-ZrO_2 powders used to prepare all freeze-cast samples later in this chapter, still exhibited some spherical morphology, but appeared more interconnected than did those prepared in more acidic solutions. This effect of pH on particle morphology has potential implications for the freeze casting process: as powder suspensions are freeze cast directionally, spherical and sheet-like powders are likely may give rise to different sintered microstructures. As the honeycomb-like pore network is crucial to the ability of a polycrystalline CSZ sample to accommodate the martensitic transformation, different microstructures may yield samples with different mechanical behavior.

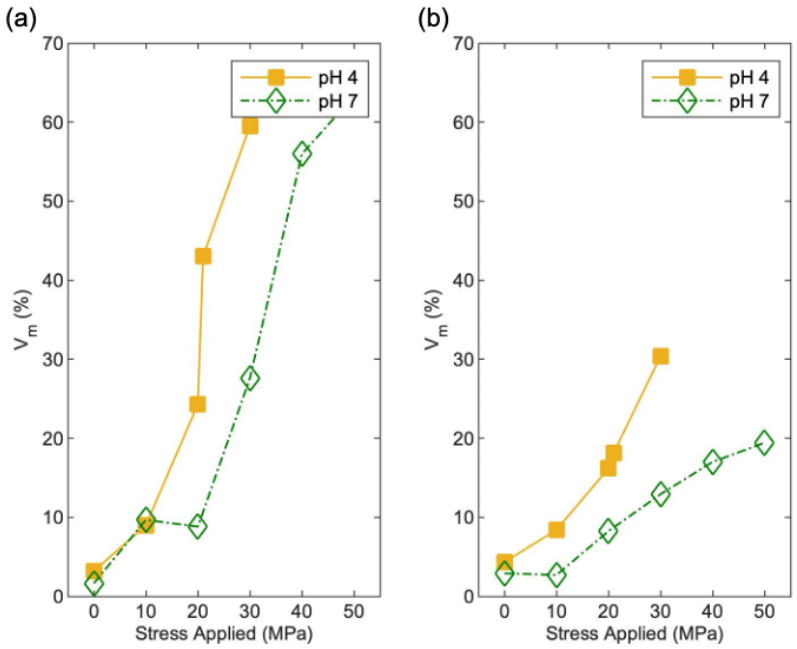

Figure 3.4. V_m as calculated through XRD of the top (a) and bottom (b) faces of ceria-stabilized zirconia honeycombs prepared in pH 4 and pH 7 solutions as a function of compressive stress.

To test this, powders prepared at different pH values during the sol-gel synthesis were freeze cast into honeycombs and compressed to at least 30 MPa, with the monoclinic phase content then analyzed using X-ray diffraction (Figure 3.4). The preliminary results from these tests indicated that samples prepared under different pH conditions transformed from the tetragonal to the monoclinic phase at different applied stresses: samples prepared in pH 4 solution exhibited higher monoclinic phase contents than did samples prepared in pH 7 solutions after compression to the same stress. While this trend was observed on both faces of the samples, further studies are needed to determine whether this effect is replicable over multiple compression cycles, and whether samples prepared from powders synthesized in basic solutions also behave differently to those prepared in neutral solutions.

3.3.2. Microstructure of shape memory and superelastic porous ceria-stabilized zirconia solids

Scanning electron microscopy images of the samples revealed the honeycomb-like pore network that permits observation of shape memory and superelastic behavior in polycrystalline porous zirconia (Figure 3.5). When cut perpendicular to the freezing axis, samples exhibited columnar pores (Figure 3.5a and b), a result of freezing the suspensions at the relatively low freezing front velocity of 1 mm/s[35]. This honeycomb-like pore network increased the surface area to volume ratio of these samples, in contrast to a fully dense sample of the same size. When cut parallel to the freezing axis, the width of the pore walls was further emphasized (Figure 3.5c). The pore walls were not only thin enough to accommodate the volume expansion that accompanies the martensitic transformation, but were also roughly parallel to each other, as expected in a honeycomb-like structure. When compressed along an axis parallel to that of the freezing front velocity, each pore wall should be aligned with the axis of compression.

A closer look at one of the pore walls revealed a bamboo-like distribution of grains (Figure 3.5c) in which the pore wall was roughly one grain across, mimicking the

oligocrystalline micropillars from earlier shape memory studies[10, 12, 13, 18]. Also notable is the distribution of grain sizes represented at this magnification, on the order of 0.5 μm to 8 μm. As grains of different size and orientation transform from the tetragonal phase to the monoclinic phase at different critical stresses[12], the diversity of grain sizes and orientations in these samples led to the martensitic transformation over a broad range of stresses.

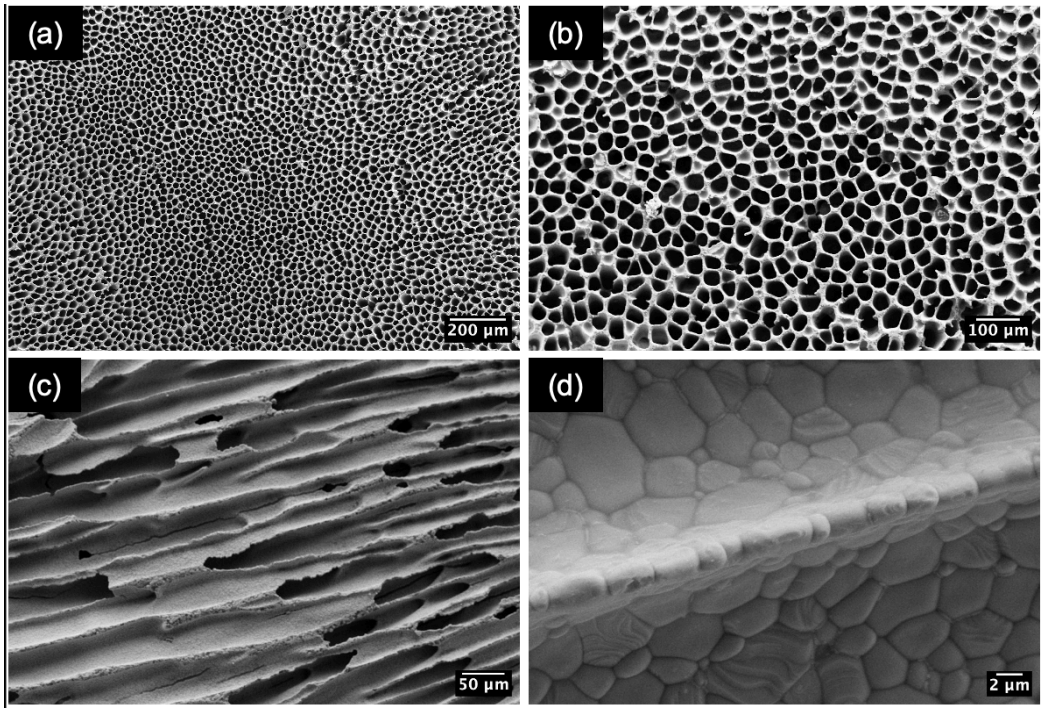

Figure 3.5. Scanning electron microscope images of freeze-cast 12.5 mol% ceria-stabilized zirconia cut (a,b) perpendicular to the freezing direction and (c,d) parallel to the freezing direction.

3.3.3. Shape memory zirconia

3.3.3.1. Compression-induced shape memory effects

Freeze-cast porous zirconia doped with 12.5 mol% CeO_2 were loaded under uniaxial compression to observe shape memory effects in ceria-stabilized zirconia honeycombs. As 12.5 mol% CSZ samples were subjected to increasing compressive

load, XRD patterns collected after compression revealed the incremental change in phase composition. With the resultant increasing compressive stress, the monoclinic peaks at 2θ = 28° and 31° increased in intensity with respect to the tetragonal peak at 2θ = 30° (Figure 3.6a). Stresses as low as 10 MPa were sufficient to induce the martensitic transformation in some grains of the sample by virtue of their size or orientations. Results confirmed that the martensitic transformation had taken place as the sample was compressed and increased with increasing applied stress.

A typical stress-strain plot of the sample when compressed to 8.5% strain was consistent with shape memory behavior (Figure 3.6b). There was a significant non-linearity in the stress-strain curve at stresses approximately 40 MPa, implying that the martensitic transformation was taking place in numerous grains in the sample. Notably, this region of the stress-strain plot was neither horizontal nor linear, as would be expected of a single grain undergoing a martensitic transformation. Rather, in this polycrystalline sample, the loading portion of the shape memory effect appeared as a series of individual transformations. The critical stress at which a single grain transforms not only depends on grain size and local dopant concentration, but also on the resolved stress on the transformation shear plane, based upon the crystal orientation of the grain[12, 14, 15, 38]. As a result, the observed transformation stress varied widely. The residual strain (~3%) after the compressive stress was removed further indicated that the monoclinic phase was retained on unloading, also consistent with the shape memory effect. After a single loading and unloading cycle, it is important to note that the sample exhibited a higher stiffness than the starting fully tetragonal sample (as calculated from the slopes of the linear regions of the loading and unloading sections of the stress-strain curve, Figure B.1). This is consistent with first-principles calculations of the moduli of monoclinic and tetragonal zirconia, in which the former was found to be marginally stiffer[39].

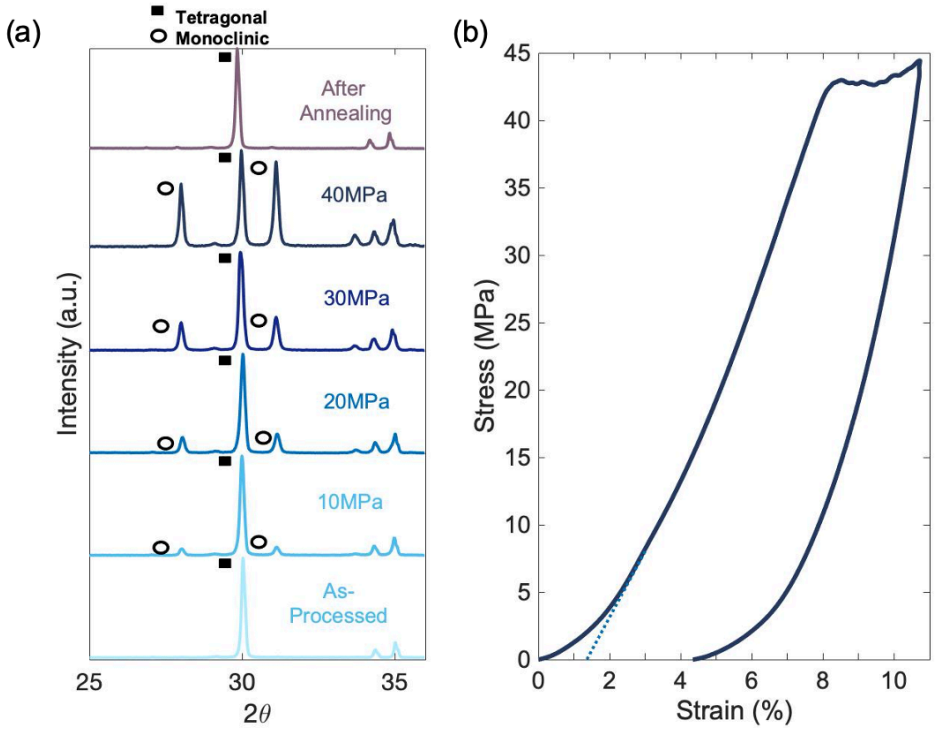

Figure 3.6. Shape memory behavior in 12.5 mol% CSZ. (a) XRD patterns of 12.5 mol% CSZ reveal the extent of the transformation as a function of stress. (b) A stress-strain plot of a 12.5 mol% CSZ sample under compression exhibits non-linearity in the stress-strain curve characteristic of a martensitic transformation between ~7.2% and ~9.3% strain as calculated from the ratio of the crosshead extension to the initial sample height. The non-linearity between 0 and 1.4% strain is attributed to sample adjustments in the loading fixture, and the dashed line indicates extrapolated value of the stress-strain curve without this non-linearity.

The XRD pattern of the sample after annealing at 700 °C for 2 hours (Figure 3.6a) was nearly identical to that of the sample before compression, indicating that the martensitic transformation was reversible on heating. Crucially, that the sample only returned to its initial state on heating further confirms that a shape memory behavior is in effect: the samples were transformed on the application of stress, remained transformed even after that stress is removed, and only returned to their initial state when heated to 700 °C.

Together, the XRD patterns and the stress-strain plot tracked the extent of the martensitic transformation with increasing loads across a large surface area of the sample. However, given that the stress-strain plot provided data from the entire sample, and XRD analysis from millimeter-wide areas of the sample, they did not necessarily provide a rigorous look at grain-size transformations (on the order of microns) over the course of the experiment. For a closer look, then, we turned to Raman spectroscopy. A complementary technique to XRD, Raman spectroscopy affords data collection from smaller spot sizes than does XRD. Additionally, Raman spectroscopy allows for more flexible sample arrangements as the coupled optical microscope ensures suitable focus on the sample and is thus more easily compatible with *in-situ* experimental setups such as those shown in Figure 3.1c and 3.1d.

3.3.3.2. Shape memory effects over multiple cycles

Using the analysis techniques outlined in section 3.2.4, we compared the monoclinic volume fraction, V_m as determined from XRD and through Raman analysis as a 12.5 mol% CeO_2 sample was compressed over multiple cycles (Figure 3.7). The V_m from XRD was plotted on the left-hand side of Figure 3.7 and reports the phase content of an area on the order of 50 mm^2. The analysis using Raman spectroscopy was plotted on the right-hand side of Figure 3.7, where each sample was scanned in 100 different 1 μm^2 regions across the same face that was examined through XRD. The V_m of each spectrum, calculated using the above method, was assigned a color on a spectrum from blue ($V_m = 0$, entirely tetragonal) to red ($V_m = 1$, entirely monoclinic). Each square in the resulting colormap corresponded to one spectrum representing a $1mm^2$ area of the sample. It is critical to note that samples were moved between the compression fixture, X-ray diffractometer, and Raman spectrometer (Figure 3.1b), and thus the specific locations scanned in the Raman spectrometer varied between cycles. As a result, the location of the squares in the colormap did not correspond to the same location on the sample over every point of analysis.

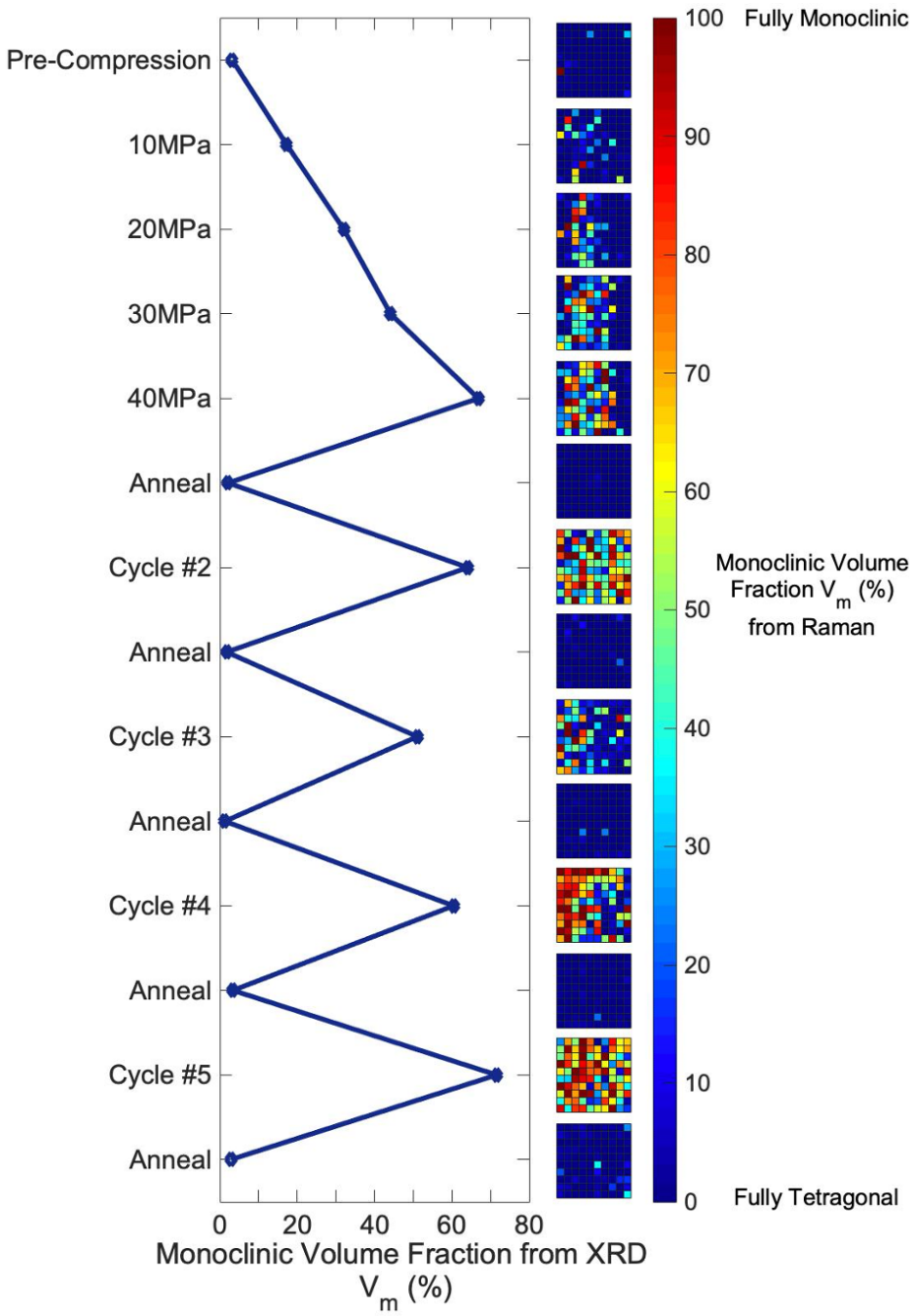

Figure 3.7. Monoclinic volume fraction (V_m) as calculated by XRD (left) and Raman spectroscopy (right) as a function of loading and annealing cycle for 12.5 mol% CSZ. The color of individual pixels on the colormap is assigned based on the V_m value of the corresponding spectra, with blue representing fully tetragonal spectra (V_m = 0) and red representing fully monoclinic spectra (V_m = 1).

Overall, both techniques described the same trend: the monoclinic content present in the sample increased as stress is applied and returned to almost zero after annealing. This behavior is repeated over multiple cycles. However, the V_m values described in the Raman colormaps provided more site-specific detail than was possible through XRD analysis alone. Colormaps corresponding to the maximum strain, as seen in the stress-strain plot in Figure 3.6b, exhibited regions of fully tetragonal character, indicating that the entirety of the sample had not transformed even with strains approaching 10%. This reinforced the observations of the stress-strain plot shown in Figure 3.6b: these complex, polycrystalline systems were comprised of many grains that transform at different critical stresses. Conversely, colormaps taken after annealing exhibited regions with largely tetragonal character, but still retained a small number of regions with some monoclinic character. This is evident in the colormap collected following the final anneal in Figure 3.7, where regions on the bottom right corner of the colormap revealed 35% monoclinic phase had been retained.

3.3.3.3. Location effects on shape memory behavior

Raman spectroscopy was then utilized to probe the uniformity of the martensitic transformation across multiple faces of the sample. Using the semicylindrical sample shown in Figure 3.1a, the sample was exposed to the same compression and annealing cycles and analysis. Three faces of the sample were scanned: the top and bottom (faces perpendicular to the freezing direction), and side (a face parallel to the freezing direction). The semicylindrical samples were cut to have three flat faces for analysis through Raman spectroscopy: two faces perpendicular to the freezing direction (top and bottom) and one parallel to the freezing direction (side). The same trends were observed in Figure 3.8 as were seen in Figure 3.7 (where a face perpendicular to the freezing direction was analyzed) of increasing V_m with increasing stress, a nearly complete return to the tetragonal phase after annealing, and the ability to perform this shape memory behavior over several cycles.

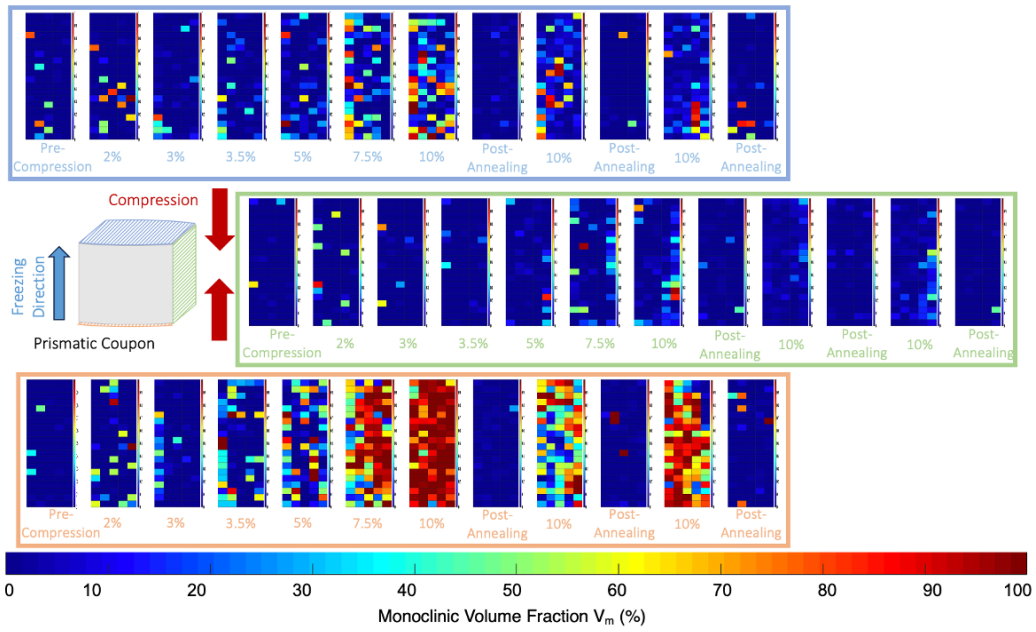

Figure 3.8. Monoclinic volume fraction as calculated through the rule of mixtures approach across three faces of the same 12.5 mol% CSZ sample: the face in contact with the top platen (blue), the face in contact with the bottom platen (orange), and the face parallel to the freezing direction (green), which only contacted the platens at the top and bottom edges. Each face was analyzed before compression, then after compression as a function of strain. After compression, the sample was annealed, analyzed, and the cycle of compression and analysis was repeated twice more.

While all three sides observed exhibited the same general trend, they did so to varying extents. The bottom surface exhibited some regions that had fully transformed to the monoclinic phase, but fewer were seen on the top surface. The side parallel to the pore orientation and freezing direction exhibited limited regions of complete transformation. This difference in behavior, if not a trend, across these separate locations on the sample further underscored the complexity of polycrystalline materials in addition to the anisotropy of the structure. Factors including the size of grains, orientation of grains, thickness of pore walls, and local stresses under

compression, such as those from contact stresses on surfaces adjacent to the loading platens, all influenced the critical stress at which grains in the sample transform.

It is noteworthy that the side of the sample parallel to the freezing direction transformed to a lesser extent than the two faces perpendicular to the freezing direction, implying that either stresses were significantly lower than those experienced on the orthogonal top and bottom planes, or that grains were oriented in unfavorable directions for the transformation. Stresses can be estimated by treating the sample as a compressed solid cylinder fixed between beveled washers [40, 41], and with this, a simpler explanation should also be considered. Raman spectroscopy only penetrates a few micrometers into the sample beginning at the free surface, while the sample under study is approximately 4 mm thick. The free surface remained stress-free under load, and as such, will likely experience a lesser fraction of grains transformed. Alternatively, grains in the interior of the cylinder under compression experienced greater stress than those on the free surface increasing their probability of transformation but were positioned too far from the Raman probe for analysis.

With porous zirconia honeycombs, shape memory behavior was observed in a polycrystalline ceramic over several cycles and tracked how different regions of the sample transformed. As complex systems comprised of many thousands of grains, the porous ceria-stabilized zirconia ceramics combined the individual transformation events of the many grains into one bulk-scale transformation, as is seen in stress-strain curves and monoclinic content colormaps, and overall monoclinic content as calculated by XRD. With the use of Raman spectroscopy, the spatial homogeneity of phase transformations and the effects of structural features such as pores, surfaces, and edges on the degree of transformation and in these polycrystalline zirconia honeycombs are better understood.

3.3.4. Superelastic zirconia

3.3.4.1. Ex-situ compression experiments

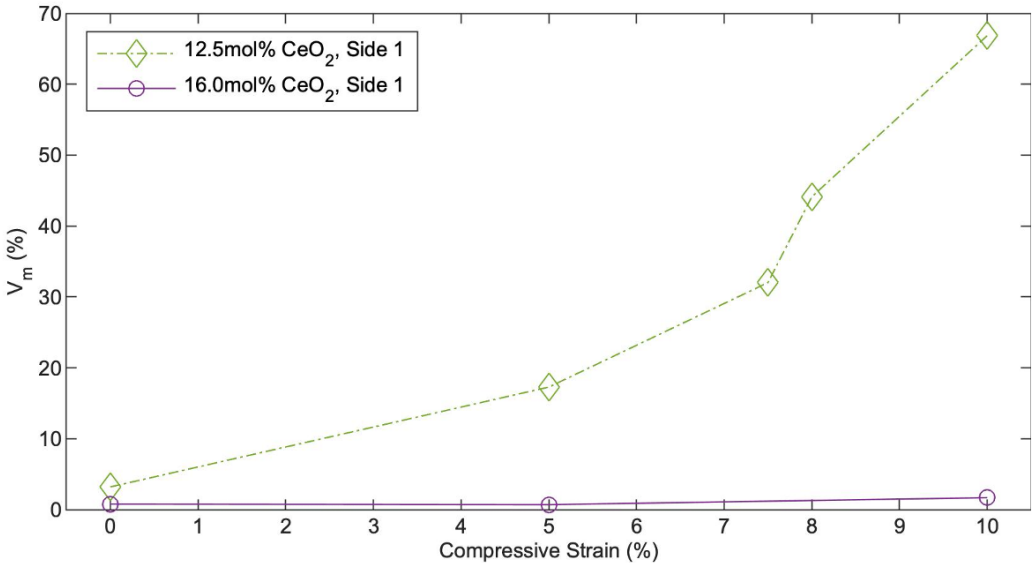

Figure 3.9. Monoclinic volume fraction (V_m) of 12.5 mol% (green) and 16.0 mol% (purple) ceria-stabilized zirconia honeycombs as they are compressed in increments up to 10% crosshead extension as determined using XRD.

Having observed the shape memory effect in a 12.5 mol% CeO_2-stabilized ZrO_2 sample over several cycles, the same analytical techniques were used to observe superelastic behavior in a 16.0 mol% CeO_2-stabilized ZrO_2 sample. As with the shape memory sample, the superelastic sample was compressed, and analyzed using *ex-situ* XRD at various increments until 10% crosshead extension was reached (Figure 3.9). Unlike the shape memory sample, which exhibited increasing V_m as the sample is compressed to greater extensions, the superelastic sample showed no increase in V_m, even after compression to 10% of the crosshead extension.

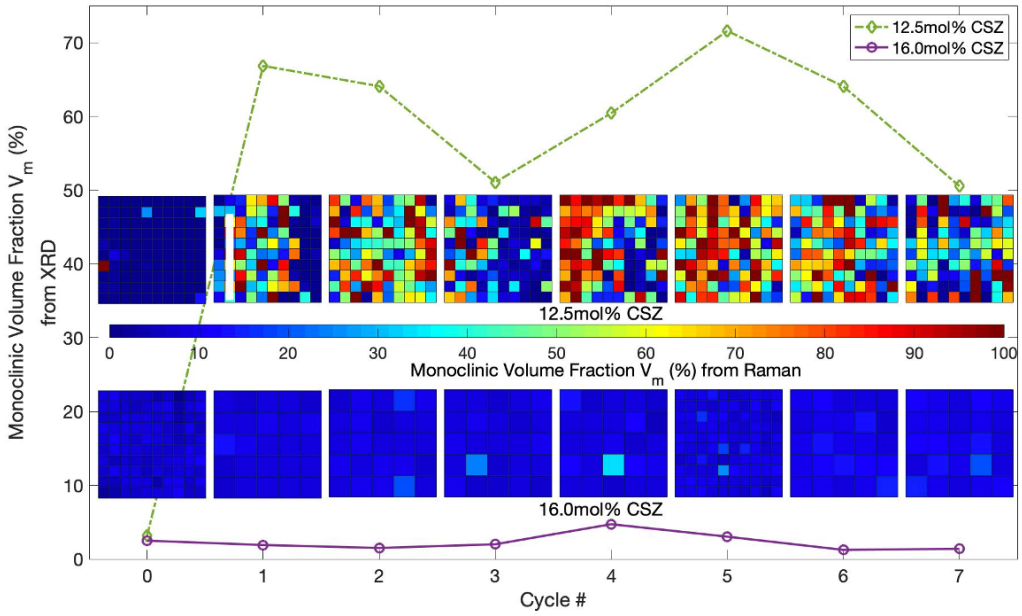

Figure 3.10. Monoclinic volume fraction (V_m) as determined from XRD (plot) and Raman spectroscopy (colormaps) for cylindrical 12.5 mol% (shape memory) and 16.0 mol% (superelastic) CeO_2-stabilized ZrO_2 samples upon unloading after compression. The corresponding colormaps are shown in the upper row for the 12.5 mol% sample and the lower row for the 16.0 mol% sample. After each compression cycle, the 12.5 mol% samples were annealed (post-annealing colormaps shown in Figure 3.7).

This behavior was additionally replicable over many cycles. The superelastic samples were then compressed to 10% crosshead extension over seven cycles times and analyzed through XRD and Raman spectroscopy in between each compression cycle, as shown in Figure 3.10. The behavior of the superelastic samples again sharply contrasted with that observed in the shape memory samples, also shown in Figure 3.10. After the load was removed, very little monoclinic character was observed in the superelastic composition using both XRD and Raman spectrometry color maps, which appeared in all blue shades. This is to be expected from a material exhibiting stress-induced superelastic behavior: the sample should transform while under load, then return to its original state as soon as the load is removed. However, the presence of the monoclinic phase under load could not be observed in these samples using the

ex-situ experimental setup seen in Figure 3.1b. Consequently, an *in-situ* experimental setup (Figure 3.1c) was next used to detect the sample's transformation to the monoclinic phase.

3.3.4.2. In-situ compression experiments

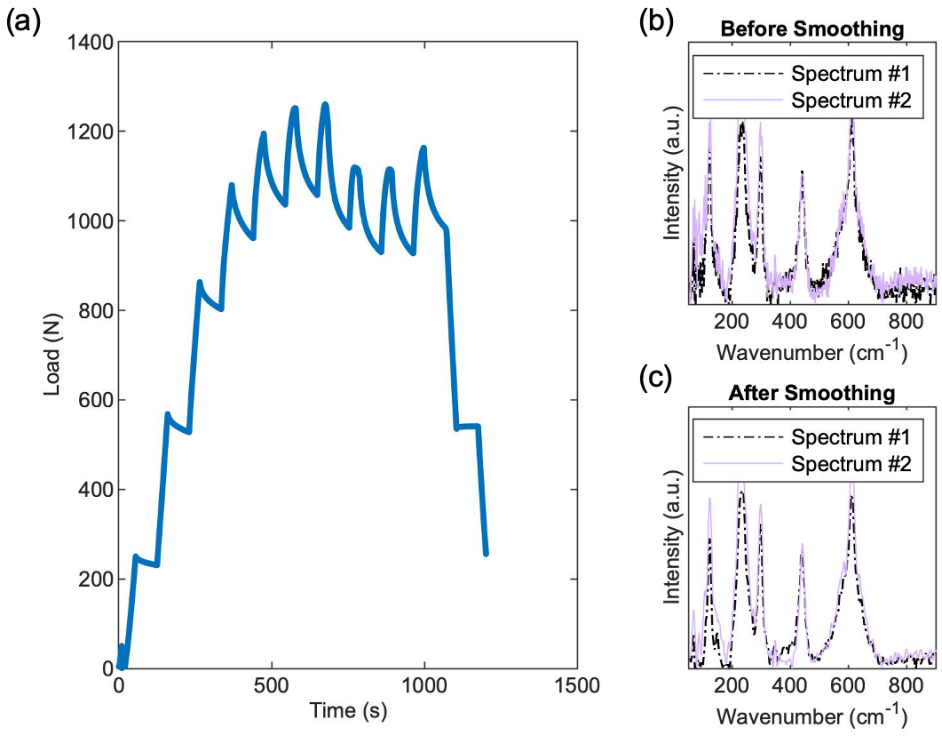

Figure 3.11. In-situ compression experiments using the setup shown in Figure 3.1c. (a) A loading profile with two-minute holds for spectral analysis shows significant relaxation of the sample when not under continuous compression. (b) Raman spectra collected during continuous compression runs exhibit large amounts of noise and are then (c) smoothed with a Savitzky-Golay filter.

In the *in-situ* compression setup, a Raman probe was focused on a sample undergoing compression in a load frame, so that the phase content of the samples under load could be analyzed. With this arrangement, Raman spectra could be correlated to specific points on the stress-strain curve. As the sample was compressed, spectra were collected continuously from a stationary position on the side of the sample

parallel to the freeze casting direction (Figure 3.1c). While holding the crosshead at a stationary extension during spectra collection would have allowed for the collection of more accumulations of each spectrum, tests in which compression was paused for two minutes showed significant relaxation of the samples (Figure 3.11a) due to insufficient stiffness of the sample setup.

Consequently, it was necessary to collect spectra during a slow, continuous compression profile. This required balancing the number of spectra collected with the number of accumulations and exposure time for each spectrum—while collecting more spectra provided more granular detail on the transformation over the compression cycle, it limited the number of accumulations and exposure time for each spectrum. As a result, the spectra contained more experimental noise than was ideal, since traditional Raman spectrometer setups allow for easier minimization of noise than did the *in-situ* compression setup. In addition to the increased experimental background in each spectrum due to the high Ce doping content of the superelastic samples, the presence of experimental noise complicated the analysis of the spectra collected from this setup.

There are several methods of minimizing noise, including increasing the number of times spectra are added together during the collection process, optimizing focus, and using filters to smooth the finished data[42]. However, this *in-situ* experimental setup limited the first two minimization strategies. To catch small changes in phase content over the course of the collection cycle, each spectrum had to be taken as quickly as possible, limiting the number of accumulations possible. Furthermore, the need to prevent collisions between the probe and the load frame fixtures prevented focusing lenses with short focal distance. These two settings were optimized to find conditions yielding spectra with the greatest intensity. The final spectra, examples of which are seen in Figure 3.11b, had a Savitzky-Golay filter applied (Figure 3.11c) to further reduce the remaining noise, sufficient to track superelastic behavior in ceria-stabilized zirconia systems[42].

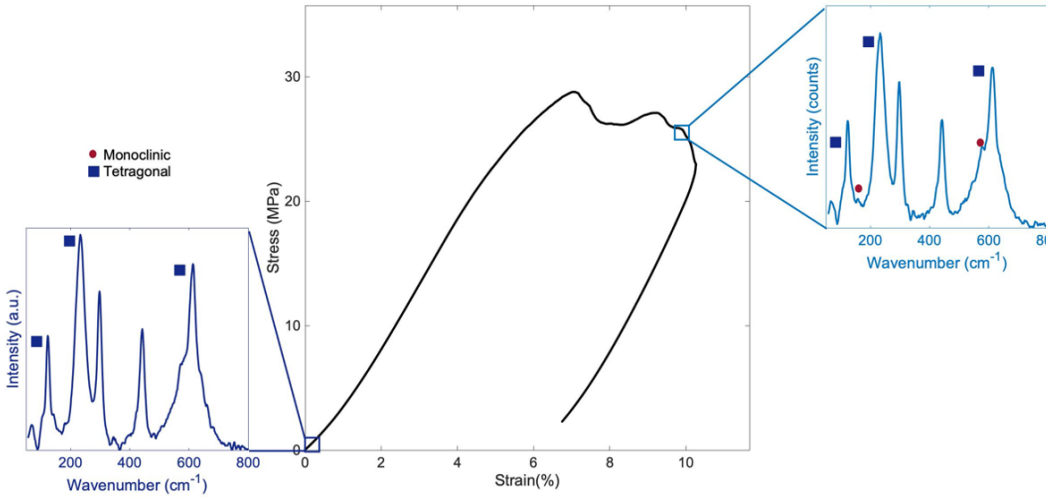

Figure 3.12. Stress-strain plot of a 16.0 mol% ceria-stabilized zirconia honeycomb under compression in the in-situ experimental setup, with Raman spectra corresponding to low (0 MPa and 0% strain) and high (25 MPa and 9.5% strain) stresses during the compression cycle. The programmed compression profile of the crosshead did not enable the crosshead to return to a zero-stress state after compression. Monoclinic peaks considered for analysis are indicated by a red circle (●) and tetragonal peaks considered for analysis are indicated by a blue square (■). Peaks around 315 cm-1 and 460 cm-1, which correspond to the tetragonal phase, were not considered, as they are too close to the monoclinic peaks 330 cm-1 and 465 cm-1 to be easily deconvoluted.

The stress-strain plot of the compression indicated that a martensitic transformation had taken place, as the non-linearity in the stress-strain curve implies (Figure 3.12). The stress-strain plot collected resembled that collected from the *ex-situ* setup with 16 mol% ceria (Figure B.2), confirming that the same behavior was observed on the two different experimental setups. The Raman spectra in Figure 3.12 exhibited slight changes in the regions of the spectra that contain monoclinic peaks. While those variations were small, the calculated V_m of the spectrum corresponding to 0 MPa was 0%, whereas the calculated V_m of the spectrum corresponding to 27 MPa was found to be about 6.0%. While the difference between the calculated V_m from the zero- and high-stress spectra was small, it did fit into the pattern observed in the shape memory

samples collected from the sides of the samples parallel to the freezing direction. In those samples, Raman spectra collected from those sides exhibited far less monoclinic content than did those collected from the two faces perpendicular to the freezing direction (Figure 3.8) for reasons discussed earlier in Section 3.3.3.3.

3.3.4.3. Diamond anvil cell compression experiments

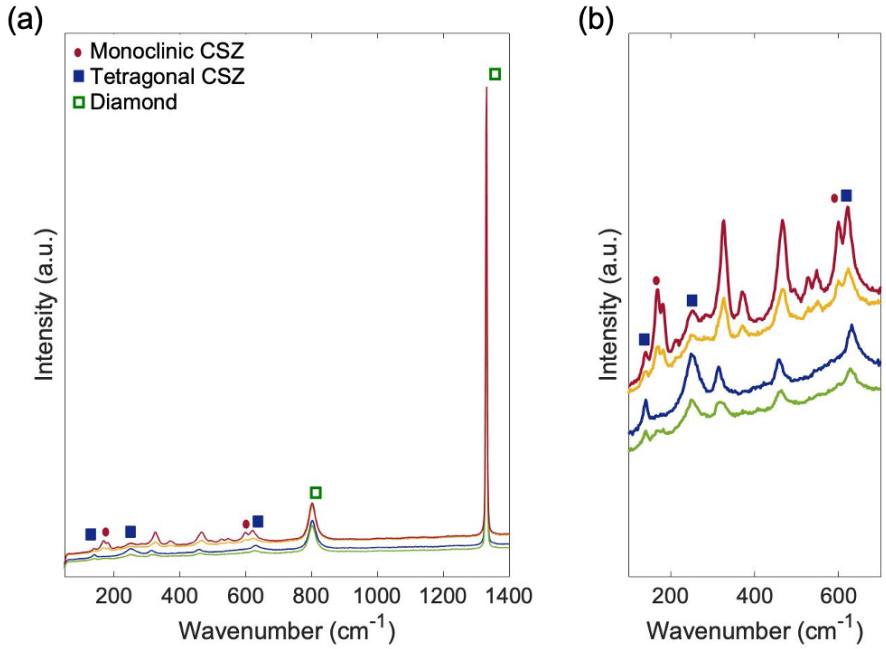

Figure 3.13. Raman spectra of 12.5 mol% CSZ were collected through the diamond window of the diamond anvil cell. (a) When the spectrum between 100 cm^{-1} and 1400 cm^{-1} is considered, a significant diamond peak is observed around 1330 cm^{-1}. (b) When only the region of the spectrum between 100 cm^{-1} and 700 cm^{-1} is considered, both tetragonal and monoclinic spectra are visible under the diamond window.

To complement observations from surfaces parallel to the freezing direction, a cylindrical sample was placed in an NBS-style diamond anvil cell (Figure 3.1d). Here, the top surface (perpendicular to the freezing direction) could be scanned through the 1.44 mm^2 diamond window before, during, and after the application of the compressive force parallel to the freezing direction. Spectra collected from a 12.5

mol% CSZ sample through the diamond window containing both monoclinic and tetragonal regions revealed that, despite the intensity of the diamond peak at 1330 cm^{-1} (Figure 3.13a), both monoclinic and tetragonal spectra were visible in the region between 100 cm^{-1} and 700 cm^{-1} (Figure 3.13b).

A 1 mm by 1 mm area of a 16 mol% CSZ sample under the diamond was scanned, and the V_m of the resulting spectra are represented in 20 by 20 square colormaps (Figure 3.14). Prior to compression, the area mapped was found to consist of highly tetragonal CSZ, as seen in Figures 3.14a, 3.14d, and 3.14g. This was consistent with the colormap corresponding to cycle 0 in Figure 3.10, which described the monoclinic content of 16.0 mol% ceria-stabilized zirconia samples before compression.

Evidence of a superelastic transformation was substantiated when the CSZ phases were mapped during compression. In Figures 3.14b, 3.14e, and 3.14h, there was clear evidence for an increase in V_m in both the colormap of the highlighted section shown in the center column, and in the presence of monoclinic peaks in the corresponding Raman spectrum. That only a small (0.1 μm^2) region of the sample exhibited a noticeable increase in V_m was consistent with the behavior seen in the *in-situ* experiment (Figure 3.12) and with the *ex-situ* experiments conducted on 12.5 mol% ceria-stabilized zirconia (Figure 3.7). In both, it was observed that some regions of the sample do not transform from tetragonal to monoclinic even under high stresses. In all of these cases, the transformation behavior could be attributed to grain size and orientation.

Superelastic behavior in 16.0 mol% ceria-stabilized zirconia was further confirmed with mapping of the same area under the diamond window after the compressive load was removed. Regions of the sample that while under compression showed clear increases in V_m (Figure 3.14e) exhibited little-to-no monoclinic CSZ evidence after the diamond anvil is withdrawn (Figure 3.14f), consistent with the trends shown in Figure 3.10.

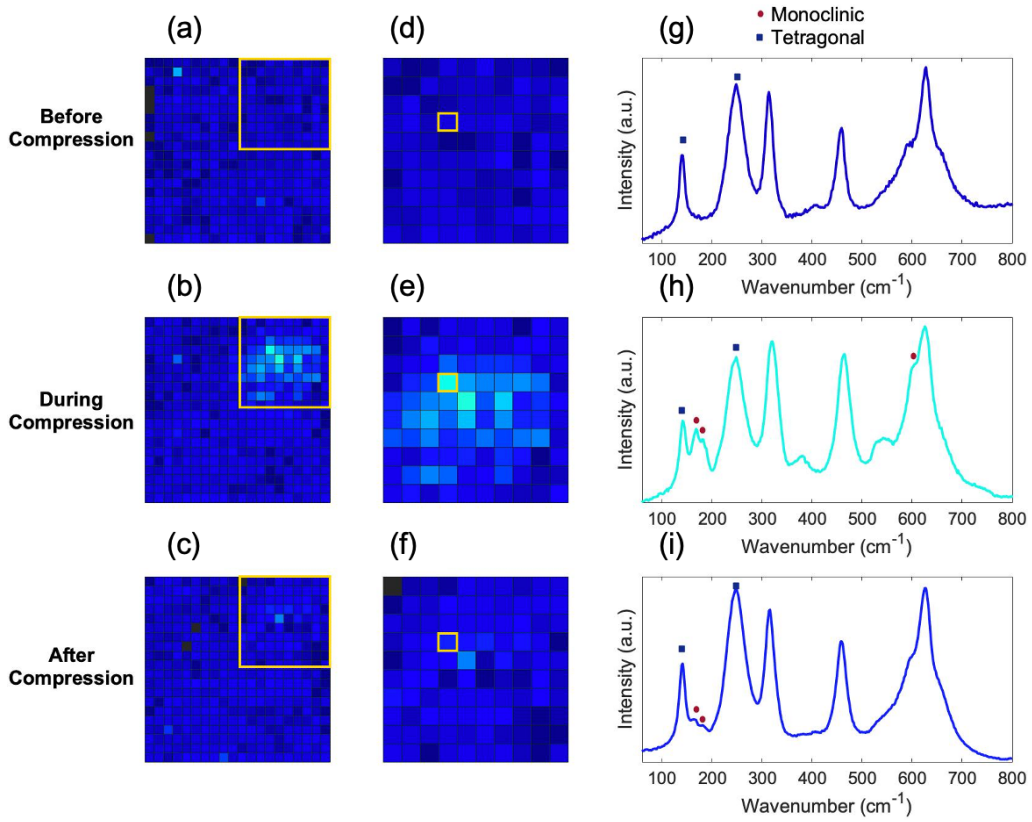

Figure 3.14. Colormaps corresponding to 1 mm by 1 mm areas (a-c) of a cylindrical 16.0 mol% CSZ sample (perpendicular to the freezing direction) in the diamond anvil cell fixture seen in Figure 3.1d. The highlighted squares are shown in greater magnification (d-f) and represent an area of approximately 0.5 mm by 0.5 mm. The spectra that correspond to the highlighted squares (g-i) are shown with monoclinic peaks marked with a red circle (●) and tetragonal peaks marked with a blue square (■). The sample was measured before compression (a,d,g), during compression (b,e,h), and after compression (c,f,i).

Based upon *ex-situ* and *in-situ* experimental results, the presence of the monoclinic phase in compression in the 16.0 mol% CSZ confirms that these samples underwent the martensitic phase transformation required for superelastic behavior. The non-linearity in the stress-strain curve upon transformation coupled with transformation from tetragonal to monoclinic and back to tetragonal on application and removal of load over several cycles provided clear evidence for superelasticity in the ceria-

stabilized zirconia porous structures. Overall, the diamond anvil compression setup presented a novel method for tracking superelastic effects in polycrystalline ceria-stabilized zirconia. While only small regions can be mapped at once, and pressure calibration is challenging due to the lack of a pressure-transmitting medium in this arrangement, clear phase changes can nonetheless be observed and used for confirmation of superelastic behavior in bulk-scale porous zirconia.

3.4. Summary

This work presented shape memory, and for the first time, superelastic behavior of freeze-cast, ceria-stabilized zirconia, polycrystalline honeycombs over multiple cycles. To probe these transformations in greater detail than X-ray diffraction allows, the process to quantitatively analyze the phase content through Raman spectra developed in Chapter II was used to explore regions on the order of one to two cells of the honeycomb and behavior across multiple faces of a sample both parallel and perpendicular to the freezing direction. Such studies provided insight into the spatial homogeneity of the transformations and their local reversibility on cycling.

The use of Raman spectroscopy also enabled the coupling of alternative compression systems, such as the experimental *in-situ* setup with a mechanical testing machine and the diamond anvil compression cell with phase identification. The stress-strain plots from the *in-situ* and *ex-situ* setups exhibit similar trends, indicating that the two experimental techniques were complementary. While the *in-situ* setup utilizing the external Raman probe and load frame presented several challenges, it has the potential to track martensitic transformations in these complex polycrystalline systems with further optimization: altering platen design or lens choice to better accommodate the probe while the sample is undergoing compression and improve focus without risking damage to the probe as the platens move closer together. The versatility of Raman spectroscopy further allowed for the use of more spatially restrictive compression fixtures, such as diamond anvil cells, as the optical microscope coupled to the spectrometer ensured correct focus on the sample. The use

of an NSB-style diamond anvil cell allowed for the observation of monoclinic phase in 16.0 mol% CSZ only while compression is applied—once the compression was removed, regions of the sample that had previously exhibited clear monoclinic character reverted to the tetragonal phase.

Ultimately, the demonstration of shape memory and superelastic behavior in bulk structures of polycrystalline zirconia-based ceramics opens a wealth of opportunities for future exploration into tailored porous microstructures. Through these techniques, the effects of pore size or alternate pore geometries on martensitic transformations in zirconia ceramic systems can be explored in greater detail, enabling their future use as shape memory actuators or superelastic dampeners in high-temperature or corrosive environments.

3.5. References

1. Swain, M.V. Shape Memory Behaviour in Partially Stabilized Zirconia Ceramics. *Nature*. 1986;322(6076):234–236. https://doi.org/10.1038/322234a0.
2. Reyes-Morel, P.E., Cherng, J.S., Chen, I-W. Transformation Plasticity of Ceria-Stabilized Tetragonal Zirconia Polycrystals: II. Pseudoelasticity and Shape Memory effect. *J Am Ceram Soc*. 1988;71:648–57. https://doi.org/10.1111/j.1151-2916.1988.tb06383.x.
3. Garvie, R.C., Hannink, R.H., Pascoe, R.T. Ceramic Steel? *Nature*. 1975;258(5537):703–704. https://doi.org/10.1038/258703a0.
4. Bansal, G.K., Heuer, A.H. On a Martensitic Phase Transformation in Zirconia (ZrO_2)—I. Metallographic Evidence. *Acta Metall*. 1972;20(11):1281–1289. https://doi.org/10.1016/0001-6160(72)90059-4.
5. Bansal GK, Heuer AH. On a Martensitic Phase Transformation in Zirconia (ZrO_2)—II. Crystallographic Aspects. *Acta Metallurgica*. 1974;22(4):409–417. https://doi.org/10.1016/0001-6160(74)90093-5.
6. Hannink, R.H.J. Growth Morphology of the Tetragonal Phase in Partially Stabilized Zirconia. *J Mater Sci*. 1978;13:2487–96. https://doi.org/10.1007/BF00808066.
7. Reyes-Morel, P.E., Chen, I-W. Transformation Plasticity of Ceria-Stabilized Tetragonal Zirconia Polycrystals: I. Stress Assistance and Autocatalysis. *J Am Ceram Soc*. 1988;71:343–53. https://doi.org/10.1111/j.1151-2916.1988.tb05052.x.
8. Swain, M.V., Hannink, R.H.J. Metastability of the Martensitic Transformation in a 12 mol% Ceria-Zirconia Alloy: II. Grinding Studies. *J Am Ceram Soc*. 1989;72:1358–654. https://doi.org/10.1111/j.1151-2916.1989.tb07652.x.
9. Hayakawa, M., Oka, M. Structural Study on the Tetragonal to Monoclinic Transformation in Arc-Melted Zirconia-2 mol.% Yttria. II. Quantitative Analysis. *Acta Metall*. 1989;37:2229–35. https://doi.org/10.1016/0001-6160(89)90149-1.

10. Lai, A., Du, Z., Gan, C.L., Schuh, C.A. Shape Memory and Superelastic Ceramics at Small Scales. *Science*. 2013;341(6153):1505–1508. https://doi.org/10.1126/science.1239745.
11. Camposilvan, E., Torrents, O., Anglada, M. Small-Scale Mechanical Behavior of Zirconia. *Acta Mater*. 2014;80:239–249. https://doi.org/10.1016/j.actamat.2014.07.053.
12. Du, Z., Zeng, X.M., Liu, Q., Lai, A., Amini, S., Miserez, A., Schuh, C.A., Gan, C.L. Size Effects and Shape Memory Properties in ZrO_2 Ceramic Micro- and Nano-Pillars. *Scr Mater*. 2015;101:40–43. https://doi.org/10.1016/j.scriptamat.2015.01.013.
13. Camposilvan, E., Anglada, M. Size and Plasticity Effects in Zirconia Micropillars Compression. *Acta Mater*. 2016;103:882–892. https://doi.org/10.1016/j.actamat.2015.10.047.
14. Zeng, X.M., Du, Z., Schuh, C.A., Tamura, N., Gan, C.L. Microstructure, Crystallization and Shape Memory Behavior of Titania and Yttria Co-Doped Zirconia. *J Eur Ceram Soc*. 2016;36(5):1277–1283. https://doi.org/10.1016/j.jeurceramsoc.2015.11.042.
15. Zeng, X.M., Lai, A., Gan, C.L., Schuh, C.A. Crystal Orientation Dependence of the Stress-Induced Martensitic Transformation in Zirconia-Based Shape Memory Ceramics. *Acta Mater*. 2016;116:124–135. https://doi.org/10.1016/j.actamat.2016.06.030.
16. Du, Z., Ye, P., Zeng, X.M., Schuh, C.A., Tamura, N., Zhou, N., Gan, C.L. Synthesis of Monodisperse CeO_2–ZrO_2 Particles Exhibiting Cyclic Superelasticity Over Hundreds of Cycles. *J Am Ceram Soc*. 2017;100(9):4199–4208. https://doi.org/10.1111/jace.14972.
17. Faber, K.T. Small Volumes Create Super(elastic) Effects. *Science*. 2013;341(6153):1464–1465. https://doi.org/10.1126/science.1245097.
18. Zeng, X.M., Du, Z., Tamura, N., Liu, Q., Schuh, C.A., Gan, C.L. *In-Situ* Studies on Martensitic Transformation and High-Temperature Shape Memory in Small Volume Zirconia. *Acta Mater*. 2017;134:257–266. https://doi.org/10.1016/j.actamat.2017.06.006.
19. Rauch, H.A., Chen, Y., An, K., Yu, H.Z. *In-Situ* Investigation of Stress-Induced Martensitic Transformation in Granular Shape Memory Ceramic Packings. *Acta Mater*. 2019;168:362–375. https://doi.org/10.1016/j.actamat.2019.02.028
20. Yu, H.Z., Hassani-Gangaraj, M., Du, Z., Gan, C.L., Schuh, C.A. Granular Shape Memory Ceramic Packings. *Acta Mater*. 2017;132:455–466. https://doi.org/10.1016/j.actamat.2017.04.057.
21. Crystal, I.R., Lai, A., Schuh, C.A. Cyclic Martensitic Transformations and Damage Evolution in Shape Memory Zirconia: Single Crystals vs Polycrystals. *J Am Ceram Soc*. 2020;103(8):4678–4690. https://doi.org/10.1111/jace.17117.
22. Deville, S. Freeze-Casting of Porous Ceramics: A Review of Current Achievements and Issues. *Adv Eng Mater*. 2008;10:155–169. https://doi.org/10.1002/adem.200700270.
23. Nelson, I., Naleway, S.E. Intrinsic and Extrinsic Control of Freeze Casting. *J Mater Res Techn*. 2019;8(2):2372–2385. https://doi.org/10.1016/j.jmrt.2018.11.011.
24. Zeng, X., Arai, N., Faber, K.T. Robust Cellular Shape-Memory Ceramics via Gradient-Controlled Freeze Casting. *Adv Eng Mater*. 2019;21(12):1900398. https://doi.org/10.1002/adem.201900398.

25. Naviroj, M., Voorhees, P.W., Faber, K.T. Suspension- and Solution-Based Freeze Casting for Porous Ceramics. *J Mater Res*. 2017;32(17):3372–3382. https://doi.org/10.1557/jmr.2017.133.
26. Arai, N., Faber, K.T. Hierarchical Porous Ceramics via Two-Stage Freeze Casting of Preceramic Polymers. *Scr Mater*. 2019;162:72–76. https://doi.org/10.1016/j.scriptamat.2018.10.037.
27. Arai, N. Freeze Casting of Ceramics: Pore Design from Solidification Principles. Ph.D.; California Institute of Technology; 2021 https://doi.org/10.7907/3rmr-cz93
28. Zhao, X., Vanderbilt, D. Phonons and Lattice Dielectric Properties of Zirconia. *Phys Rev B*. 2002;65(7):075105. https://doi.org/10.1103/PhysRevB.65.075105.
29. Kontoyannis, C.G., Carountzos, G. Quantitative Determination of the Cubic-to-Monoclinic Phase Transformation in Fully Stabilized Zirconias by Raman Spectroscopy. *J Am Ceram Soc*. 1994;77(8):2191–2194. https://doi.org/10.1111/j.1151-2916.1994.tb07117.x.
30. Kontoyannis, C.G., Orkoula, M. Quantitative Determination of the Cubic, Tetragonal and Monoclinic Phases in Partially Stabilized Zirconias by Raman Spectroscopy. *J Mater Sci*. 1994;29(20):5316–5320. https://doi.org/10.1007/BF01171541.
31. Clarke, D.R., Adar, F. Measurement of the Crystallographically Transformed Zone Produced by Fracture in Ceramics Containing Tetragonal Zirconia. *J Am Ceram Soc*. 1982;65(6):284–288. https://doi.org/10.1111/j.1151-2916.1982.tb10445.x.
32. Katagiri, G., Ishida, H., Ishitani, A., Masaki, T.. Science and Technology of Zirconia. *American Ceramic Society: Westerville, OH, USA*. 1988;537–544.
33. Lim, C.S., Finlayson, T.R., Ninio, F., Griffiths, J.R. *In-Situ* Measurement of the Stress-Induced Phase Transformations in Magnesia-Partially-Stabilized Zirconia Using Raman Spectroscopy. *J Am Ceram Soc*. 1992;75(6):1570–1573. https://doi.org/10.1111/j.1151-2916.1992.tb04227.x.
34. Danks, A.E., Hall, S.R., Schnepp, Z. The Evolution of "Sol–Gel" Chemistry as a Technique for Materials Synthesis. *Mater Horiz*. 2016;3(2):91–112. https://doi.org/10.1039/C5MH00260E.
35. Arai, N., Faber, K.T. Gradient-Controlled Freeze Casting of Preceramic Polymers. *J Eur Ceram Soc*. 2023;43(5):1904–1911. https://doi.org/10.1016/j.jeurceramsoc.2022.12.016.
36. Piermarini, G.J., Block, S. Ultrahigh Pressure Diamond-Anvil Cell and Several Semiconductor Phase Transition Pressures in Relation to the Fixed Point Pressure Scale. *Rev Sci Instrum*. 2008;46(8):973–979. https://doi.org/10.1063/1.1134381.
37. Toraya, H., Yoshimura, M., Somiya, S. Calibration Curve for Quantitative Analysis of the Monoclinic-Tetragonal ZrO2 System by X-Ray Diffraction. *J Am Ceram Soc*. 1984;67(6):C-119-C–121. https://doi.org/10.1111/j.1151-2916.1984.tb19715.x.
38. Zeng, X. Development and Characterization of Shape Memory Ceramics at Micro/Nanoscale. Ph.D. Thesis; 2017 https://doi.org/10.32657/10356/69895.
39. Zhao, X.-S., Shang, S.-L., Liu, Z.-K., Shen. J.-Y. Elastic Properties of Cubic, Tetragonal and Monoclinic ZrO_2 from First-Principles Calculations. *J Nucl Mater.* 2011;415(1):13–17. https://doi.org/10.1016/j.jnucmat.2011.05.016.

40. Watanabe, S. Elastic Analysis of Axi-symmetric Finite Cylinder Constrained Radial Displacement on the Loading End. *Structural Engineering Earthquake Engineering*. 1996;13:175s–186s..
41. Benthem, J.P., Minderhoud, P. The Problem of the Solid Cylinder Compressed Between Rough Rigid Stamps. *Int J Solids Struc.* 1972;8(8):1027–1042. https://doi.org/10.1016/0020-7683(72)90067-4.
42. Savitzky, A., Golay, M.J.E. Smoothing and Differentiation of Data by Simplified Least Squares Procedures. *Anal Chem*. 1964;36(8):1627–1639. https://doi.org/10.1021/ac60214a047.

Chapter 4

TEMPORARILY REDACTED

Chapter 5

POROUS CERAMICS AS ELECTRON ACCEPTORS AND HABITATS FOR GEOBACTERIAL COLONIZATION

This work was performed in collaboration with Y. Jangir, P. Samantaray, A. Johnson, J.A. Kornfield, and V.J. Orphan. P. Samantaray performed FeOOH deposition in SiOC ceramics (Section 5.2.1.2) and provided colloidal iron oxide nanoparticles for incorporation in the freeze casting process (Section 5.2.2.1). Y. Jangir cultured *Geobacter sulfurreducens* for colonization in SiOC ceramics (Section 5.2.1.3), and A. Johnson performed incubation of the culture with the ceramics and took scanning electron microscope images of the colonized samples (Section 5.2.1.3). J.A. Kornfield, V.J. Orphan, and K.T. Faber supervised the experimental work.

5.1. Introduction

One of the most damaging effects of anthropogenic climate change is the increase of greenhouse gases such as methane and nitrous oxide in the atmosphere[1–3]. In addition to trapping heat and contributing to global warming, the proliferation of these and other pollutants greatly impacts natural biogeochemical processes[1,4,5]. Biogeochemical cycles, in which elements such as carbon, nitrogen, and sulfur move between living organisms, the atmosphere, and geological sinks, are not only impacted by the increased amounts of greenhouse gases in the atmosphere, but also may provide potential solutions to mitigate the damaging effects of anthropogenic climate change[4–8].

The microorganisms that play such key roles in naturally occurring biogeochemical cycles have been considered as holding potential solutions to removing or remediating toxic gases and other pollutants from the environment[9,10].

Exoelectrogens are a class of organisms that can pass electrons between themselves and external sources—whether those sources be other exoelectrogenic organisms, electron sources, or electron sinks[10]. Current electromicrobiological research seeks to not only better understand how these organisms function in natural biogeochemical cycles, but also investigate how the ability of these organisms to perform complex chemical transformations could be harnessed to mitigate air- and water-borne pollution[11–17].

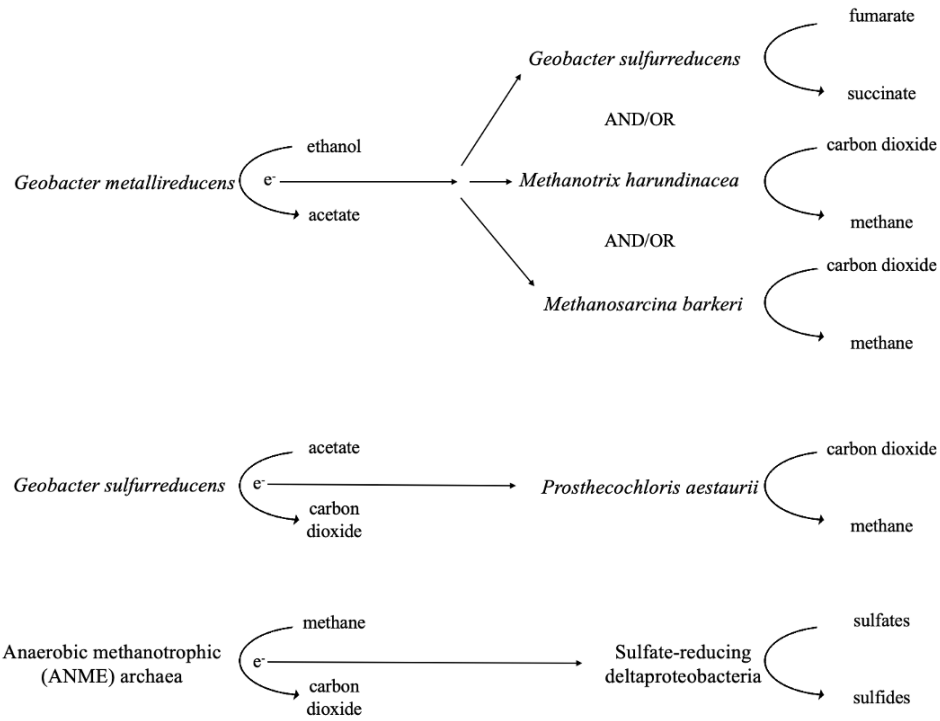

Figure 5.1. A selection of exoelectrogens and redox-active compounds that can participate in direct interspecies electron transfer (DIET) reactions to reduce fumarate, carbon dioxide, and sulfates, among others, and oxidize compounds such as ethanol, acetate, and methane[18–23].

The chemical transformations that exoelectrogens mediate generally fall under two categories: direct electron transfer (DET) and direct interspecies electron transfer (DIET). In direct electron transfer, an exoelectrogenic microorganism will pass

electrons to or from redox-capable minerals or electrodes[24]. In direct interspecies electron transfer, co-consortia of multiple exoelectrogenic species will work in concert to couple redox pathways together, some examples of which are shown in Figure 5.1[18]. The specific cellular mechanism which enables an organism to move electrons across its cellular membrane will differ depending on the redox potential of the electron source or sink, but through these mechanisms, technologies such as microbial fuel cells and microbial electrolysis cells have been developed to utilize these organisms to perform complex chemical transformations[25–29].

One such exoelectrogenic organism is *Geobacter sulfurreducens,* an anaerobic bacterium first isolated from river sediment in the 1990s[30]. *G. sulfurreducens* is one of the most well-studied metal-reducing microorganisms, and is capable of acting as either an electron acceptor or an electron donor[25, 30, 31]. This organism has commonly been shown to donate electrons to iron oxyhydroxide species, and also to conductive materials that can act as electrodes and measure cellular activity through the flow of current from the *Geobacter* culture[10,18,21]. However, as with many other exoelectrogenic organisms, it is difficult to understand how these bacteria interact with their natural microenvironment—studying these microbes generally necessitates their removal from their native habitats, and thus limits the understanding of the spatial and temporal dynamics at play in such environments[32].

In Chapter IV, a transparent soil mimic was produced to begin to probe microbial colonization dynamics in a three-dimensional porous material. In this chapter, electron acceptors such as iron oxide species and carbon nanotubes will be incorporated into opaque porous materials with the goal of creating replicable porous matrices that can provide electron sinks and/or act as electrodes for probing microbial activity in real time. Iron oxide species were added to materials after, during, and as the primary solute material in the freeze casting process, and the advantages and disadvantages of adding iron oxides to porous materials in these ways was explored. Additionally, since previous work had shown that the conductivity of SiOC can be increased by several orders of magnitude by incorporating multi-walled carbon

nanotubes (MWCNT) to the porous matrix, conductive, robust porous ceramics were considered as bacterial habitats that can simultaneously monitor electrical activity[33, 34]. In this chapter that technique was expanded to encompass additional pore regimes better suited for microbial colonization.

5.2. Materials and Methods

5.2.1. Porous SiOC ceramics for bacterial colonization

5.2.1.1. Freeze casting of ceramics

To prepare dendritic SiOC ceramics, 20 wt.% MK powder, a methyl-functionalized polysiloxane preceramic polymer (Wacker Chemie, Munich, Germany) was dissolved in cyclohexane (Thermo Fisher Scientific, Waltham, MA, USA) before 1 wt.% Geniosil GF91 (Wacker Chemie, Munich, Germany) was added as a crosslinker and stirred with the preceramic polymer and solvent for five minutes. The solution was then degassed under vacuum and poured into a borosilicate ring 20 mm high and 24 mm in diameter that was lined with Mylar® sheeting (The Tape Casting Warehouse, Inc., Morrisville, PA, USA) and placed on a freeze casting setup described in previous work[35–37]. The solution was then freeze cast such that the freezing front velocity was controlled to be 15 μm/s[36].

Once freeze-cast, the sample was placed in a lyophilizer (VirTis AdVantage 2.0, SP Scientific, Warminster, PA, USA) for at least 24 hours. The porous green body was then pyrolyzed under Ar for 4 hours at 1100°C in a tube furnace (Carbolite CTF 17/300 Tube Furnace, Haan, Germany). Once pyrolyzed, the samples were cut into quarter circles using a wafer dicing saw.

5.2.1.2. FeOOH deposition

Colloidal FeOOH was synthesized inside porous SiOC ceramics by submerging the ceramics in a solution of 0.4M $FeCl_3$ in distilled water under vacuum until the air inside the pores of the ceramics had been replaced by the iron chloride solution and

the ceramics descended to the bottom of the jar. The samples were then removed and washed with a 25% (w/v) NaOH solution before being submerged in distilled water at neutral pH for 1 hour under vacuum. Samples were then washed with distilled water and IPA. Some samples were polished so that no iron oxide remained on the surface of the ceramic, and others remained unpolished, with iron oxide remaining on the surface.

5.2.1.3. Bacterial growth and incubation

Geobacter sulfurreducens were grown in anerobic conditions in 10mL of a medium containing 20mM sodium acetate and 30mM sodium fumarate, by incubating 1mL *G. sulfurreducens* in the medium for one week. This culture was then injected into an airtight tube containing the FeOOH-functionalized ceramic that had been purged with CO_2/N_2 for 15 minutes. The tubes were placed into a water bath kept at 30°C for 25 days.

After incubation, the ceramics were fixed with 2.5% glutaraldehyde and dehydrated using a stepwise dehydration procedure, first using ethanol, then using hexamethyldisilane (HDMS). Samples were then coated with 20nm Pd/Pt before imaging on a Zeiss 1550 VP scanning electron microscope (Carl Zeiss AG, Oberkochen, Germany).

5.2.2. Porous SiOC with incorporated iron oxide nanoparticles

5.2.2.1. Preparation of colloidal iron oxides

Poorly crystalline Fe_2O_3 (PCIO), which has been previously used as an electron acceptor with exoelectrogenic cellular cultures, was prepared according to a method adapted from Lovley et al. in which 0.4M $FeCl_3 \cdot 6H_2O$ was stirred constantly[38]. A solution of 10M NaOH was then used to adjust the acidity of the solution to pH 7. The suspension was washed, freeze dried, and stored at -80°C.

Colloidal ferrihydrite was prepared using a method adapted from Schwertmann et al.[39] A 0.2M solution of $Fe(NO_3)_3 \cdot 9H_2O$ was stirred continuously while 1M KOH was added dropwise to raise the pH to 7. The suspension was washed via centrifugation and resuspension, then freeze dried and stored at -80°C.

5.2.2.2. Freeze casting of ceramics

The two types of colloidal iron oxide—α-Fe_2O_3 and FeO(OH)—were mixed with polysiloxane powder in concentrations of 0-10 wt.% each. Dendritic SiOC ceramics were then freeze cast, freeze dried, and pyrolyzed in the same manner as described in Section 5.2.1.1. Samples were photographed following freeze drying, before pyrolysis. The SiOC-Fe ceramics were then cut along the freezing direction using a wafer dicing saw, coated with 10nm Pd/Pt, and imaged using scanning electron microscopy and energy dispersive X-ray spectroscopy (Zeiss 1550 VP, Carl Zeiss AG, Oberkochen, Germany).

Colloidal nanoparticles that had not been freeze-cast were subjected to the same conditions as the composite ceramics required for pyrolysis (4 hours at 1100°C in Ar atmosphere), and X-ray diffraction traces were collected with a Panalytical X'Pert Pro Powder X-ray Diffractometer using Cu K-α radiation (Malvern Panalytical, Worcestershire, UK).

5.2.3. Porous iron oxide ceramics

5.2.3.1. Freeze casting of ceramics

Porous iron oxide ceramics were fabricated using a suspension-based freeze-casting process on a freeze-casting setup outlined in previous work (Figure 1.6b) [35–37]. To prepare suspensions for freeze casting, 10 vol% Fe_2O_3 (Sigma Aldrich, St. Louis, MO, USA) was mixed with cyclohexane (Thermo Fisher Scientific, Waltham, MA, USA) that had been sonicated with a dispersant (KD4, Croda Inc., Yorkshire, UK). The suspension was then ball-milled until well mixed and pipetted into a borosilicate

mold of dimensions 12.5 mm high, 24 mm inner diameter, 32 mm outer diameter. The mold was lined with Mylar® sheeting (The Tape Casting Warehouse, Inc., Morrisville, PA, USA) and placed on the thermoelectric plate of the freeze casting setup prior to the addition of suspension. The top cold finger was then placed in the mold such that its face was in contact with the suspension, and the thermoelectric plates were cooled such that the freezing rate corresponded with the freezing front velocity noted in Table 5.1.

Table 5.1. Freeze casting and sintering parameters for iron oxide samples.

Experimental Variable	Sample	Freezing	Sintering			
		Freezing Front Velocity	Time	Temperature	Atmosphere	Flow Rate
Freezing Front Velocity	1 μm/s	1 μm/s	2h/2h	600°C/1100°C	Argon	3SCFH
	3 μm/s	3 μm/s	2h/2h	600°C/1100°C	Argon	3SCFH
	5 μm/s	5 μm/s	2h/2h	600°C/1100°C	Argon	3SCFH
Sintering Temperature	600°C	5 μm/s	4h	600°C	Argon	3SCFH
	800°C	5 μm/s	4h	800°C	Argon	3SCFH
	1000°C	5 μm/s	4h	1000°C	Argon	3SCFH
	1100°C	5 μm/s	4h	1100°C	Argon	3SCFH
Atmosphere Humidity	Dry Air	5 μm/s	4h	1000°C	Air	N/A
	1SCFH	5 μm/s	4h	1000°C	Air + H_2O	1SCFH
	3SCFH	5 μm/s	4h	1000°C	Air + H_2O	3SCFH
	5SCFH	5 μm/s	4h	1000°C	Air + H_2O	5SCFH

After freeze casting, samples were freeze dried in a lyophilizer (VirTis AdVantage 2.0, SP Scientific, Warminster, PA, USA) for at least 24 hours and sintered according to the times, temperatures, and atmospheres outlined in Table 5.1. Sintering runs under inert or humid atmospheres were done in a tube furnace (Carbolite CTF 17/300 Tube Furnace**,** Haan, Germany). Humid atmospheres were created by bubbling industrial air through a DI water-filled beaker kept at 95°C before flowing into the tube furnace at the rates noted in Table 5.1. Sintering runs in dry air were done in a box furnace (CM Rapid Temp 1700°C Furnace, CM Furnaces, Inc., Bloomfield, NJ, USA).

5.2.3.2. Analysis of composition and pore morphology

The open porosity of iron oxide samples was measured through the Archimedes method. The pore size distributions of samples freeze-cast at different freezing rates were collected through mercury intrusion porosimetry (AutoPore IV Mercury Intrusion Porosimeter, Micromeritics, Norcross, GA, USA). Other samples were cut parallel and perpendicular to the freezing direction and coated with 10 nm Pd/Pt for imaging using SEM.

Iron oxide samples sintered at different temperatures were analyzed using X-ray diffraction on a Panalytical X'Pert Pro Powder X-ray Diffractometer using Cu K-α radiation (Malvern Panalytical, Worcestershire, UK). Samples sintered under different atmospheres, as noted in Table 5.1, were analyzed through X-ray diffraction and through Raman spectroscopy (InVia Raman Microscope, Renishaw, Wotton-under-Edge, UK).

5.2.4. Porous SiOC-carbon nanotube composites

5.2.4.1. Freeze casting of ceramics

SiOC-CNT composite structures were created according to procedures developed in previous work, but with alternate freezing solvents[33, 34]. Hypermer KD4 dispersant (Croda Inc., Yorkshire, UK) was first dissolved in cyclohexane (Thermo Fisher Scientific, Waltham, MA, USA) or in cyclooctane (Thermo Fisher Scientific, Waltham, MA, USA). Multi-walled carbon nanotubes (MWCNT) (US Research Nanomaterials, Inc., TX, USA) were then added to the solution at either 1.32 wt.%, 4.26 wt.%, or 8.16 wt.%, and sonicated for 1 hour before MK powder (Wacker Chemie, Munich, Germany) was added to the suspension. This solution was sonicated for another 60 minutes, then 1 wt.% Geniosil GF91 (Wacker Chemie,

Munich, Germany) was added as a crosslinker and stirred with the preceramic polymer, carbon nanotubes, and solvent for three minutes.

These suspensions were then freeze cast and controlled such that the freezing front velocity was 15μm/s, freeze dried in a lyophilizer (VirTis AdVantage 2.0, SP Scientific, Warminster, PA, USA) for at least 24 hours and pyrolyzed at 1100°C in Ar for 4 hours in a tube furnace (Carbolite CTF 17/300 Tube Furnace**,** Haan, Germany)[36].

5.2.4.2. Agglomeration and conductivity analysis

CNT agglomeration was assessed through scanning electron microscopy of samples cut along the freezing direction on a Zeiss 1550 VP Scanning Electron Microscope (Carl Zeiss AG, Oberkochen, Germany). Due to the increased conductivity of these samples as a result of CNT incorporation, additional coating of the samples was not necessary.

To measure sample conductivity, the parallel faces of the porous SiOC-CNT composites were coated with a conductive silver paste (Thermo Fisher Scientific, Waltham, MA, USA). The resistance of these samples was then measured using a multimeter, and the conductivity calculated from these values.

5.3. Results and Discussion

5.3.1. Iron oxides incorporated after freeze casting

In seeking porous materials that can act as both habitats for microorganisms and provide a source of electron acceptors, dendritic SiOC ceramics were fabricated and FeOOH deposited inside the porous ceramics. SiOC was chosen for this proof-of-concept test as a well-studied, robust material into which pores can easily be incorporated through freeze casting of preceramic polymers such as polysiloxane. A robust ceramic was necessary, as many microorganisms that can perform chemical transformations naturally inhabit sediments in high-pressure environments—such as

those found on the seafloor or near hydrothermal vents. As a preliminary method of iron incorporation, FeOOH nanoparticles were synthesized directly in the pores of the dendritic ceramic before the ceramic was exposed to a bacterial culture for incubation over several weeks. After this incubation, scanning electron microscopy (SEM) images showed that in both samples with and without iron oxide nanoparticles on their surfaces, bacteria were present on the ceramic surface (Figure 5.2.) In Figure 5.2a, the bacteria were seen amongst the electron-accepting FeOOH nanoparticles, but even on a surface that FeOOH had been removed from (Figure 5.2b), bacteria appeared to have colonized the SiOC ceramic.

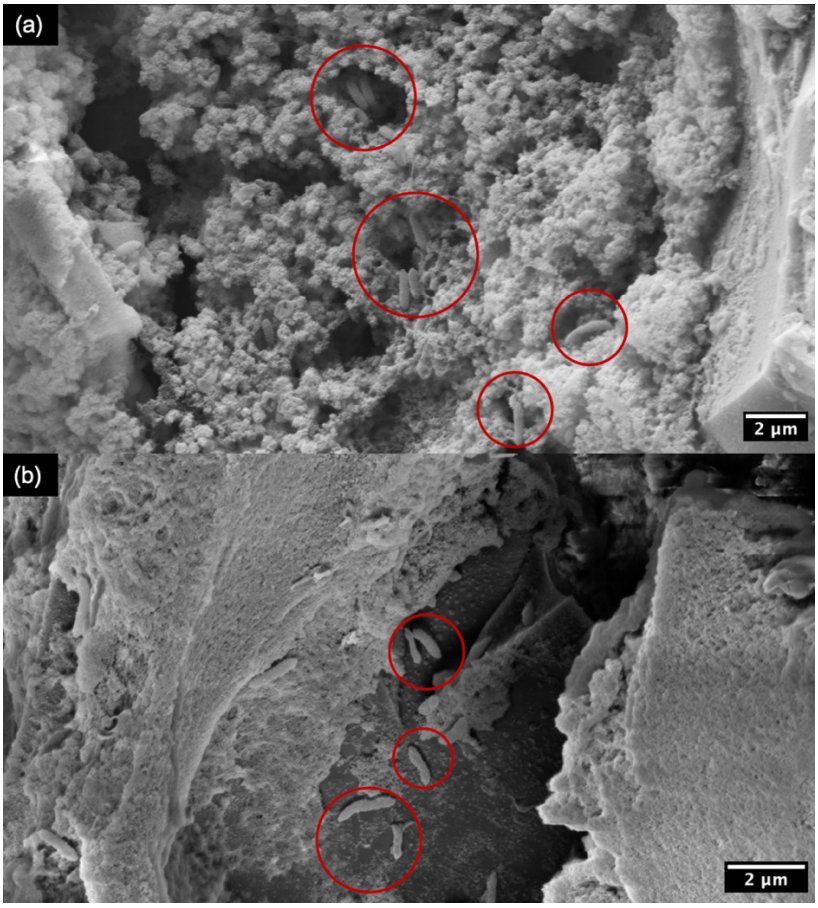

Figure 5.2. Surfaces of dendritic SiOC ceramics with deposited iron oxide nanoparticles that have been exposed to a culture of G. sulfurreducens. The iron nanoparticles on the surface (a) have not and (b) have been removed. Bacterial cells are circled in red. Nanoparticles appear as spherical deposits on the smooth SiOC surface.

The presence of bacteria on the surface of each of these samples primarily indicated that SiOC was non-toxic to the bacteria, and indeed, even surfaces without electron acceptors like FeOOH could be colonized by the *Geobacter sulfurreducens* culture. This implied that these porous materials were useful in and of themselves for colonization of species like *Geobacter sulfurreducens.* However, these images did not reveal the depth of colonization within the ceramic, only that bacteria had adhered to the surface of the ceramics. Additionally, it was unclear how well-dispersed the colloidal FeOOH nanoparticles were within the pore space of the ceramic. While the nanoparticles remained visible in Figure 5.2a, after washing, incubation with bacteria, and fixation, it was less clear how homogeneously distributed the electron acceptors were throughout the depth of the porous matrix. Subsequently, investigation turned to creating a robust, porous ceramic structure with iron oxyhydroxide species homogeneously dispersed throughout the pore matrix.

5.3.2. Iron oxide nanoparticles incorporated during freeze casting

To fabricate a robust porous ceramic with iron oxides incorporated throughout the sample, colloidal iron nanoparticles were mixed with the preceramic polymer to create a freeze casting solution so as to yield a dendritic pore morphology. The colloidal iron nanoparticles used were already known to be non-toxic to bacteria, and to act as electron acceptors for exoelectrogens such as *Geobacter sulfurreducens.* However, difficulties occurred as soon as the freeze casting process had begun—photos of freeze-cast and -dried polysiloxane-iron nanoparticle ceramics show a distinct difference in appearance between the top and bottom of the freeze-cast sample (Figure 5.3). At the top of each sample, the samples made with various ratios of nanoparticles to preceramic polymer all appeared similar to one another and to the control sample freeze cast without nanoparticles. At the bottom of the sample, however, where the solvent crystals nucleate during freezing, the appearance of the sample changed dramatically. In each sample, regardless of the type or concentration

of iron oxide nanoparticles mixed with the polysiloxane, those nanoparticles were now visible. In samples with relatively low concentrations of nanoparticles (2.5 wt.%), the nanoparticles were distributed across the bottom of the polysiloxane structure. However, in samples with 5-10 wt.% nanoparticles, the nanoparticles had formed a dark (α-Fe_2O_3) or light (FeO(OH)) film that almost entirely obscures the white polysiloxane structure.

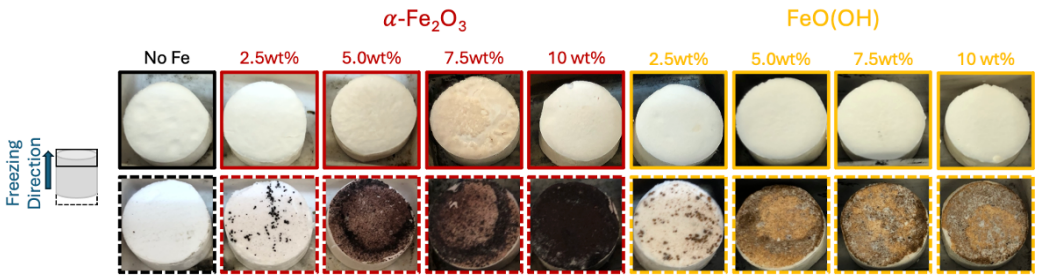

Figure 5.3. The top face (upper row) and bottom face (lower row) of freeze-cast and -dried dendritic polysiloxane green bodies, with iron oxide nanoparticles incorporated into the preceramic polymer powder.

These images implied that a most of the nanoparticles had settled to the bottom of the mold during the thirty-minute freeze-casting process. As the procedure to create dendritic polysiloxane structures is one of the fastest freeze-casting procedures (columnar structures such as those seen in Chapters III and IV can take over two hours to freeze cast), this indicated that the colloidal nanoparticles used here had fallen to the bottom of the freeze-casting mold too quickly to be trapped within the solid preceramic polymer network that forms as the solvent crystals separate from the polymer during freezing. That settling of the colloidal nanoparticles had occurred was further confirmed by SEM and energy dispersive X-ray spectroscopy (EDX), as seen in Figure 5.4. An agglomeration of iron nanoparticles was clearly visible both in the SEM image (Figure 5.4a) and in the Fe Kα map (Figure 5.4b). The incorporation of nanoparticles into the freeze casting process did not appear to have greatly impacted the dendritic pore morphology of the SiOC ceramic—dendritic

pores were clearly visible in this longitudinal cross-section of the sample. However, while some smaller iron oxide nanoparticles were visible at other locations in the dendritic pore matrix, the main location of iron nanoparticles was at the bottom edge of the sample, further confirming that the majority of nanoparticles agglomerated and settled to the bottom of the freeze casting solution before they could be trapped in place by the solidifying preceramic polymer.

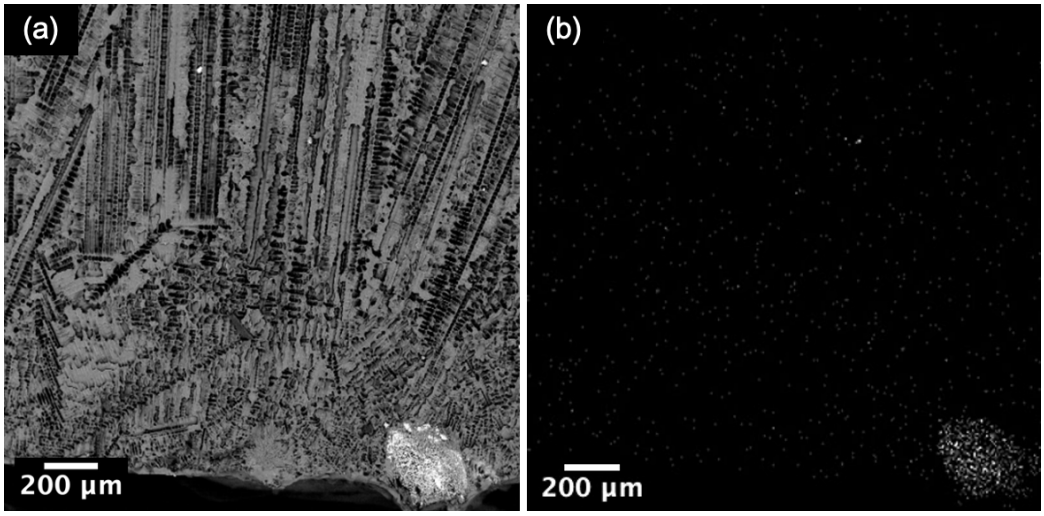

Figure 5.4. Freeze-cast SiOC with iron oxide nanoparticles incorporated during freeze casting. (a) SEM image of an iron nanoparticle agglomerate at the bottom of the dendritic pore network of an SiOC sample, and (b) an EDS map of the iron present in that same region.

X-ray diffraction analysis of α-Fe_2O_3 and FeO(OH) nanoparticles before and after their exposure to pyrolysis conditions revealed further complications with simply combining a well-studied ceramic matrix with a well-studied electron acceptor. Both species of nanoparticle showed significant changes in their XRD trace after being heat-treated at 1100°C in Ar for 4 hours—the conditions required for complete pyrolysis of polysiloxane into SiOC (Figure 5.5). As a result, it was less clear if iron species embedded in polysiloxane during freeze casting and pyrolyzed along with the preceramic polymer would be well-suited to act as electron acceptors for

exoelectrogenic organisms. While the amorphous background of the nanoparticles decreased after sintering in both cases, it was likely that the samples transformed to iron oxide species with a mixture of Fe_3O_4 and Fe_2O_3.

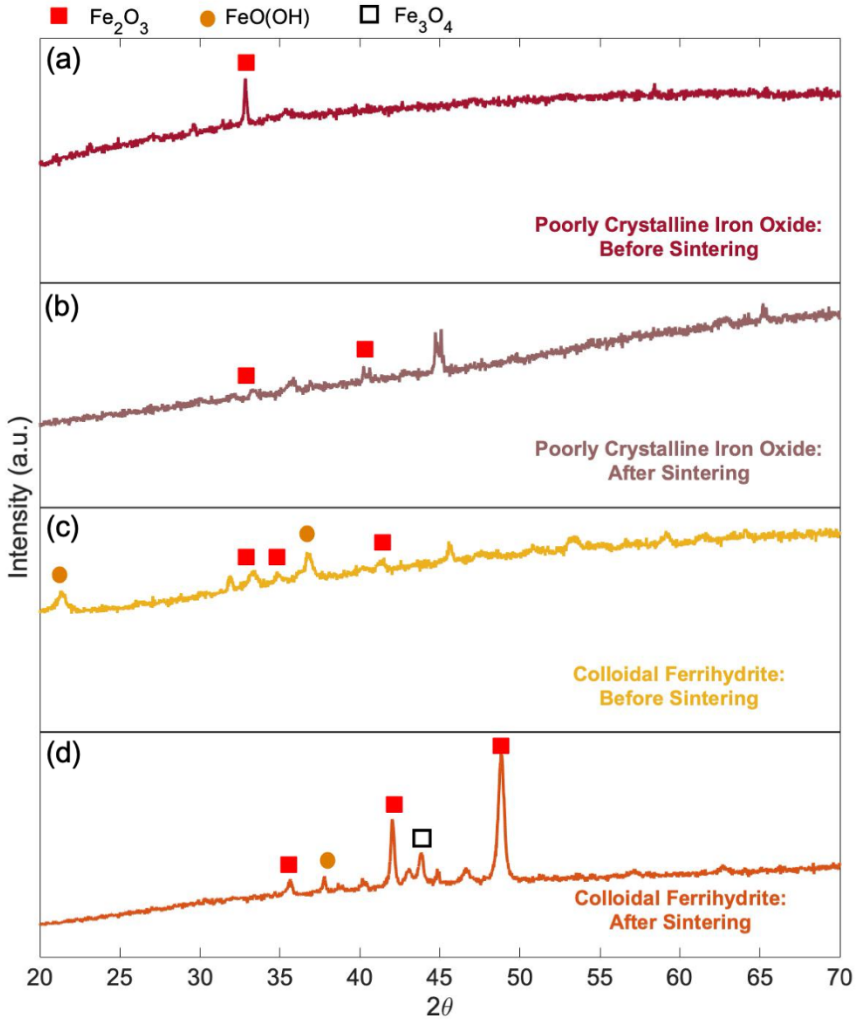

Figure 5.5. X-ray diffraction traces of (a) Fe_2O_3 nanoparticles before exposure to SiOC pyrolysis conditions, (b) Fe_2O_3 nanoparticles after exposure to SiOC pyrolysis conditions, (c) FeO(OH) nanoparticles before exposure to SiOC pyrolysis conditions, and (d) FeO(OH) nanoparticles after exposure to SiOC pyrolysis conditions.

As these nanoparticles were sintered and analyzed on their own, without being incorporated into the SiOC matrix, it is further likely that pyrolysis of a SiOC-Fe

nanoparticle composite might introduce more unwanted side reactions. The iron oxyhydroxide sources used in concert with bacterial species are generally well-controlled, well-defined homogeneous iron oxide nanoparticles[24, 40]. An iron oxide species within a SiOC matrix may be likely to react with carbon from the graphene nanodomains or from the fugitive crosslinker species or may be reduced in the inert atmosphere. As a result of this chemical complexity, and of the heterogeneous distribution of iron oxide nanoparticles within a freeze-cast sample, different materials for creating a porous matrix containing iron oxyhydroxides were explored.

5.3.3. Freeze casting using iron oxide as the primary solute

5.3.3.1. Effects of freezing front velocity on pore morphology

While SiOC produces robust porous ceramics with well-defined porous matrices through solution-based freeze casting, the incorporation of iron oxide nanoparticles into the SiOC matrix proved challenging. Subsequently, suspension-based freeze casting was explored as an alternate route to fabricate porous materials that could act as electron acceptors. While the pore networks produced through suspension-based freeze casting are generally less neatly defined than those produced through solution-based freeze casting, suspension-based freeze casting can be achieved with any material that can be suspended in a solvent, rather than solely those materials that will dissolve in the solvents needed to produce a particular pore structure[41]. To create a porous structure through this technique that could act as an electron acceptor for exoelectrogenic organisms, Fe_2O_3 was chosen as the solute material to be used in suspension-based freeze casting.

By simply altering the freezing rate of the Fe_2O_3-cyclohexane solution, it was possible to change both the open porosity and the pore size of the resulting porous iron-based ceramics (Figure 5.6). In Figure 5.6a, increasing the freezing rate such that the velocity of the cyclohexane freezing front increased resulted in a decrease in the Archimedes open porosity of the sintered, iron-based ceramics, although porosity

of the samples frozen at a rate of 3 μm/s varied widely. This not only indicated that freeze casting with iron oxide was possible, but that control over pore morphologies was able to be exerted. This was further confirmed through mercury intrusion porosimetry (Figure 5.6b). As the freezing front velocity was increased from 1 μm/s to 5 μm/s, the diameter of the pores decreased from 25 μm to 10 μm. That open porosity and pore size can be thus controlled by freezing front velocity was in line with the trends seen in other freeze-cast systems[36, 42], and suggest that levers such as changing the concentration of iron oxide or the solvent could also be utilized to tailor pore morphology of the final iron oxide-based ceramics.

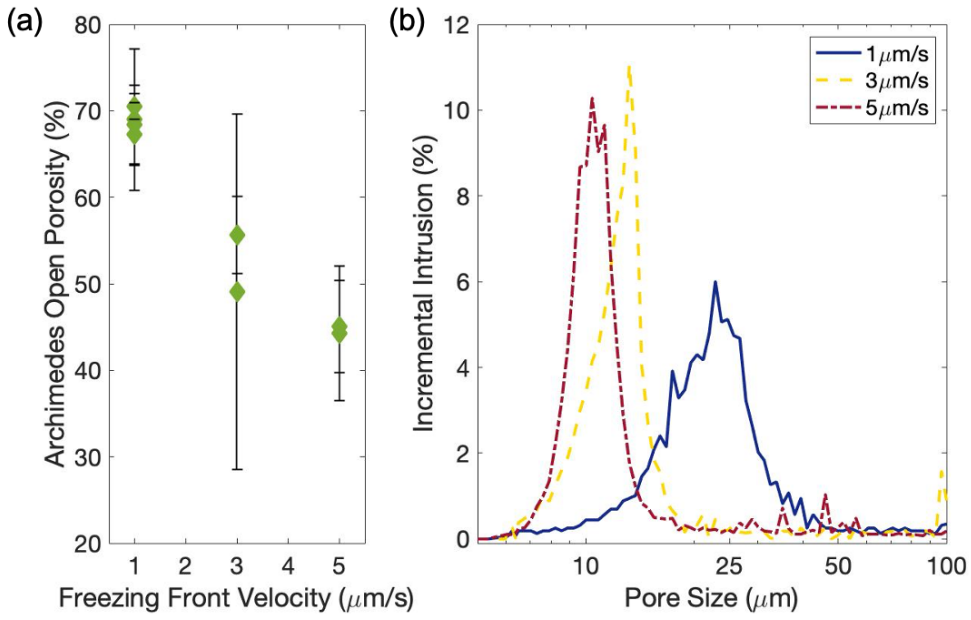

Figure 5.6. Freeze-cast structures with iron oxide as the primary solute. (a) Archimedes open porosity of iron oxide samples freeze cast at different freezing rates. (b) Pore size distributions of iron oxide samples freeze cast at 1 μm/s (-·-), 3 μm/s (-), and 5 μm/s (- -).

The pore morphologies exhibited by the three samples seen in Figure 5.6b trended towards a more unimodal pore size distribution than the bimodal pore size

distribution indicative of dendritic ceramics and discussed in more detail in Sections 4.3.1.2 and 4.3.2.1. This was a result of the slower freezing rate—dendritic pore morphologies result from faster freezing rates than do columnar pore morphologies, and decreasing the freezing rate shifted the morphology of the solvent crystals closer to columnar[36]. While none of the pore size distributions seen in Figure 5.6b were as smooth as would be expected from that of a columnar sample fabricated through solution-based freeze casting, these pore size distributions are in line with other suspension-based freeze cast samples.

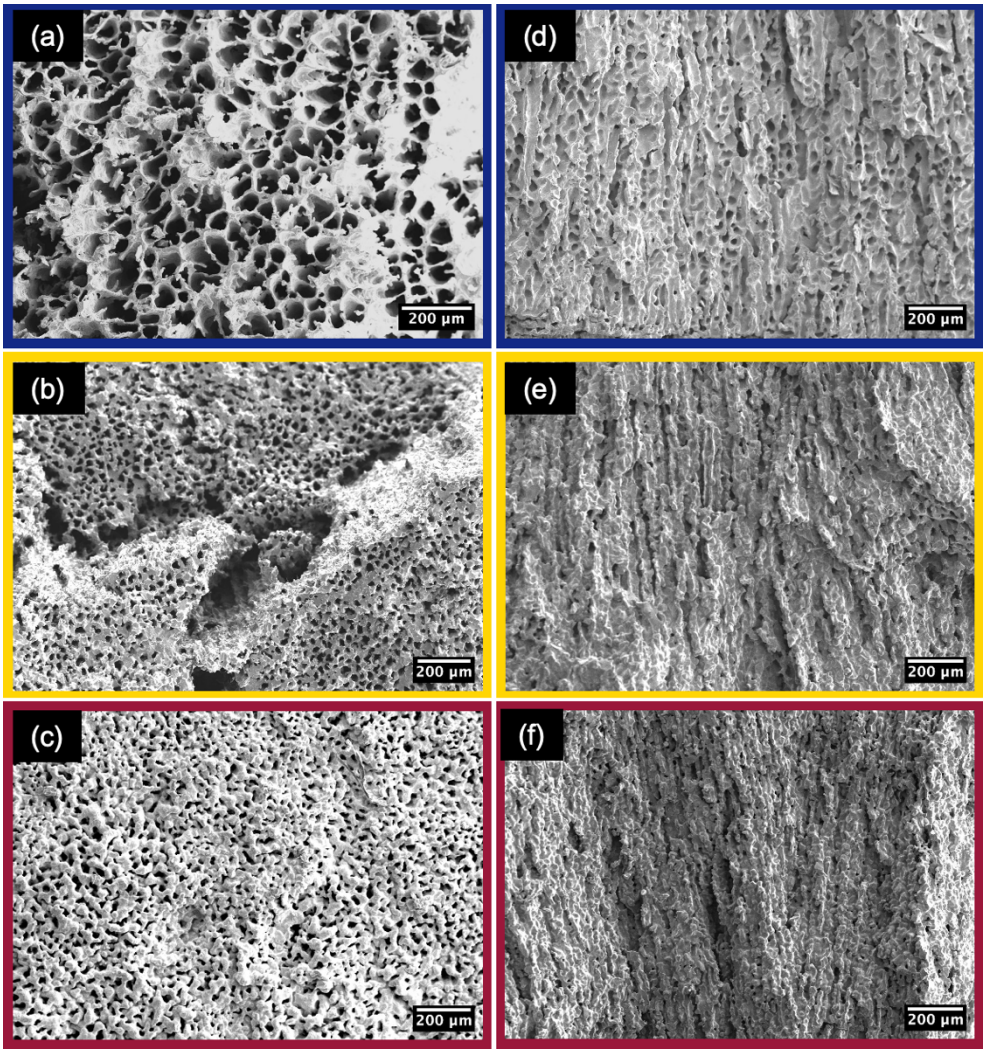

Figure 5.7. SEM images of transverse (a,b,c) and longitudinal (d,e,f) cross-sections of Fe_2O_3 freeze cast at 1 µm/s (a,d), 3 µm/s (b,e), and 5 µm/s (c,f).

These observations were further confirmed through SEM images of the transverse and longitudinal cross-sections of samples freeze cast at each freezing rate (Figure 5.7). Samples frozen at 1 μm/s, the slowest rate studied here, exhibited the largest pores, as seen in the transverse cross-section in Figure 5.7a. Of the three morphologies, the pore walls of samples frozen at 1 μm/s were the smoothest (Figure 5.7d)—however, they were not perfectly columnar. As the freezing front velocity was increased, the resulting pores were smaller (Figure 5.7b and 5.7c), and the pore walls became less smooth (Figures 5.7e and 5.7f). As the freezing front velocity increased, the morphology became more dendritic, resulting in less smooth, columnar pore walls than were seen in samples frozen at a slower rate.

5.3.3.2. Effects of sintering temperature on pore morphology

With a greater understanding of the effects of freezing front velocity on the possible pore morphologies available in suspension-based freeze-cast iron oxide systems, the effect of temperature on the chemical composition was then explored. In order to produce robust ceramics that can survive machining, analysis, and exposure to higher pressures as potential electron-accepting habitats for exoelectrogens, freeze-cast iron oxide must be sintered in order to densify and strengthen the ceramic. However, while the starting material used in the freeze-casting suspension, Fe_2O_3, has been studied as a potential electron acceptor for bacteria[38], the studies of iron oxide nanoparticles in Section 5.3.2. indicated that exposure to high temperatures and/or inert sintering environments might alter the chemical composition of iron oxide species away from the most biologically useful forms.

To probe the effect of temperature on freeze-cast iron oxide, freeze-cast samples were subjected to temperatures ranging from 600°C to 1100°C under an Ar atmosphere. The XRD traces in Figure 5.8a revealed that in all of the samples, Fe_3O_4 peaks were present, indicating that each of the samples has been reduced slightly. However, Fe_2O_3 peaks remained present in all samples except that exposed to 1100°C, and those traces also have faint peaks around $2\theta = 23°$ that may be attributable to some

FeOOH character. The pore size distributions of each of these sintering temperature trials, shown in Figure 5.8b, revealed that while the pore size decreased slightly with increased temperature, the change is not dramatic. This slight decrease in pore size was expected, as some shrinkage of the ceramic accompanies the densification that takes place during sintering. Higher sintering temperatures resulted in increased shrinkage, but also increased the robustness of the iron oxide samples. As 1000°C was the highest sintering temperature that still resulted in samples with some Fe_2O_3 character, it was chosen as the sintering temperature for future tests.

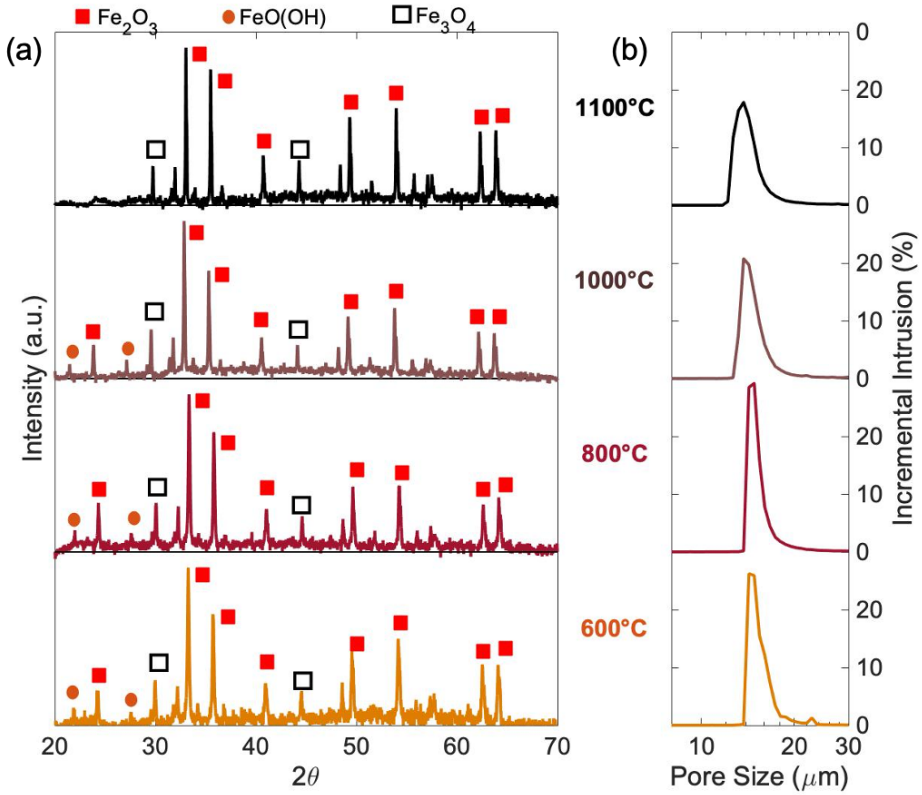

Figure 5.8 Effects of sintering temperature on freeze-cast iron oxide. (a) XRD traces and (b) pore size distributions of iron oxide samples exposed to 600°C (—), 800°C (—), 1000°C (—), and 1100°C (—) in Ar.

5.3.3.3. Effects of sintering atmosphere on pore morphology

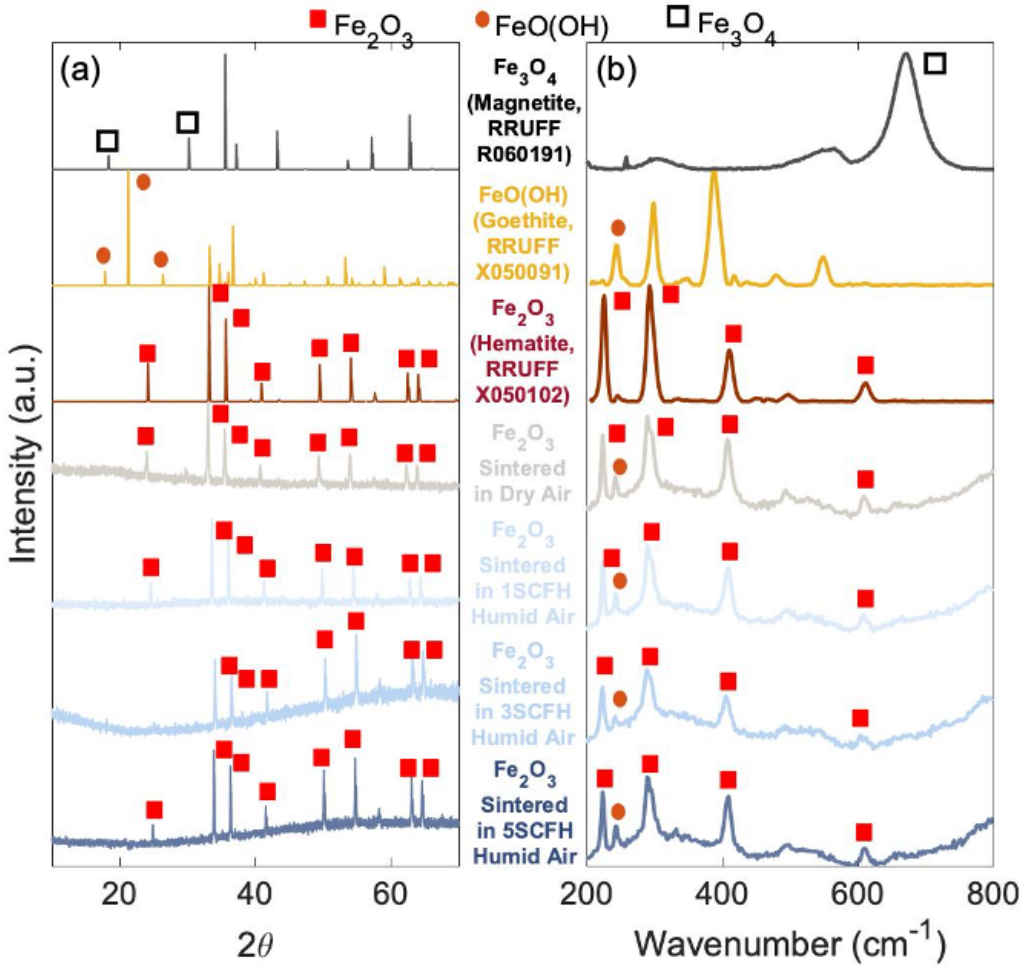

Figure 5.9. Effects of sintering atmosphere on freeze-cast iron oxide. (a) XRD traces and (b) Raman spectra of Fe_2O_3 samples sintered under dry air and increasing flow rates of humid hair, with the Raman spectra and XRD traces of magnetite, goethite, and hematite (taken from the RRUFF Project Database) included as a comparison[43].

While sintering at temperatures between 600°C and 1000°C produced iron oxide samples with some Fe_2O_3 content, these samples were all sintered in inert environments. To probe the effect that humid sintering atmospheres could have on Fe_2O_3 and FeOOH contents, samples were sintered at 1000°C in increasingly humid

atmospheres. The Raman spectra and XRD traces shown in Figure 5.9 revealed that sintering iron oxide in air rather than argon produced samples with little Fe_3O_4 content. Additionally, each of the air sintering environments produced samples with some degree of FeOOH character present in the Raman spectra. Increasing the flow rate of air through the boiling water—thus increasing the humidity—led to an increase in the FeOOH peak in the Raman spectra of the sintered samples, but the increase was fairly small. To fabricate porous Fe_2O_3 samples, sintering the green bodies at 1000°C in air was found to strike a balance between producing samples with the desired chemical composition and samples that could withstand high pressures or mechanical stresses.

5.3.4. SiOC-CNT composites

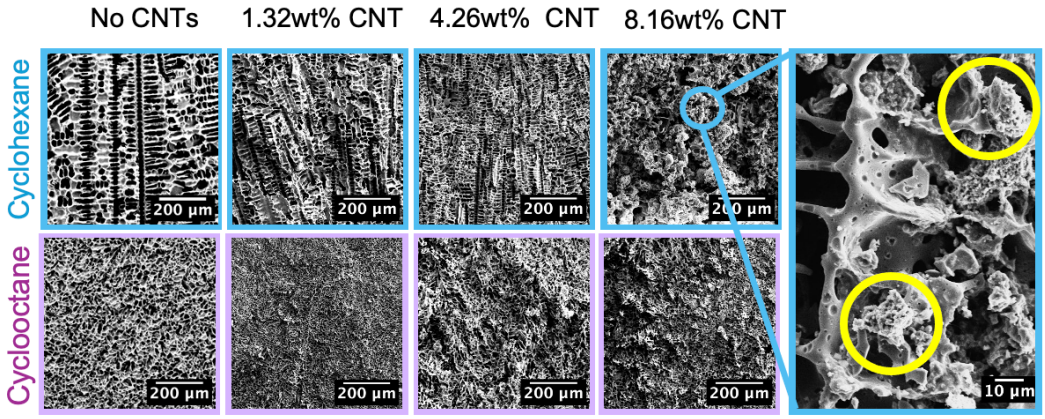

Figure 5.10. SEM images of SiOC ceramics frozen with cyclohexane for dendritic pores (blue) and cyclooctane for isotropic pores (purple) and with increasing amounts of MWCNTs incorporated into the SiOC matrix. On the far right, under higher magnification, the MWCNT agglomerates (circled in yellow) are clearly visible within the dendritic pore structure.

While iron oxyhydroxide species have been frequently studied as an electron acceptor for exoelectrogens like *Geobacter sulfurreducens*, it is also possible to use conductive materials to study their electrochemical activities in real time[11, 12, 16].

However, while SiOC is an easily freeze-cast material, it is very insulating. Previous work by Kuo et al. reports the increased conductivity of porous SiOC by incorporating multi-walled carbon nanotubes (MWCNTs) into the pore walls[33]. As this work focused on lamellar pore morphologies, though, this technique was tested with alternate pore morphologies better suited to bacterial colonization—dendritic and isotropic pores.

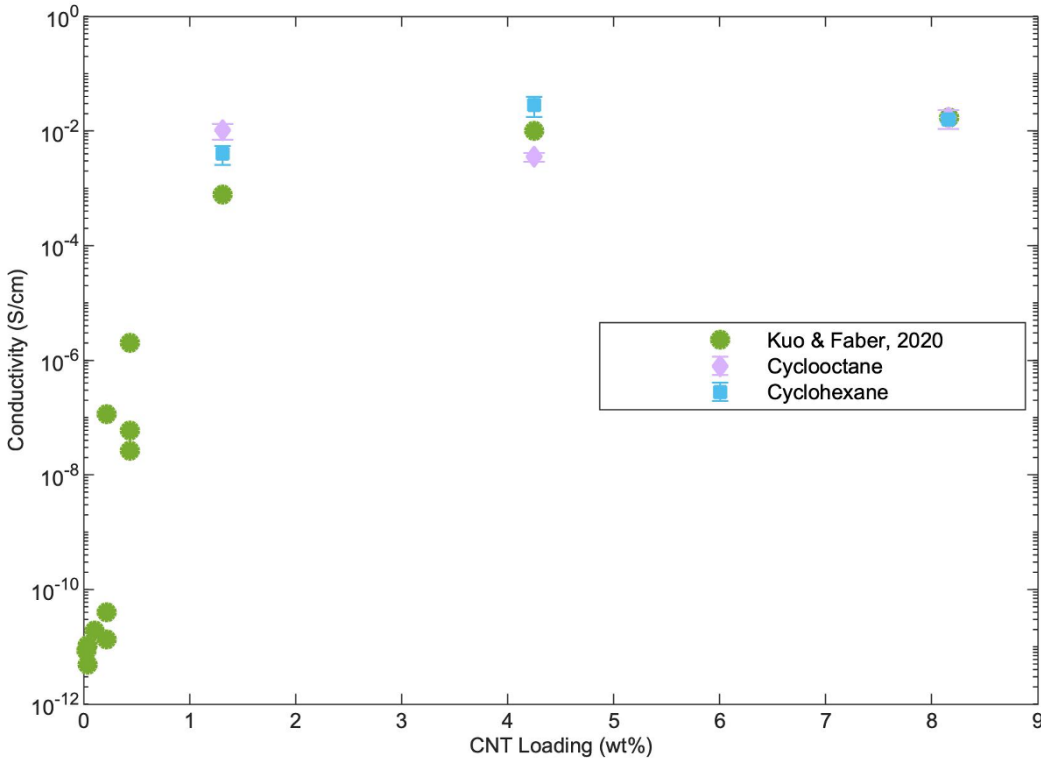

Figure 5.11. Conductivity of dendritic (■), isotropic (◆), and lamellar (●) SiOC ceramics with respect to MWCNT loading (wt.%).

When the technique of CNT incorporation presented in previous work was applied to dendritic and isotropic pore morphologies, the longitudinal cross-sectional SEM images shown in Figure 5.10 revealed that this technique both preserves the desired pore morphology and incorporates MWCNTs into the SiOC structure. As the concentration of CNTs in the freeze casting solution was increased, the aggregated

MWCNTs were increasingly more visible under SEM for both pore morphologies. However, in both morphologies, the characteristic features, such as primary and secondary dendrite arms, remained visible even as the CNT loading was increased. In the high-magnification image on the far right, both the agglomeration of CNTs and the preservation of SiOC pore morphology was visible. The CNT agglomerates were around 10 μm across but were well-distributed across the sample.

While the individual nanotubes were not well-dispersed, however, this agglomeration effect was both in keeping with the trends seen in previous work and not a barrier to increasing the conductivity of the overall sample. Unaltered SiOC was found by Kuo et al. to have a conductivity of less than 10^{-11} S/cm, which is for all intents and purposes insulating. However, samples at each CNT concentration and across both pore morphologies studied exhibited conductivities on the order of 10^{-2} S/cm, an increase of about 9 orders of magnitude (Figure 5.11). This result not only matched well with the measured conductivities of lamellar SiOC-MWCNT composites, but also indicated that even the incorporation of 1 wt.% MWCNTs can dramatically increase the conductivity of both dendritic and isotropic SiOC. As SiOC is robust enough to withstand the high pressures mimicking ocean-floor environments, this increase in conductivity could allow for real-time electrochemical monitoring of cellular activity of exoelectrogens under high pressures.

5.4. Summary

In seeking to further the understanding of the microbial dynamics of exoelectrogens, creating porous materials that can act as habitats for electron-passing organisms will enable further study of how these organisms interact with extracellular substrates and with each other. These porous materials should ideally be robust, and this work has sought to develop such materials that can additionally act as both a microbial habitat and as electron acceptors for direct electron transfer mechanisms between these materials and the exoelectrogenic organisms. Porous ceramics can not only serve these purposes, but also withstand temperature and pressure variations reminiscent

of the natural habitats of many of these unique organisms, and as such, this work builds on previous studies of suspension- and solution-based freeze casting to develop several possible microbial habitats.

Introducing an electron-accepting colloidal iron oxide nanoparticle as a coating on a robust, well-studied porous SiOC ceramic was found to be non-toxic to *Geobacter sulfurreducens*, and well-placed to be used in future studies. Dendritic SiOC ceramics were chosen to allow for colonization of secondary dendritic arms by microbes while primary dendrites were left free for media flow and nutrient circulation throughout the culture. That *G. sulfurreducens* colonized the surface of FeOOH-coated SiOC indicates its biocompatibility, and future studies could explore colonization patterns throughout the ceramic pore network.

Iron oxide species were additionally studied as electron acceptors contained within porous matrices rather than simply as coatings, by adding iron oxides as both secondary and primary solutes during freeze casting. Colloidal iron oxide nanoparticles, while commonly studied and utilized for *ex-situ* culturing of microbial communities as a nutrient included in growth media, were not well-suited for combination with solution-based freeze casting techniques. The majority of the iron present after freeze casting and pyrolysis had settled to the bottom of the samples and was not well-distributed or dispersed throughout the sample. Further optimization of the solutions, dispersants, and particle size may overcome these obstacles, but suspension-based freeze casting provided an alternate approach to incorporating iron species into a porous matrix.

Through suspension- rather than solution-based freeze casting, Fe_2O_3 was instead able to be incorporated as the primary solute in the suspension, resulting in porous solids entirely composed of iron oxide. By adjusting the freezing front velocity during freeze casting, it was possible to alter the pore size and open porosity of the final sintered samples, and by changing the sintering temperature and atmosphere, the specific chemical composition of the porous materials could be more finely tuned.

Through this technique, a variety of chemical compositions and pore morphologies is possible, creating a range of porous materials that could act as both microbial habitats and electron acceptors.

Finally, this work turned to multi-walled carbon nanotubes as an alternate electron acceptor to create conductive, robust SiOC-based porous ceramics. This study expanded on previous work by using other solvents to make available additional pore regimes more suited to microbial colonization than the lamellar structures featured in previous studies. Despite continued agglomeration of the MWCNTs, conductivity of the ceramics increased by several orders of magnitude to a value in keeping with those seen in the literature. Through this and the other approaches, multiple avenues have been explored for creating porous structures intended for microbial habitation and interaction. These investigations will enable the study of microbial electron transfer with solid substrates more similar to those encountered in natural minerals, rather than simply electron transfer to dissolved species, and through conductive porous materials, enable continuous electrochemical monitoring of microbial activity at high pressures reminiscent of the natural habitats of some of the exoelectrogens under study.

5.5. References

1. Reeburgh WS. Oceanic Methane Biogeochemistry. *Chem Rev*. 2007;107(2):486–513. https://doi.org/10.1021/cr050362v.
2. Worden, J.R., Bloom, A.A., Pandey, S., Jiang, Z., Worden, H.M., Walker, T.W., Houweling, S., Röckmann, T. Reduced Biomass Burning Emissions Reconcile Conflicting Estimates of the Post-2006 Atmospheric Methane Budget. *Nat Commun*. 2017;8(1):2227. https://doi.org/10.1038/s41467-017-02246-0.
3. AR5 Climate Change 2013: The Physical Science Basis — IPCC. 2013.
4. Oppo, D., De Siena, L., Kemp, D.B. A Record of Seafloor Methane Seepage Across the Last 150 Million Years. *Sci Rep*. 2020;10(1):2562. https://doi.org/10.1038/s41598-020-59431-3.
5. Boetius, A., Ravenschlag, K., Schubert, C.J., Rickert, D., Widdel, F., Gieseke, A., Amann, R., Jørgensen B.B., Witte, U., Pfannkuche, O. A Marine Microbial Consortium Apparently Mediating Anaerobic Oxidation of Methane. *Nature*. 2000;407(6804):623–626. https://doi.org/10.1038/35036572.
6. Fisher, M.R. Environmental Biology: 3.2 Biogeochemical Cycles. Open Oregon Educational Resources; 2017.

7. He, X., Chadwick, G.L., Kempes, C.P., Orphan, V.J., Meile, C. Controls on Interspecies Electron Transport and Size Limitation of Anaerobically Methane-Oxidizing Microbial Consortia. *mBio*. 2021;12(3):e03620-20. https://doi.org/10.1128/mBio.03620-20.
8. Marlow, J.J., Hoer, D., Jungbluth, S.P., Reynard, L.M., Gartman, A., Chavez, M.S., El-Naggar, M.Y., Tuross, N., Orphan, V.J., Girguis, P.R. Carbonate-hosted Microbial Communities are Prolific and Pervasive Methane Oxidizers at Geologically Diverse Marine Methane Seep Sites. *PNAS*. 2021;118(25):e2006857118. https://doi.org/10.1073/pnas.2006857118.
9. McGlynn, S.E., Chadwick, G.L., O'Neill, A., Mackey, M., Thor, A., Deerinck, T.J., Ellisman, M.H., Orphan, V.J. Subgroup Characteristics of Marine Methane-Oxidizing ANME-2 Archaea and Their Syntrophic Partners as Revealed by Integrated Multimodal Analytical Microscopy. *Appl Envir Microbiol*. 2018. https://doi.org/10.1128/AEM.00399-18.
10. Shi, M., Jiang, Y., Shi, L. Electromicrobiology and Biotechnological Applications of the Exoelectrogens *Geobacter* and *Shewanella* spp. *Sci China Technol Sci*. 2019;62(10):1670–1678. https://doi.org/10.1007/s11431-019-9509-8.
11. Bond, D.R., Holmes, D.E., Tender, L.M., Lovley, D.R. Electrode-Reducing Microorganisms That Harvest Energy from Marine Sediments. *Science*. 2002;295(5554):483–485. https://doi.org/10.1126/science.1066771.
12. Zhang, T., Gannon, S.M., Nevin, K.P., Franks, A.E., Lovley, D.R. Stimulating the Anaerobic Degradation of Aromatic Hydrocarbons in Contaminated Sediments by Providing an Electrode as the Electron Acceptor. *Environ Microbiol*. 2010;12(4):1011–1020. https://doi.org/10.1111/j.1462-2920.2009.02145.x.
13. Adelaja, O., Keshavarz, T., Kyazze, G. Treatment of Phenanthrene and Benzene using Microbial Fuel cells Operated Continuously for Possible *In situ* and *Ex situ* Applications. *Int Biodeter Biodegradation*. 2017;116:91–103. https://doi.org/10.1016/j.ibiod.2016.10.021.
14. Domínguez-Garay, A., Quejigo, J.R., Dörfler, U., Schroll, R., Esteve-Núñez, A. Bioelectroventing: An Electrochemical-assisted Bioremediation Strategy for Cleaning-up Atrazine-Polluted Soils. *Microbial Biotechnol*. 2018;11(1):50–62. https://doi.org/10.1111/1751-7915.12687.
15. Daghio, M., Aulenta, F., Vaiopoulou, E., Franzetti, A., Arends, J.B.A., Sherry, A., Suárez-Suárez, A., Head, I.M., Bestetti, G., Rabaey, K. Electrobioremediation of Oil Spills. *Water Research*. 2017;114:351–370. https://doi.org/10.1016/j.watres.2017.02.030.
16. Gregory, K.B., Lovley, D.R. Remediation and Recovery of Uranium from Contaminated Subsurface Environments with Electrodes. *Environ Sci Technol*. 2005;39(22):8943–8947. https://doi.org/10.1021/es050457e.
17. Pous, N., Balaguer, M.D., Colprim, J., Puig, S. Opportunities for Groundwater Microbial Electro-remediation. *Microbial Biotechnol*. 2018;11(1):119–135. https://doi.org/10.1111/1751-7915.12866.
18. Summers, Z.M., Fogarty, H.E., Leang, C., Franks, A.E., Malvankar, N.S., Lovley, D.R. Direct Exchange of Electrons Within Aggregates of an Evolved Syntrophic Coculture of Anaerobic Bacteria. *Science*. 2010;330(6009):1413–1415. https://doi.org/10.1126/science.1196526.

19. Rotaru, A.-E., Shrestha, P.M., Liu, F., Markovaite, B., Chen, S., Nevin, K.P., Lovley, D.R. Direct Interspecies Electron Transfer between *Geobacter metallireducens* and *Methanosarcina barkeri*. *Applied and Environmental Microbiology*. 2014;80(15):4599–4605. https://doi.org/10.1128/AEM.00895-14.
20. Rotaru, A.-E., Shrestha, P.M., Liu, F., Shrestha, M., Shrestha, D., Embree, M., Zengler, K., Wardman, C., Nevin, K.P., Lovley, D.R. A New Model for Electron Flow During Anaerobic Digestion: Direct Interspecies Electron Transfer to *Methanosaeta* for the Reduction of Carbon Dioxide to Methane. *Energy Environ Sci*. 2013;7(1):408–415. https://doi.org/10.1039/C3EE42189A.
21. Ha, P.T., Lindemann, S.R., Shi, L., Dohnalkova, A.C., Fredrickson, J.K., Madigan, M.T., Beyenal, H. Syntrophic Anaerobic Photosynthesis via Direct Interspecies Electron Transfer. *Nat Commun*. 2017;8(1):13924. https://doi.org/10.1038/ncomms13924.
22. Deng, X., Dohmae, N., Nealson, K.H., Hashimoto, K., Okamoto, A. Multi-heme Cytochromes Provide a Pathway for Survival in Energy-limited Environments. *Science Advances*. 2018;4(2):eaao5682. https://doi.org/10.1126/sciadv.aao5682.
23. McGlynn, S.E., Chadwick, G.L., Kempes, C.P., Orphan, V.J. Single Cell Activity Reveals Direct Electron Transfer in Methanotrophic Consortia. *Nature*. 2015;526(7574):531–535. https://doi.org/10.1038/nature15512.
24. Lovley, D.R., Phillips, E.J.P. Novel Mode of Microbial Energy Metabolism: Organic Carbon Oxidation Coupled to Dissimilatory Reduction of Iron or Manganese. *Appl Environ Microbiol*. 1988;54(6):1472. https://doi.org/10.1128/aem.54.6.1472-1480.1988.
25. Levar, C.E., Hoffman, C.L., Dunshee, A.J., Toner, B.M., Bond, D.R. Redox Potential as a Master Variable Controlling Pathways of Metal Reduction by *Geobacter sulfurreducens*. *ISME J*. 2017;11(3):741–752. https://doi.org/10.1038/ismej.2016.146.
26. Nealson, K.H., Rowe, A.R. Electromicrobiology: Realities, Grand challenges, Goals and Predictions. *Microbial Biotechnol*. 2016;9(5):595–600. https://doi.org/10.1111/1751-7915.12400.
27. Shi, L., Dong, H., Reguera, G., Beyenal, H., Lu, A., Liu, J., Yu, H.-Q., Frederickson, J.K. Extracellular Electron Transfer Mechanisms Between Microorganisms and Minerals. *Nat Rev Microbiol*. 2016;14(10):651–662. https://doi.org/10.1038/nrmicro.2016.93.
28. Lovley, D.R. Syntrophy Goes Electric: Direct Interspecies Electron Transfer. *Ann Rev Microbiol*. 2017;71(Volume 71, 2017):643–664. https://doi.org/10.1146/annurev-micro-030117-020420.
29. Lovley, D.R. Happy Together: Microbial Communities That Hook Up to Swap Electrons. *The ISME Journal*. 2017;11(2):327–336. https://doi.org/10.1038/ismej.2016.136.
30. Caccavo, F., Lonergan, D.J., Lovley, D.R., Davis, M., Stolz, J.F., McInerney, M.J. *Geobacter sulfurreducens* sp. nov., A Hydrogen- and Acetate-Oxidizing Dissimilatory Metal-Reducing Microorganism. *Appl Environ Microbiol*. 1994;60(10):3752–3759. https://doi.org/10.1128/aem.60.10.3752-3759.1994.
31. He, X., Chadwick, G., Jiménez, O.F., Orphan, V.J., Meile, C. Spatially Resolved Electron Transport through Anode-Respiring Geobacter sulfurreducens Biofilms:

Controls and Constraints. *ChemElectroChem*. 2021;8(10):1697–1697. https://doi.org/10.1002/celc.202100425.
32. Sharma, K., Palatinszky, M., Nikolov, G., Berry, D., Shank. E.A. Transparent Soil Microcosms for Live-cell Imaging and Non-destructive Stable Isotope Probing of Soil Microorganisms. *eLife*. 2020;9:e56275. https://doi.org/10.7554/eLife.56275.
33. Kuo, C.T., Faber, K.T. Permeable Carbon Nanotube-Reinforced Silicon Oxycarbide via Freeze Casting with Enhanced Mechanical Stability. *J Eur Ceram Soc.* 2020;40(6):2470–2479. https://doi.org/10.1016/j.jeurceramsoc.2019.12.059.
34. Kuo, C.T. Customized Porosity in Ceramic Composites via Freeze Casting. Ph.D.; California Institute of Technology.; 2021 https://doi.org/10.7907/88p1-5v79.
35. Arai, N., Faber, K.T. Hierarchical Porous Ceramics via Two-stage Freeze Casting of Preceramic Polymers. *Scr Mater*. 2019;162:72–76. https://doi.org/10.1016/j.scriptamat.2018.10.037.
36. Zeng, X., Arai, N., Faber, K.T. Robust Cellular Shape-Memory Ceramics via Gradient-Controlled Freeze Casting. *Adv Eng Mater.* 2019;21(12):1900398. https://doi.org/10.1002/adem.201900398.
37. Naviroj, M., Miller, S.M., Colombo, P., Faber, K.T. Directionally Aligned Macroporous SiOC via Freeze Casting of Preceramic Polymers. *J Eur Ceram Soc*. 2015;35(8):2225–2232. https://doi.org/10.1016/j.jeurceramsoc.2015.02.013.
38. Lovley, D.R. Dissimilatory Fe(III)- and Mn(IV)-Reducing Prokaryotes. In: Dworkin M, Falkow S, Rosenberg E, Schleifer K-H, Stackebrandt E, eds. *The Prokaryotes: Volume 2: Ecophysiology and Biochemistry*. New York, NY: Springer; 2006:635–658. https://doi.org/10.1007/0-387-30742-7_21.
39. General Preparative Techniques. *Iron Oxides in the Laboratory*. John Wiley & Sons, Ltd; 2000:19–25. https://doi.org/10.1002/9783527613229.ch02.
40. Ferrihydrite. *Iron Oxides in the Laboratory*. John Wiley & Sons, Ltd; 2000:103–112. https://doi.org/10.1002/9783527613229.ch08.
41. Naviroj, M., Voorhees, P.W., Faber, K.T. Suspension- and Solution-based Freeze Casting for Porous Ceramics. *J Mater Res*. 2017;32(17):3372–3382. https://doi.org/10.1557/jmr.2017.133.
42. Arai, N. Freeze Casting of Ceramics: Pore Design from Solidification Principles. Ph.D.; California Institute of Technology; 2021 https://doi.org/10.7907/3rmr-cz93.
43. Lafuente, B., Downs, R.T., Yang, H., Stone, N. The Power of Databases: The RRUFF Project. *Highlights in Mineralogical Crystallography, Berlin, Germany, W De Gruyter*. n.d.;p 1-30.

Chapter 6

FREEZE CASTING OF PRECERAMIC POLYMERS TO CREATE POROUS SILICON CARBIDE CERAMICS

This work was performed in collaboration with A. Cortez and N. Chen of the Jet Propulsion Laboratory under a President's and Director's Research and Development Fund grant entitled "Tunable Ceramic Optical Structures through Freeze Casting." A. Cortez performed carbothermal reduction experiments and collected X-ray diffraction data (Section 6.2.1.4). Thermal conductivity measurements were performed by Westmoreland Mechanical Testing & Research (Section 6.2.1.2), and thermogravimetric analyses were performed at California State University, Northridge, and at Westmoreland Mechanical Testing & Research (Section 6.2.1.3). N. Chen and K.T. Faber supervised the experimental work.

6.1. Introduction

Silicon carbide has emerged as a promising candidate material for next-generation space optical devices to be used both in space and on Earth[1]. As a material with both high stiffness with respect to weight and good thermal stability, SiC has been used as the mirrors aboard the Herschel telescope and the Rosetta Narrow Angle Camera (NAC)[2, 3]. It is currently in use in spacecraft ranging from CubeSats to the Sentinel-2 observation mission[4, 5]. However, the thermal loads on the mirrors of these telescopes are both high and complex, and as such telescopes need to be carefully designed both to minimize thermal expansion mismatch and to conduct heat away from the mirrors and delicate optical equipment[6, 7]. In seeking to fulfill both these objectives, as well as reduce weight and therefore launch costs, attention has turned to creating lightweight, all-SiC systems[1].

Incorporating porosity into materials is one method through which weight can be reduced, and porous SiC has already been explored for a wide variety of applications

from filters and catalyst supports to grinding materials[8–15]. Macroporous SiC has been shown to exhibit good mechanical strength and thermal shock resistance compared to dense SiC, in addition to the high chemical resistivity, thermal conductivity and low thermal expansion coefficients characteristic to SiC[16]. However, manufacturing both porous and dense SiC requires facile production methods that can be elusive when working exclusively with pure SiC.

While pure silicon carbide has a sintering temperature at or above 2000°C, polymeric precursors to SiC can be converted into Si-based ceramics at much lower temperatures[16–19]. These preceramic polymers have been studied for over fifty years as more easily manipulated precursors to SiC—both polysiloxanes and polycarbosilanes were shown to be promising precursors to SiC in the 1990s and 1970s, respectively[20, 21]. Polysiloxanes, which are comprised of a Si-O backbone and functionalized Si atoms, are converted to silicon oxycarbide, SiO_xC_y at temperatures as low as 1100°C[22]. The specific O:C ratio in pyrolyzed SiOC depends on the concentration and identity of the functional groups branching off the Si atoms in the Si-O backbone[23]. SiOC can then be converted into SiC by reduction at temperatures ranging from 1400-1700°C, significantly lower than the 2000°C sintering temperature normally required for sintering SiC[16, 18, 19]. Polycarbosilanes, which contain a Si-C backbone rather than the Si-O backbone found in polysiloxanes, can be converted to SiC at even lower temperatures—recent studies have produced β-SiC from polycarbosilane at 1200°C[24]. These lower-temperature synthetic routes for SiC from preceramic polymers open up a wide range of processing procedures to fabricate all-SiC parts in increasingly complex shapes while minimizing processing temperatures and material shrinkage.

Freeze casting has been well-established as a method for creating porous SiOC ceramics[25–30]. This work seeks to expand upon that previous work by utilizing freeze casting to create porous SiC with tailorable pore morphologies from porous SiOC. Porous SiOC ceramics were created through two routes: one utilizing polysiloxane-derived SiOC, and one utilizing click chemistry techniques to create porous SiOC

from polycarbosilane. Polysiloxane-derived SiOC, well-studied as a freeze casting by-product, was produced in a range of isotropic and anisotropic pore morphologies to explore the effect of anisotropy on thermal conductivity. Porous SiOC systems were then converted to SiC through carbothermal reduction at 1650°C to probe the feasibility of producing SiC ceramics from polysiloxane-derived SiOC. Finally, polycarbosilane-derived SiOC was produced as an alternate SiC precursor through a UV-assisted photopolymerization inspired by additive manufacturing techniques combined with the pore-forming freeze casting process.

6.2. Materials and Methods

6.2.1. Traditional freeze casting techniques

6.2.1.1. Freeze casting of ceramics

SiOC ceramics were prepared by dissolving between 5-40 wt.% MK powder (Wacker Chemie, Munich, Germany) in a solvent and adding 1 wt.% crosslinker (Geniosil GF91, Wacker Chemie, Munich, Germany). Specific solids loading concentrations and solvents used can be found in Table 6.1. The solution was then degassed under vacuum and poured into a 20 mm high, 24 mm diameter borosilicate ring lined with Mylar® sheeting (The Tape Casting Warehouse, Inc., Morrisville, PA, USA) and placed on a freeze casting setup described in previous work[25, 28, 31]. The solution was then freeze cast at the rate noted in Table 6.1. The freeze-cast sample was next placed in a lyophilizer (VirTis AdVantage 2.0, SP Scientific, Warminster, PA, USA) for at least 24 hours. After freeze drying, the porous polysiloxane was pyrolyzed under Ar for 4 hours at 1100°C in a tube furnace (Carbolite CTF 17/300 Tube Furnace, Haan, Germany). Pyrolyzed samples were then sliced along the freezing direction using a wafer dicing saw to produce a flat surface for imaging longitudinal cross-sections. One half of the sample was further sliced perpendicular to the freezing direction, producing transverse cross-sections for imaging. Cross-sections were coated with 10nm Pd/Pt before imaging on a Zeiss

1550 VP Scanning Electron Microscope (Carl Zeiss AG, Oberkochen, Germany). The pore size distribution of pyrolyzed samples was obtained through mercury intrusion porosimetry (AutoPore IV Mercury Intrusion Porosimeter, Micromeritics, Norcross, GA, USA).

Table 6.1. Freeze casting parameters for SiOC ceramics.

Sample	Solvent	Solids Loading	Coarsening Time	Freezing Front Velocity	Freezing Profile
Isotropic	Cyclooctane*	20 wt. %	0 h	15 μm/s	D.3
Columnar	Cyclohexane*	20 wt. %	2 h	15 μm/s	D.4
Dendritic	Cyclohexane*	20 wt. %	0 h	15 μm/s	D.2
Angled Dendritic	1,4-dioxane^	20 wt. %	0 h	15 μm/s	D.5
Lamellar	Tert-butanol^	20 wt. %	0 h	15 μm/s	D.6
5 wt.%	Cyclohexane*	5 wt. %	0 h	15 μm/s	D.2
10 wt.%	Cyclohexane*	10 wt. %	0 h	15 μm/s	D.2
15 wt. %	Cyclohexane*	15 wt. %	0 h	15 μm/s	D.2
20 wt.%	Cyclohexane*	20 wt. %	0 h	15 μm/s	D.2
30 wt. %	Cyclohexane*	30 wt. %	0 h	15 μm/s	D.2
40 wt.%	Cyclohexane*	40 wt. %	0 h	15 μm/s	D.2

***** Thermo Fisher Scientific, Waltham, MA, USA
^Sigma Aldrich, St. Louis, MO, USA

6.2.1.2. Thermal conductivity measurements

Thermal conductivity measurements were collected at Westmoreland Mechanical Testing & Research, Inc. (Youngstown, PA, USA). Diffusivity was measured via laser flash (ASTM E1461) using a sample of diameter 0.5 inches and height 0.125 inches. Specific heat was measured using differential scanning calorimetry (DSC) (ASTM E1269) of a sample 0.18 inches in diameter and 0.06 inches thick.

6.2.1.3. Thermal stability measurements

Unaltered polysiloxane powder, freeze-cast polysiloxane, pyrolyzed polysiloxane, and polycarbosilane were analyzed using thermal gravimetric analysis (TGA) at

California State University, Northridge. Samples were tested in argon with a ramp rate of 20°C/min from room temperature to 1200°C.

Pyrolyzed polysiloxane was further analyzed by TGA at Westmoreland Mechanical Testing & Research (Youngstown, PA, USA). The sample was held at 100°C in Ar to drive away water before being heated to 1600°C at a ramp rate of 10°C/min in Ar.

6.2.1.4. Conversion to SiC

Table 6.2. Hold temperatures and times for thermal profiles used in SiC conversion experiments.

Thermal Profile	Intermediate Hold Temperature (°C)	Intermediate Hold Time (h)	Ramp Rate (°C/min)		Maximum Hold Temperature (°C)	Maximum Hold Time (h)
			Low-T	High-T		
Thermal Profile 1	1550°C	0 h	40	5	1650	2
Thermal Profile 2	1550°C	0 h	20	5	1650	2
Thermal Profile 3	1425°C	1 h	5	2	1650	2

Dendritic SiOC ceramics were hot-pressed at the Jet Propulsion Laboratory (Pasadena, CA) in order to reduce SiOC to SiC. Samples were heated to 1650°C with various hold temperatures and ramp rates (Table 6.2 and Figure 6.1) using a custom-built hot press from Materials Research Furnaces (Allenstown, NH, USA). The converted SiC ceramics were then analyzed using X-ray diffraction (XRD) on a Panalytical Aeris Benchtop powder X-ray diffractometer (Malvern Panalytical, Worcestershire, UK) and scanning electron microscopy (Zeiss 1550 VP Scanning Electron Microscope, Carl Zeiss AG, Oberkochen, Germany).

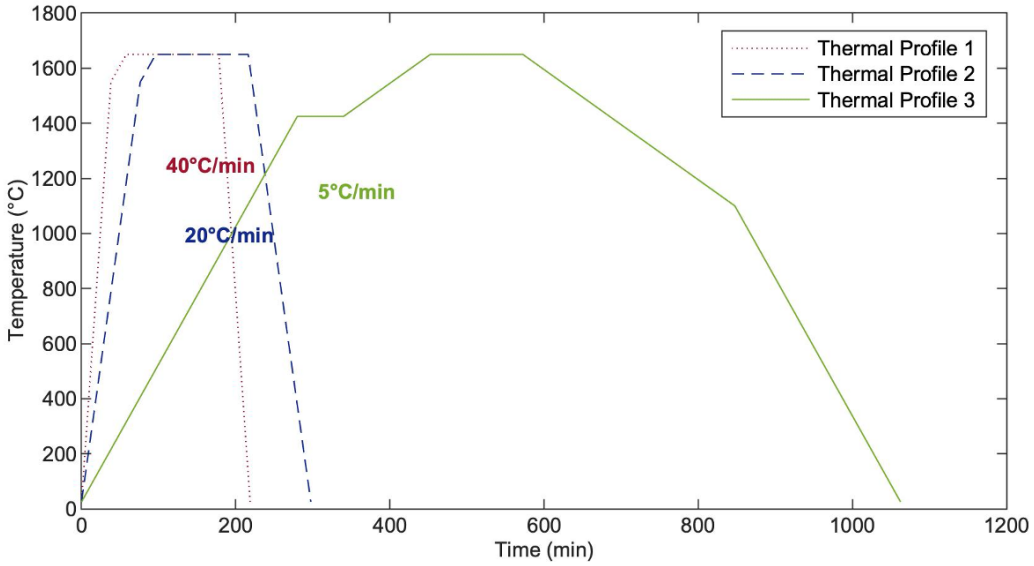

Figure 6.1. Thermal profiles 1, 2, and 3 for conversion of SiOC to SiC, each with a maximum hold temperature of 1650°C but differing ramp rates.

6.2.2. UV-assisted freeze casting techniques

6.2.2.1. UV effects on freeze-cast pore morphologies

To assess the effect of UV irradiation on frozen solvent crystals, four solutions to produce dendritic, isotropic, angled dendritic, and lamellar pore morphologies were prepared and as noted in Table 6.1. The solutions were poured into two borosilicate molds each, of outer diameter 14 mm, inner diameter 12 mm, and height 20 mm that had been lined with Mylar® sheeting. The samples were frozen simultaneously using freezing profile D.2. After the freezing setup had reached a temperature of -30°C, one sample of each solvent was removed from the freeze casting setup and placed in a lyophilizer to be freeze dried. The remaining four samples remained on the thermoelectric-controlled cold finger, which was held at -30°C, for 2 hours while being irradiated with a UV light (WACOOL Spiral Compact Reptile Light). After a 2-hour irradiation, the samples were removed from the freeze-casting setup and placed with the others in the lyophilizer. All samples were then pyrolyzed under Ar

for 4 hours at 1100°C in a tube furnace (Carbolite CTF 17/300 Tube Furnace, Haan, Germany) and analyzed using mercury intrusion porosimetry (AutoPore IV Mercury Intrusion Porosimeter, Micromeritics, Norcross, GA, USA). The spectrum of light emitted by the lightbulb was measured using an Andor Luminescence spectrometer (Oxford Instruments, Abingdon, UK).

6.2.2.2. UV-assisted freeze casting with polycarbosilane

Polycarbosilane solutions for freeze casting were prepared based on the technique outlined by Wang et al., utilizing thiol-ene click chemistry to induce photopolymerization of the polycarbosilane polymer[32]. First, 76 wt.% polycarbosilane preceramic polymer (SMP10, Starfire Systems, Inc., Glenville, NY, USA), 0.90 wt.% phenylbis(2,4,6-trimethylbenzoyl) phosphine oxide (BAPO) photoinitiator (Thermo Fisher Scientific, Waltham, MA, USA), 0.22 wt.% hydroquinone free radical scavenger (Thermo Fisher Scientific, Waltham, MA, USA), and 0.45 wt.% Sudan Orange G photoabsorber (Thermo Fisher Scientific, Waltham, MA, USA) were mixed together and sonicated for 90 minutes. After sonication, 22 wt.% 1,6-hexanedithiol (Thermo Fisher Scientific, Waltham, MA, USA) was added as a crosslinker, and the solution was stirred for 20 minutes.

This photoactive polycarbosilane solution was then added to 1,4-dioxane (Sigma Aldrich, St. Louis, MO, USA) or to tert-butanol (Sigma Aldrich, St. Louis, MO, USA) in a ratio of 20 wt.% polycarbosilane solution to 80 wt.% solvent, with wt.% calculated from total combined weight. These solutions were then frozen using freezing profile D.2 and irradiated for 2h with UV light. The samples were then freeze dried (VirTis AdVantage 2.0, SP Scientific, Warminster, PA, USA) and pyrolyzed in a tube furnace at 1100°C for 4 hours in Ar (Carbolite CTF 17/300 Tube Furnace, Haan, Germany). Pore morphologies were characterized using mercury intrusion porosimetry (AutoPore IV Mercury Intrusion Porosimeter, Micromeritics, Norcross, GA, USA) and scanning electron microscopy (Zeiss 1550 VP Scanning Electron Microscope Carl Zeiss AG, Oberkochen, Germany).

6.3. Results and Discussion

6.3.1. Polysiloxane-derived SiOC

6.3.1.1. Available pore morphologies

Methyl-functionalized polysiloxane preceramic polymer is soluble in a wide variety of solvents, and as such a range of pore morphologies was accessible through freeze casting of this preceramic polymer and pyrolysis to SiOC (Figure 6.2.). The five examples of pore morphologies shown in Figure 6.2. span from isotropic, sponge-like pore networks to highly aligned columnar pores. Isotropic pore morphologies, as visible in the first column of Figure 6.2, appeared the same whether cross-sectioned parallel or perpendicular to the freezing direction. The pore size distribution of isotropic morphologies was multimodal, with smaller pores than were visible in other pore morphologies. Columnar pore networks, by comparison, were highly anisotropic. With smooth pore walls and pores aligned with the freezing direction, as shown in the second column of Figure 6.2, the pore size distribution was unimodal and the pores in this morphology were larger than that exhibited in the isotropic morphology.

Isotropic and columnar pore morphologies occupy opposite ends of the spectrum between fully isotropic and fully anisotropic. In between these two extremes, dendritic pore morphologies exhibited tree-like branches of smaller pores off of the larger, main channel dendritic pores, as seen in the third column of Figure 6.2. The main-channel primary dendrites were approximately 25 μm and were highly aligned with the direction of the freezing front during freeze casting. The secondary dendrites, of order 12 μm, branched off from the primary dendrites at a 90° angle and produced a cross-like pore shape when viewed straight down the main channel pore. The pore size distribution of these morphologies was characteristically bimodal. The angle at which these dendrites branch off of the main channel pore was adjusted by changing the solvent used during freeze casting—when the solvent was switched

from cyclooctane to 1,4-dioxane (fourth column of Figure 6.2), secondary dendrites appeared at an angle to the primary pores, as dioxane crystals grow with secondary dendrites at an approximately 45° angle to the primary dendrite[26]. Both this angled dendritic pore morphology and the lamellar pore morphology seen in the last column of Figure 6.2 had larger pores than the first three morphologies discussed. The pores shown in the lamellar morphology were also generally aligned with the freezing direction, however, in this case the lack of interconnected pore walls made these samples somewhat fragile, and thus, difficult to image.

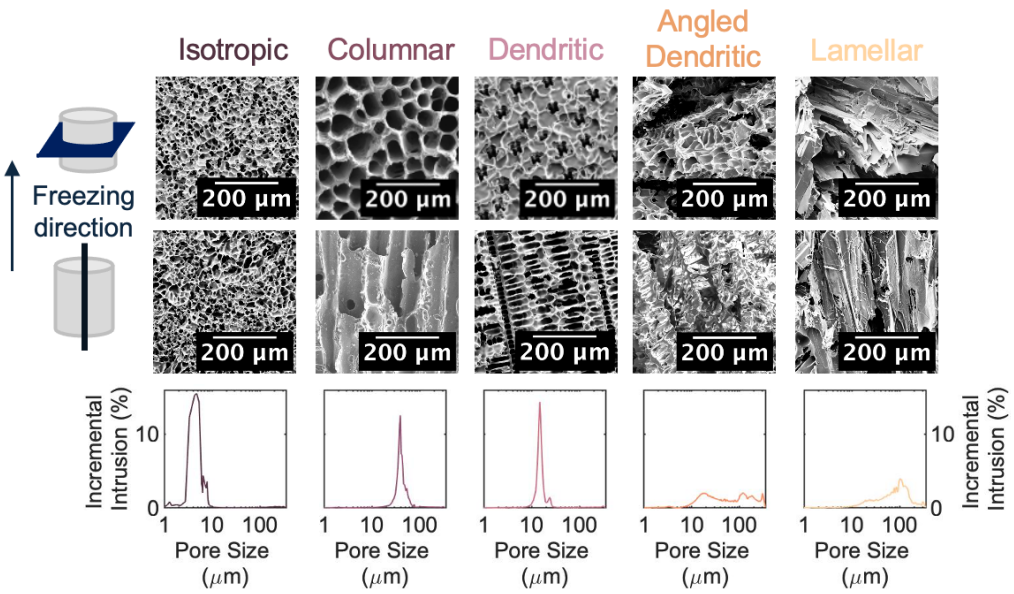

Figure 6.2. Scanning electron microscopy images and pore size distributions of SiOC ceramics with isotropic, columnar, dendritic, angled dendritic, and lamellar pores.

Adjusting the solids loading content of the polysiloxane in the freeze casting solution can also impact the pore morphology, as is seen in Figure 6.3. Through this, the pore sizes of dendritic pores were increased from the 25 µm and 12 µm primary and secondary pores sizes as large as 70 µm primary pores and 50 µm secondary pores when solids loading was decreased to 5 wt.%, and decreased to primary pores as small as 11 µm and secondary pores as small as 7 µm when solids loading was

increased to 40 wt.%. However, despite the large range of pore sizes available through the adjustment of solids loading, the characteristic cross-like pore shape of dendritic pores was visible in each transverse-cross section seen in Figure 6.3.

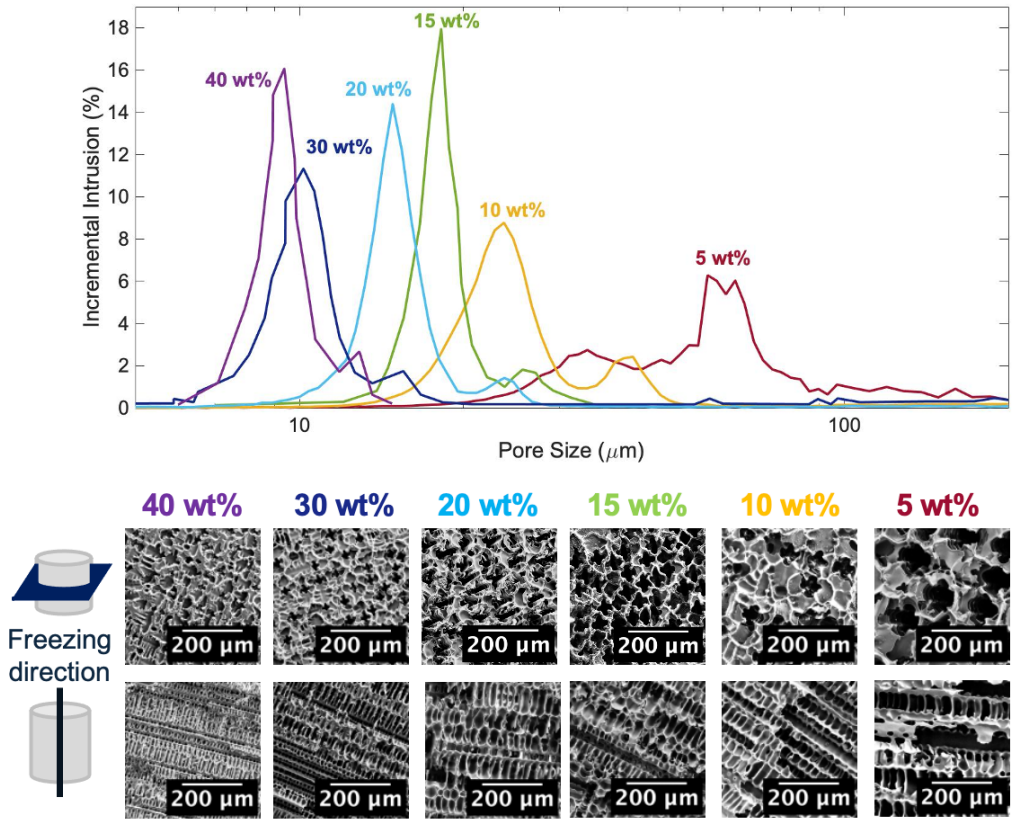

Figure 6.3. SEM images and pore size distribution of SiOC ceramics prepared with 5-40 wt.% polysiloxane in the initial freezing solution.

6.3.1.2. Thermal characteristics

To probe how these different pore morphologies impact the thermal conductivity of SiOC ceramics, the thermal conductivity was measured along the freezing direction and perpendicular to the freezing direction in three different morphologies: isotropic, dendritic, and columnar (Figure 6.4). These measurements revealed that while isotropic pore morphologies had quite similar thermal conductivities in both

directions, the same was not true for either dendritic or columnar pores. Both morphologies exhibited a significant difference in thermal conductivity when measured parallel or perpendicular to the freezing direction. That columnar morphologies exhibited the greatest difference in thermal conductivities is in line with this being the most anisotropic morphology, as their pore morphologies differ the most between transverse and longitudinal orientations. This study indicated that once converted to SiC, anisotropic thermal conductivity gradients could be engineered into porous SiC ceramics through the incorporation of highly anisotropic pore networks.

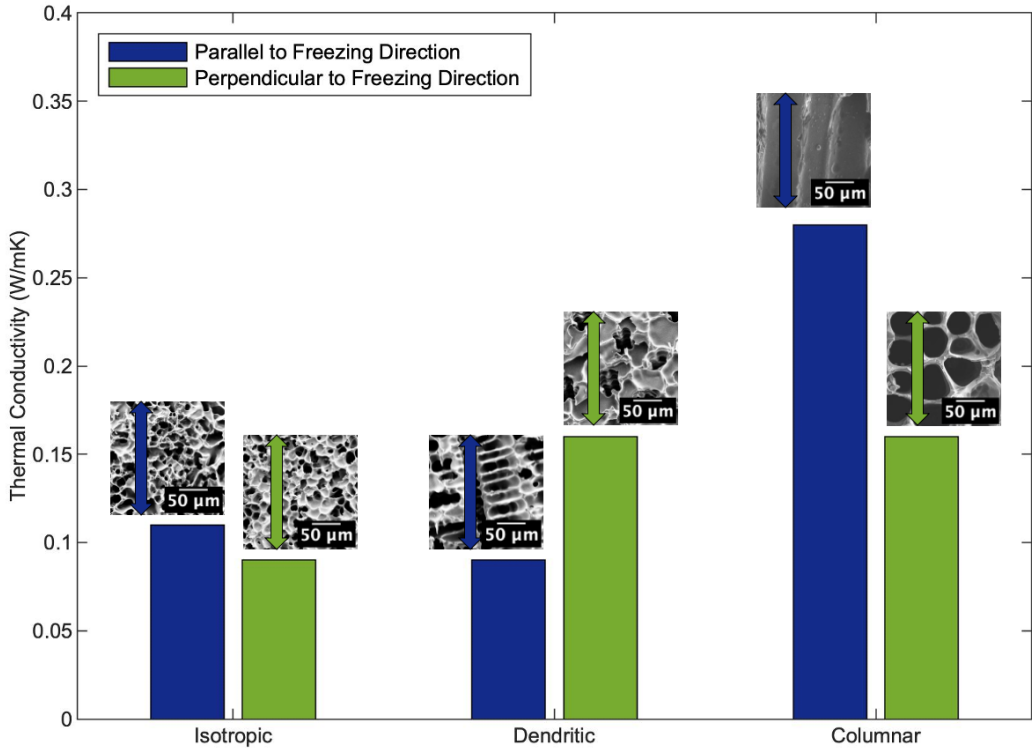

Figure 6.4. Thermal conductivity for isotropic, dendritic, and columnar SiOC ceramics, measured parallel to the freezing direction (blue) and perpendicular to the freezing direction (green).

While literature indicated that this conversion to SiC could take place in SiOC ceramics at temperatures as low as 1400°C, the conversion temperature depends on

several factors including the carbon content of the specific polysiloxane used. Thermogravimetric analysis (TGA) was used to probe the pyrolysis and SiC conversion temperatures specific to this methyl-functionalized, freeze-cast preceramic polymer (Figure 6.5a). As expected, when heated to 1200°C, un-altered polysiloxane exhibited the most mass loss (almost 50%). The first drop in mass for polysiloxane appeared beginning at 50°C, where water was baked out of the sample. Around 400°C, another ~10% drop in mass was observed, likely corresponding to the combustion of fugitive organic species. Finally, around 750°C the final drop in mass was observed, corresponding to pyrolysis of the polysiloxane into SiOC.

Polysiloxane that had been freeze-cast and -dried exhibited the same steep drop around 750°C corresponding to pyrolysis to SiOC, but no steep drops were seen between 100°C and 700°C, indicating that the freeze-drying process had removed many of the fugitive species causing the large mass loss seen in un-altered polysiloxane. Conversely, polysiloxane that had already been pyrolyzed into SiOC at 1100°C did not experience a large mass loss around 750°C, as expected from already-pyrolyzed SiOC, but did show a steep drop off around 400°C. As this pyrolyzed SiOC had been exposed to various solvents and cutting fluids while being machined into a piece approximately 10 mm by 10 mm by 5 mm for TGA analysis, this mass loss was once again likely due to the combustion of fugitive species from the ceramic.

The TGA data from the freeze-cast and -dried polysiloxane most closely resembled the thermal profile that freeze-cast samples are exposed to during pyrolysis into porous SiOC ceramics. That less than 20% of their mass is lost during this process confirms that the methyl-functionalized preceramic polymer used to produce porous SiOC results in a high ceramic yield after pyrolysis, another advantage to using this polymer to produce SiOC. Polycarbosilane, however, exhibited even less mass loss than the polysiloxane when heated to 1200°C, slightly less than 10%. Polycarbosilane's potential as a high-yield preceramic polymer will be discussed later in this chapter.

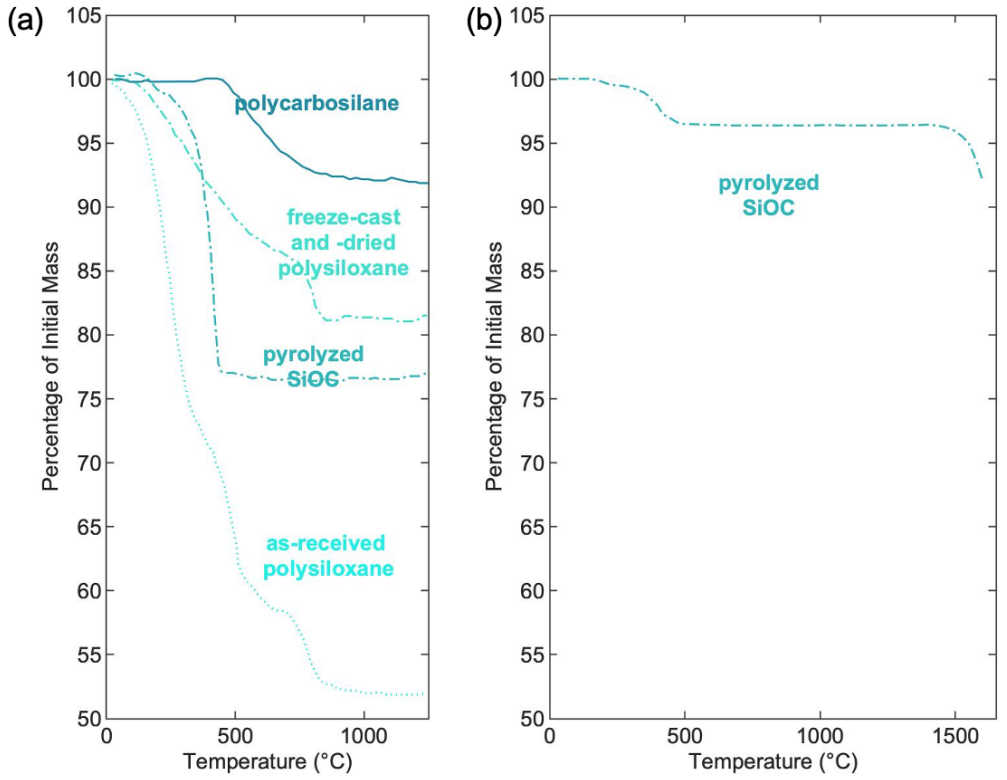

Figure 6.5. Thermal stability of preceramic polymers at various stages in the freeze casting process. Mass loss with respect to temperature of (a) as-received polysiloxane powder, freeze-cast and -dried polysiloxane, pyrolyzed SiOC, and polycarbosilane between 25 and 1200°C, and (b) of pyrolyzed SiOC ceramic between 25 and 1600°C.

While these TGA experiments provided useful insight into the chemical transformations occurring during pyrolysis, SiOC must be heated to at least 1400°C in order to be reduced to SiC. As such, a TGA experiment up to 1600°C was run on pyrolyzed SiOC (Figure 6.5b). Once again, following the combustion of fugitive species around 400°C, no mass loss was observed at higher temperatures, until temperatures around 1500°C were reached. At this point, the mass measurement dropped sharply, with approximately 4% mass loss observed between 1500°C and 1600°C. While TGA analysis is rare at temperatures higher than this, future experiments would indicate that even more substantial mass loss would occur at temperatures greater than 1600°C.

6.3.1.3. Conversion to SiC

Previous literature using polysiloxane to produce porous SiC had success with a sintering temperature of 1650°C, and as such this was chosen as the maximum temperature for each of the thermal profiles tested[18]. A SiOC sample heated using Thermal Profile 1 to 1650°C exhibited an XRD trace consistent with β-SiC (Figure 6.6). There was no significant amorphous character to the XRD trace, indicating that the sample had been fully converted to β-SiC from SiOC. However, this sample was mechanically fragile, and was only 4% of the mass of the initial SiOC sample. SEM imaging of this converted sample (Figure 6.7b) revealed no consistent pore morphology, despite the dendritic pores present before conversion to SiC (Figure 6.7a). The sample's fragility somewhat obscures the cause of the lack of dendritic pore morphology—it is possible that the pores collapsed during the rapid heating and cooling stages, but it is also possible that transporting the sample to the imaging facilities or cross-sectioning the sample destroyed any remaining clear dendritic pores. In either case, the fragility of the sample and lack of preservation of pore morphology led to alternate thermal profiles being tested.

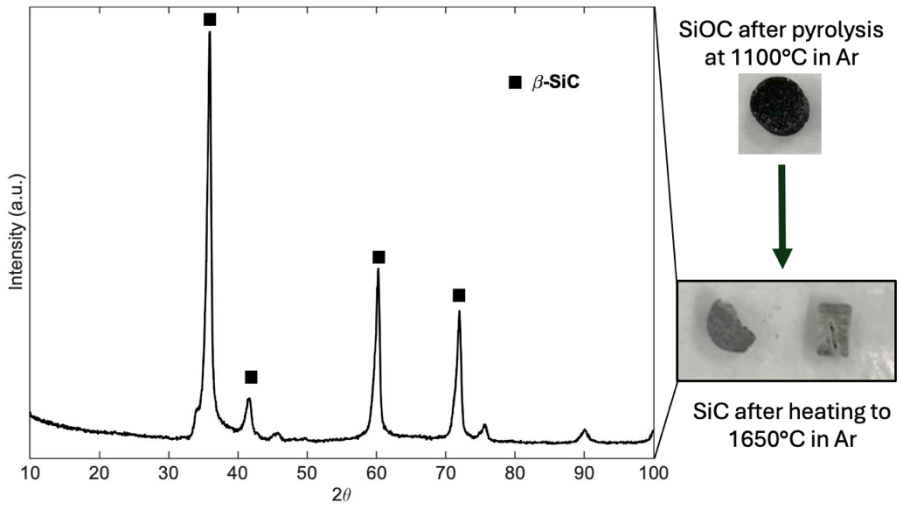

Figure 6.6. Photographs of porous SiOC before (top) and after (bottom) conversion to SiC by carbothermal reduction at 1650°C in Ar, and the corresponding XRD trace of the converted sample confirming conversion to β-SiC.

From the initial thermal profile with a ramp rate of 40°C/min, profiles with ramp rates of 20°C/min and 5°C/min were also tested (Figure 6.1). A dendritic SiOC sample heated under Thermal Profile 2 did exhibit some regions with dendritic pores after conversion to SiC at 1650°C (Figure 6.7c). While the pores in this sample were stable enough to survive the heating and cooling processes, and transport to the imaging facilities, this sample was still very fragile, and as such Thermal Profile 3 was tested next. SEM images of a sample converted to SiC under this thermal profile revealed some regions with clear dendritic characteristics, but some regions lacking a regular pore morphology (Figure 6.7d and e). The high-magnification view of the dendritic pores seen in Figure 6.7f further confirmed that while the dendritic pore morphology of the SiOC has been preserved throughout the conversion process, the pore walls were still thin and delicate.

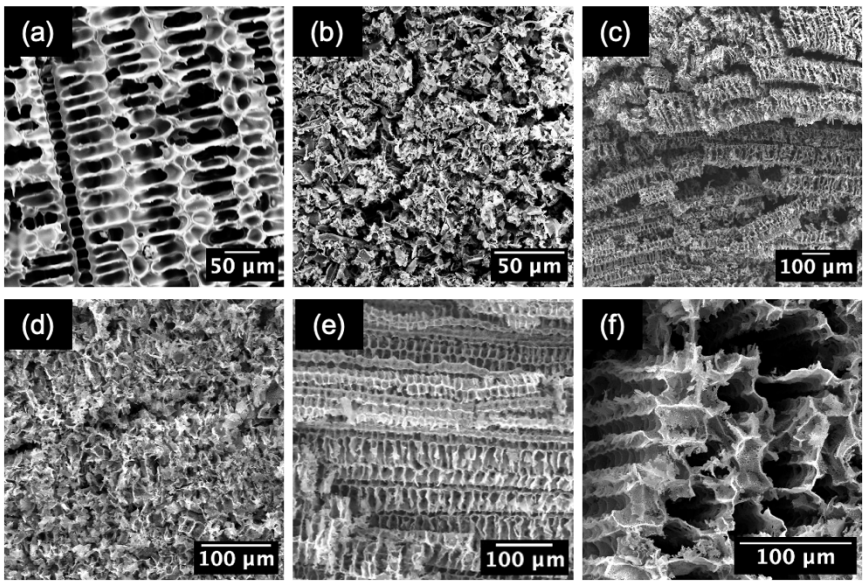

Figure 6.7. SEM images of (a) dendritic SiOC before conversion to SiC, (b) dendritic SiC after heating under Thermal Profile 1, (c) dendritic SiC after heating under Thermal Profile 2, (d) amorphous region of SiC after heating under Thermal Profile 3, (e) dendritic region of SiC after heating under Thermal Profile 3, and (f) thin pore walls of dendritic SiC after heating under Thermal Profile 3.

While decreasing the ramp rate used in the thermal profile did lead to improvements in sample robustness and preservation of pore morphology, the samples were still too fragile for further testing, or indeed for any structural applications. This lack of robusticity can be attributed to the low carbon content in the methyl-functionalized polysiloxane used to produce this porous SiOC. While this choice of preceramic polymer allowed for easy freeze-casting and high yields after pyrolysis at 1100°C, the lack of carbon in the SiOC matrix made conversion to SiC difficult. Without enough carbon to form Si-C bonds, the pore network was prone to collapse even when heated at slow rates.

6.3.2. Polycarbosilane-derived SiOC

To overcome the fragility of the samples after their conversion to SiC, it was necessary to introduce additional sources of carbon to the preceramic polymer green body formed during freeze casting. Methyl-functionalized polysiloxanes, while well-suited to freeze casting using traditional techniques, do not contain enough carbon to readily convert to SiC without additional carbon sources. However, polycarbosilanes contain a Si-C, rather than an Si-O, backbone, and had been previously shown to convert to SiC at relatively low temperatures[24]. However, polycarbosilanes that exhibit high ceramic yields can often present alternative challenges. SMP-10, a polycarbosilane with good ceramic yield, remains liquid at and below temperatures of -40°C. As the freeze-casting setup and freeze drier used in this work utilize minimum temperatures of -35°C, this preceramic polymer will not remain solid as the solvent pores are sublimated away in the freeze drier.

To overcome this challenge, alternate methods of solidifying this polycarbosilane preceramic polymer were explored. Previous work in the additive manufacturing community has utilized thiol-ene click chemistry to crosslink liquid preceramic polymers through a UV-activated photopolymerization[32]. Combining these techniques with the freeze casting process resulted in a workflow described in Figure

6.8, in which photo-active solutions were frozen, photocured with UV light, and freeze dried to produce porous, solid green bodies that can be pyrolyzed into SiOC.

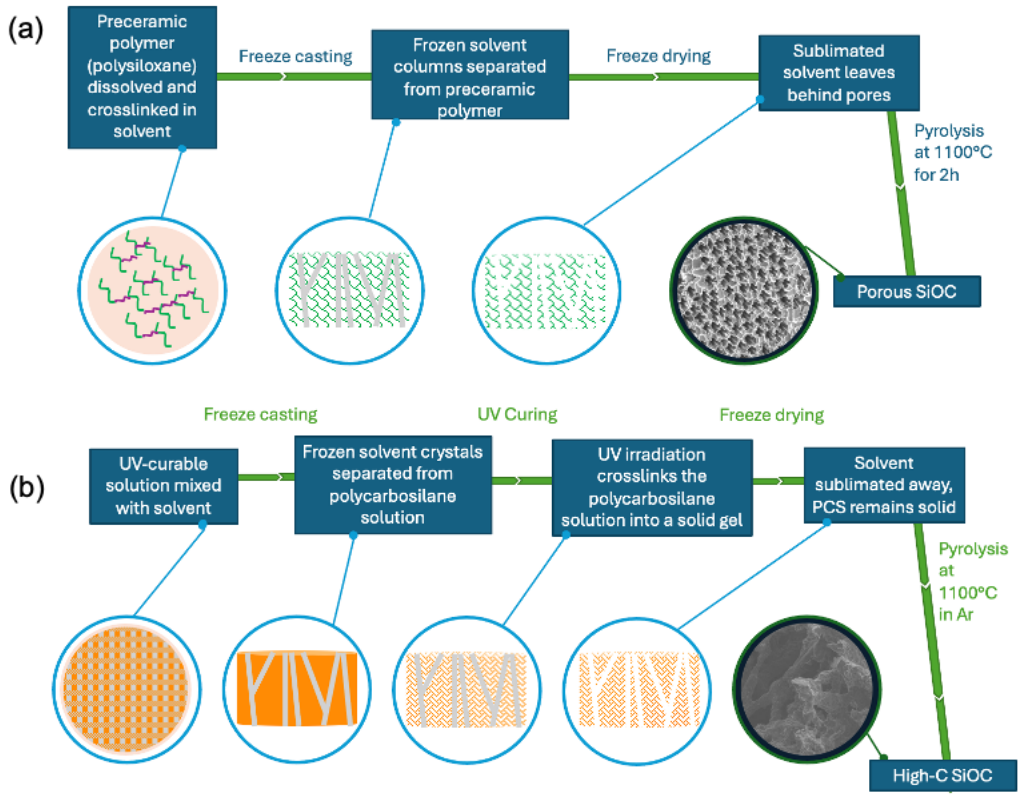

Figure 6.8. Workflow for (a) traditional freeze casting process and (b) UV-assisted freeze casting process to produce porous SiOC.

6.3.2.1. UV effects on pore morphologies

Before testing whether the UV-induced photopolymerization could be incorporated into the freeze casting process, it was necessary to probe whether the prolonged UV irradiation would impact the size or shape of the solvent crystals. To do so, samples using four different solvents were held at -30°C while being continuously irradiated with UV light, and their pore size distributions compared to samples that had been freeze-cast but not irradiated (Figure 6.9). In each case, while the shape of the pore size distribution was altered to some extent, the pores produced after 2h irradiation

with UV light were of almost the exact same size in each case. This indicated that neither the UV light nor the prolonged hold at -30°C had a substantial impact on the pore sizes produced through freezing each of these solvents.

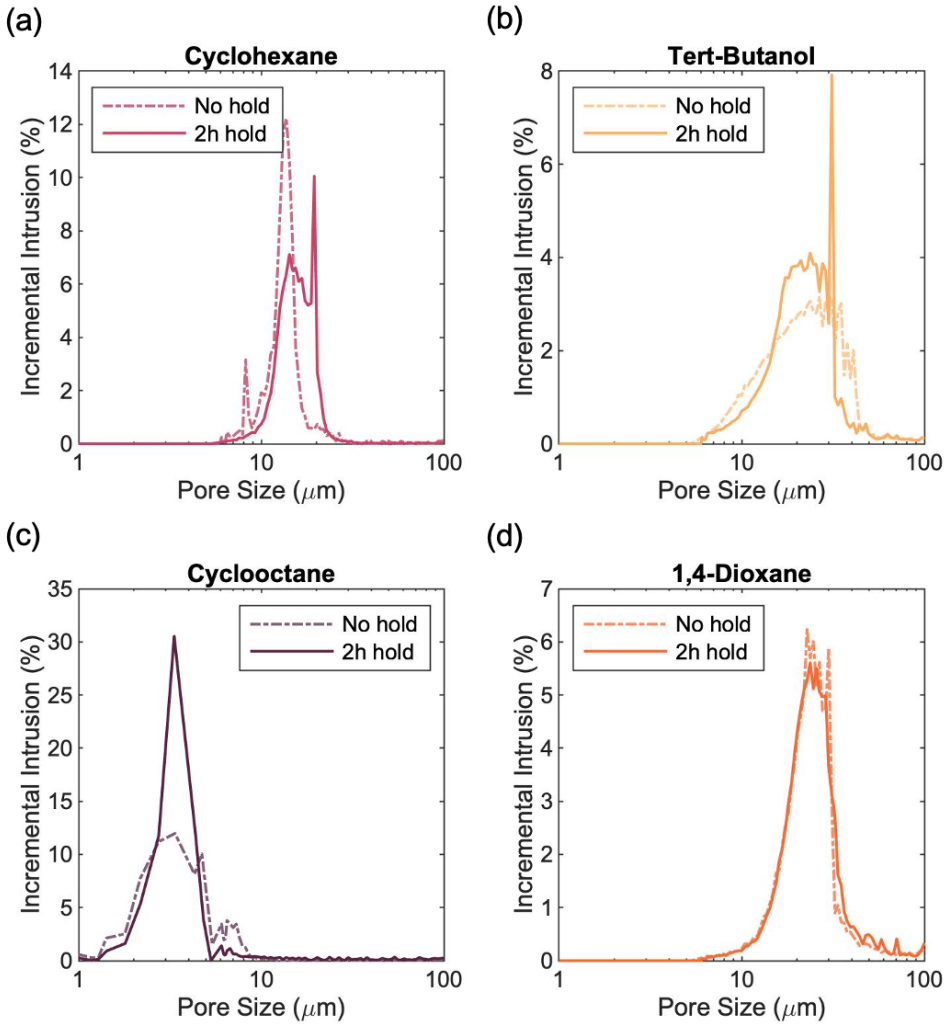

Figure 6.9. Pore size distributions of samples freeze cast with (a) cyclohexane, (b) tert-butanol, (c) cyclooctane, and (d) 1,4-dioxane that were and were not exposed to a 2h hold at -30°C while being irradiated with UV light.

Additionally, the spectrum of the UV bulb used in this experiment was taken to confirm that it was emitting UV light so as to induce photopolymerization (Figure 6.10). The spectrum confirms that while much of the light emitted by this amateur-

grade bulb was from the visible region of the spectrum, sufficient UV character was seen between 300-350nm to confirm that the bulb did emit some UV light.

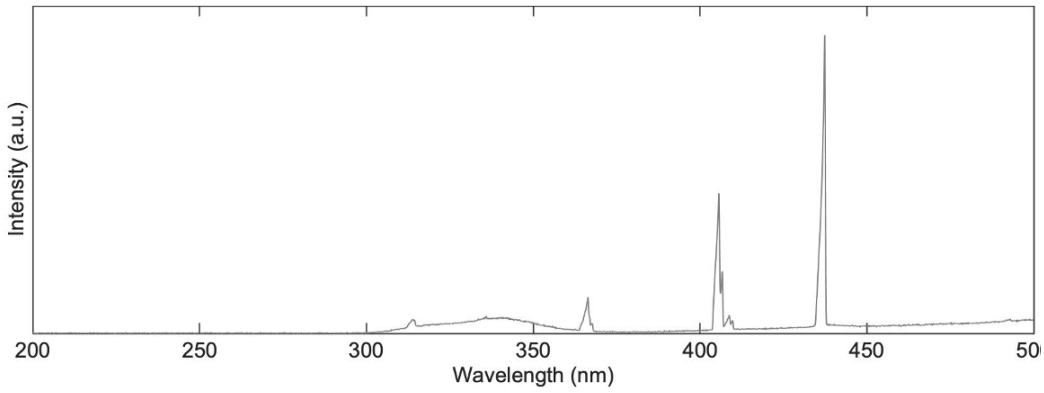

Figure 6.10. Emission spectrum of UV lamp.

6.3.2.2. UV-assisted freeze casting of polycarbosilane

As a UV-curing step could thus be incorporated into the freeze casting process without substantially altering the size of the pores produced, solutions of polycarbosilane with photoabsorbers, photoinitiators, free radical scavengers, and cross-linking agents were prepared and mixed with either 1,4-dioxane or tert-butanol. The solutions were able to be freeze cast, photocured into solid structures, then freeze dried and pyrolyzed at 1100°C. When imaged using SEM, both the pore structures produced using 1,4-dioxane and tert-butanol exhibited regular pore morphologies and robust structures strong enough to be easily imaged and analyzed using mercury intrusion porosimetry (Figure 6.11). Samples frozen with tert-butanol exhibited a large number of pores on the order of 20 μm, whereas samples frozen with dioxane exhibited a bimodal pore size distribution with larger pores on the order of 70 μm and smaller pores on the order of 50 μm, both of which are visible in the SEM images of the pore morphology.

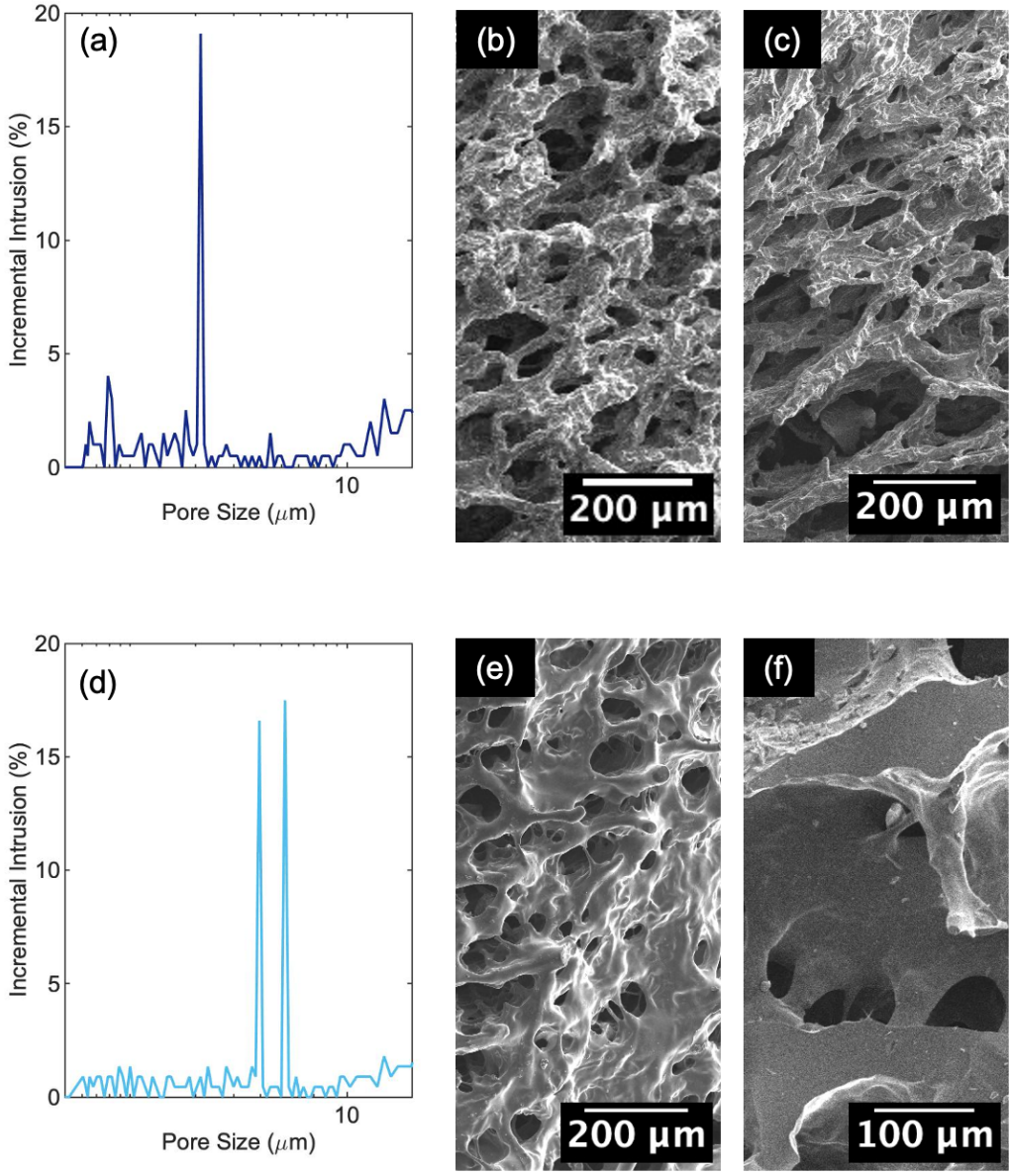

Figure 6.11. High-C SiOC samples produced through UV-assisted freeze casting. (a) Pore size distribution and (b,c) SEM images of porous polycarbosilane-derived SiOC prepared through UV-assisted freeze casting of a tert-butanol solution. (d) Pore size distribution and (e,f) SEM images of porous polycarbosilane-derived SiOC prepared through UV-assisted freeze casting of a 1,4-dioxane solution.

That this higher-C content SiOC was robust enough to be imaged and analyzed through porosimetry is a promising sign that it could potentially then be converted to porous SiC. As the use of polycarbosilane as the initial preceramic polymer meant that this SiOC had a much higher carbon content than did the polysiloxane-derived SiOC discussed in Section 6.3.1., it may be more robust after conversion to SiC at high temperatures.

6.4. Summary

To create porous SiC with anisotropic thermal properties to transfer heat in all-SiC space optical equipment, porous SiOC was first created for carbothermal reduction into SiC. To do so, two classes of SiOC-forming preceramic polymers were explored: polysiloxane and polycarbosilane. A methyl-functionalized polysiloxane preceramic polymer was chosen due to its frequent use in freeze casting as an easily soluble material that was a solid at room temperature. However, despite high ceramic yield, both the initial preceramic polymer and the resulting SiOC have relatively low carbon contents. Conversely, polycarbosilane was also studied as a point of comparison—while less frequently used in traditional freeze casting techniques, the presence of an Si-C backbone provided higher carbon contents in both the preceramic polymer and resulting SiOC.

A range of pore morphologies were available using polysiloxane in a traditional, suspension-based freeze-casting process, and this method of incorporating pores was also shown to engineer thermal anisotropy into SiOC ceramics. Additionally, thermal stability analysis of polysiloxane and the resultant SiOC confirmed that the freeze-cast preceramic polymer could be pyrolyzed to SiOC at 1100°C, and be stable once pyrolyzed up to 1500°C. However, a steep decline in mass around 1500-1600°C foreshadowed significant mass losses when polysiloxane-derived SiOC was reduced to SiC in inert atmospheres.

Initial attempts at a carbothermal reduction of SiOC to SiC showed that the polysiloxane-derived SiOC could indeed be fully converted to β-SiC through heating at 1650°C in Ar. However, the resulting samples weighed only 4% of the starting SiOC and were mechanically fragile. Decreasing the ramp rate to and from this temperature did slightly increase the robustness of the samples by reducing the rate of gas evolution and molecular rearrangement, and the resulting samples could be successfully imaged and the dendritic pore morphology of the initial SiOC preserved. However, even the most robust samples were still too fragile for further porosimetry or mechanical testing. This fragility was attributed to the low-C content of the polysiloxane-derived SiOC not providing enough material to produce a SiC structure with enough mass.

To counteract this, a higher-carbon content preceramic polymer, polycarbosilane, was turned to as an alternative candidate for fabrication of SiOC for carbothermal reduction to SiC. However, the polymer used remained in the liquid state until temperatures below -40°C, making it ill-suited for traditional freeze casting. Instead, an additive manufacturing-inspired photocatalyzed crosslinking procedure was integrated into the freeze casting process to create a porous preceramic polymer matrix. This UV-assisted freeze casting technique was shown not to substantially alter the size of solvent crystals but was able to create porous polycarbosilane structures in two solvent systems. Once converted to a higher-carbon content SiOC, these structures were shown to have regular pore structures, and be mechanically stable enough for further analysis. This procedure provides an alternate route for fabricating porous SiOC ceramic through freeze casting, with the potential to more easily produce porous SiC ceramics for thermal analysis.

6.5. References

1. Deny, P., Bougoin, M. Silicon Carbide Components for Optics: Present and Near Future Capabilities. *Optical Materials and Structures Technologies II*. Vol. 5868. International Society for Optics and Photonics; 2005:58680G. https://doi.org/10.1117/12.617226.

2. Toulemont, Y., Passvogel, T., Pilbratt, G., de Chambure, D., Pierot, D., Castel, D. The 3,5m All-SiC Telescope for Herschel. *International Conference on Space Optics — ICSO 2004*. Vol. 10568. SPIE; 2019:641–649. https://doi.org/10.1117/12.2500110.
3. Calvel, B., Castel, D., Standarovski, E., Rousset, G., Bougoin, M. Telescope and Mirrors Development for the Monolithic Silicon Carbide Instrument of the Osiris Narrow Angle Camera. *International Conference on Space Optics — ICSO 2000*. Vol. 10569. SPIE; 2017:144–162. https://doi.org/10.1117/12.2307938.
4. Wrbanek, J.D., Wrbanek, S.Y. Multidirectional Cosmic Ray Ion Detector for Deep Space CubeSats. 2016.
5. Breysse, J., Castel, D., Bougoin, M. All-SiC Telescope Technology at EADS ASTRIUM: Big Step Forward for Space Optical Payloads. *International Conference on Space Optics — ICSO 2012*. Vol. 10564. SPIE; 2019:982–991. https://doi.org/10.1117/12.2552106.
6. Wang, H., Cheng, J., Lou, Z., Liang, M., Zheng, X., Zuo, Y., Yang J. A Comparative Study of the Thermal Performance of Primary Mirror at the Four Typical Sites. *Optik*. 2018;174:727–738. https://doi.org/10.1016/j.ijleo.2018.05.008.
7. Banyal, R.K., Ravindra, B., Chatterjee, S. Opto-thermal Analysis of a Lightweighted Mirror for Solar Telescope. *Opt Express, OE*. 2013;21(6):7065–7081. https://doi.org/10.1364/OE.21.007065.
8. Suwanmethanond, V., Goo, E., Liu, P.K.T., Johnston, G., Sahimi, M., Tsotsis, T.T. Porous Silicon Carbide Sintered Substrates for High-Temperature Membranes. *Ind Eng Chem Res*. 2000;39(9):3264–3271. https://doi.org/10.1021/ie0000156.
9. Nagano, T., Sato, K., Saitoh, T., Iwamoto, Y. Gas Permeation Properties of Amorphous SiC Membranes Synthesized from Polycarbosilane without Oxygen-Curing Process. *J Ceram Soc Japan*. 2006;114(1330):533–538. https://doi.org/10.2109/jcersj.114.533.
10. Suda, H., Yamauchi, H., Uchimaru, Y., Fujiwara, I., Haraya, K. Preparation and Gas Permeation Properties of Silicon Carbide-based Inorganic Membranes for Hydrogen Separation. *Desalination*. 2006;193(1):252–255. https://doi.org/10.1016/j.desal.2005.04.143.
11. Fukushima, M., Zhou, Y., Miyazaki, H., Yoshizawa, Y.-I., Hirao, K., Iwamoto, Y., Yamazaki, S., Nagano, T. Microstructural Characterization of Porous Silicon Carbide Membrane Support With and Without Alumina Additive. *J Am Ceram Soc*. 2006;89(5):1523–1529. https://doi.org/10.1111/j.1551-2916.2006.00931.x.
12. Lee, J.-S., Lee, S.-H., Choi, S.-C. Improvement of Porous Silicon Carbide Filters by Growth of Silicon Carbide Nanowires Using a Modified Carbothermal Reduction Process. *J Alloy Compd*. 2009;467(1):543–549. https://doi.org/10.1016/j.jallcom.2007.12.042.
13. Keller, N., Pham-Huu, C., Roy, S., Ledoux, M.J., Estournes, C., Guille, J. Influence of the Preparation Conditions on the Synthesis of High Surface Area SiC for Use as a Heterogeneous Catalyst Support. *J Mater Sci*. 1999;34(13):3189–3202. https://doi.org/10.1023/A:1004681806843.
14. Zampieri, A., Sieber, H., Selvam, T., Mabande, G.T.P., Schwieger, W., Scheffler, F., Scheffler, M., Griel, P. Biomorphic Cellular Si/SiC/Zeolite Ceramic Composites:

From Rattan Palm to Bioinspired Structured Monoliths for Catalysis and Sorption. *Adv Mater*. 2005;17(3):344–349. https://doi.org/10.1002/adma.200400672.
15. Lim, K.-Y., Kim, Y.-W., Song, I.-H. Porous Sodium Borate-Bonded SiC Ceramics. *Ceram Int*. 2013;39(6):6827–6834. https://doi.org/10.1016/j.ceramint.2013.02.014.
16. Eom, J.-H., Kim, Y.-W., Raju, S. Processing and Properties of Macroporous Silicon Carbide Ceramics: A Review. *Journal of Asian Ceramic Societies*. 2013;1(3):220–242. https://doi.org/10.1016/j.jascer.2013.07.003.
17. Jana, D.C., Barick, P., Saha, B.P. Effect of Sintering Temperature on Density and Mechanical Properties of Solid-State Sintered Silicon Carbide Ceramics and Evaluation of Failure Origin. *J Mater Eng and Perform*. 2018;27(6):2960–2966. https://doi.org/10.1007/s11665-018-3397-4.
18. Eom, J.-H., Kim, Y.-W., Song, I.-H., Kim, H.-D. Processing and Properties of Polysiloxane-derived Porous Silicon Carbide Ceramics Using Hollow Microspheres as Templates. *J Eur Ceram Soc*. 2008;28(5):1029–1035. https://doi.org/10.1016/j.jeurceramsoc.2007.09.009.
19. Kim, Y.-W., Kim, S.-H., Song, I.-H., Kim, H.-D., Park, C.B. Fabrication of Open-Cell, Microcellular Silicon Carbide Ceramics by Carbothermal Reduction. *J Am Ceram Soc*. 2005;88(10):2949–2951. https://doi.org/10.1111/j.1551-2916.2005.00509.x.
20. Burns, G.T., Taylor, R.B., Xu, Y., Zangvil, A., Zank, G.A. High-temperature Chemistry of the Conversion of Siloxanes to Silicon Carbide. *Chem Mater*. 1992;4(6):1313–1323. https://doi.org/10.1021/cm00024a035.
21. Yajima, S., Hayashi, J., Omori, M. Continuous Silicon Carbide Fiber of High Tensile strength. *Chem Lett*. 1975;4(9):931–934. https://doi.org/10.1246/cl.1975.931.
22. Erb, D., Lu, K. Additive and Pyrolysis Atmosphere Effects on Polysiloxane-derived Porous SiOC Ceramics. *J Eur Ceram Soc*. 2017;37(15):4547–4557. https://doi.org/10.1016/j.jeurceramsoc.2017.06.036.
23. Colombo, P., Mera, G., Riedel, R., Sorarù, G.D. Polymer-Derived Ceramics: 40 Years of Research and Innovation in Advanced Ceramics. *J Am Ceram Soc*. 2010;93(7):1805–1837. https://doi.org/10.1111/j.1551-2916.2010.03876.x.
24. Wang, Y., Pei, X., Li, H., Xu, X., He, L., Huang, Z., Huang, Q. Preparation of SiC Ceramic Fiber From a Photosensitive Polycarbosilane. *Ceram Int*. 2020;46(18, Part A):28300–28307. https://doi.org/10.1016/j.ceramint.2020.07.333.
25. Naviroj, M., Miller, S.M., Colombo, P., Faber, K.T. Directionally Aligned Macroporous SiOC via Freeze Casting of Preceramic Polymers. *J Eur Ceram Soc.* 2015;35(8):2225–2232. https://doi.org/10.1016/j.jeurceramsoc.2015.02.013.
26. Naviroj, M., Voorhees, P.W., Faber, K.T. Suspension- and Solution-based Freeze Casting for Porous Ceramics. *J Mater Res*. 2017;32(17):3372–3382. https://doi.org/10.1557/jmr.2017.133.
27. Naviroj, M., Wang, M.M., Johnson, M.T., Faber, K.T. Nucleation-controlled Freeze Casting of Preceramic Polymers for Uniaxial Pores in Si-based Ceramics. *Scr Mater*. 2017;130:32–36. https://doi.org/10.1016/j.scriptamat.2016.10.038.
28. Arai, N., Faber, K.T. Hierarchical Porous Ceramics via Two-stage Freeze Casting of Preceramic Polymers. *Scr Mater*. 2019;162:72–76. https://doi.org/10.1016/j.scriptamat.2018.10.037.

29. Arai, N., Faber, K.T. Freeze-cast Honeycomb Structures via Gravity-enhanced Convection. *J Am Ceram Soc*. 2021;104(9):4309–4315. https://doi.org/10.1111/jace.17871.
30. Arai, N., Faber, K.T. Gradient-controlled Freeze Casting of Preceramic Polymers. *J Eur Ceram Soc*. 2023;43(5):1904–1911. https://doi.org/10.1016/j.jeurceramsoc.2022.12.016.
31. Zeng, X., Arai, N., Faber, K.T. Robust Cellular Shape-Memory Ceramics via Gradient-Controlled Freeze Casting. *Adv Eng Mater*. 2019;21(12):1900398. https://doi.org/10.1002/adem.201900398.
32. Wang, X., Schmidt, F., Hanaor, D., Kamm, P.H., Li, S., Gurlo, A. Additive Manufacturing of Ceramics from Preceramic Polymers: A versatile Stereolithographic Approach Assisted by Thiol-ene Click Chemistry. *Additive Manufacturing*. 2019;27:80–90. https://doi.org/10.1016/j.addma.2019.02.012.

Chapter 7

SUMMARY AND SUGGESTIONS FOR FUTURE WORK

In this work, an understanding of how the chemistry and porosity of ceramic structures interact was developed and utilized to create functional porous ceramics for three different applications: shape memory ceramic materials, habitats for bacterial colonization, and thermally anisotropic materials for space optics and other high temperature applications. Through these studies, the chemistry and porosity of each material explored was carefully tuned to suit the ceramic system and the final intended application. Several different chemical and physical levers, including sol-gel synthesis methods, heat treatments, and contrasting preceramic polymers, among others, were deployed to control the chemical character of these ceramic systems. Through freeze casting of both suspensions and solutions, porous ceramic structures were created with a range of anisotropic and isotropic pore morphologies and pore sizes. In each case, the porosity and chemistry are intertwined, and only through careful development of both aspects can these porous ceramics become useful for their intended purposes.

7.1. Shape Memory Ceramics

The first set of porous ceramics examined were ceria-stabilized zirconia honeycombs for use as ceramic shape memory materials. Control over dopant chemistry enabled the study of shape memory and superelastic behaviors at room temperature, and the incorporation of highly anisotropic, columnar pores was necessary for accommodation of the martensitic transformation, and its associated volume change in a polycrystalline zirconia material. Through a rule-of-mixtures approach, a procedure to calculate the relative phase contents of ceria-stabilized zirconia ceramics from Raman spectra was developed and utilized to track the progression of the martensitic transformation in shape memory and superelastic zirconia samples. The complementary quantitative analysis from X-ray diffraction and Raman spectra allowed for exploration of the shape memory effect over multiple cycles of compression and annealing, and incorporating analysis from Raman spectroscopy highlighted the

inhomogeneity of the martensitic phase transformation across the surface of a cylindrical sample. Using Raman spectroscopy along with *in-situ* and diamond anvil cell compression, superelastic effects were observed for the first time in a polycrystalline zirconia system.

The techniques developed in this study can be utilized to expand upon the understanding of the shape memory and superelastic behaviors in polycrystalline zirconia ceramics. Future work may thus focus on several potential areas of investigation. First, it may focus on correlating pore density with phase transformations. One of the benefits of tracking phase transformation through Raman spectroscopy is the ability to correlate spectra with specific locations on the sample, and simultaneously image those locations using an optical microscope coupled to the Raman spectrometer. Features such as pores, edges, and corners may create more complex stress fields, and thus contribute to the inhomogeneity of phase transformation in shape memory zirconia samples, and correlating location with spectra may shed light on the role each feature plays in promoting or inhibiting the martensitic transformation.

Second, Raman spectroscopy also enabled study of superelastic zirconia samples through compression using a diamond anvil cell. However, the specific pressure applied was difficult to calculate because of the lack of a pressure-transmitting medium. Additionally, the pressures needed to trigger the martensitic transformation in these ceramics were expected to be several orders of magnitude lower than those typically induced by diamond anvil cells, and thus typical calibration techniques such as the use of ruby fluorescence shifts to calculate pressure will not accurately calculate the pressures applied in this scenario. Alternate materials could therefore be explored as a calibration material to calculate pressures on the order of tens of MPa.

Finally, the spectroscopic techniques explored in this work were limited in terms of their penetration depth to only several microns below the surface. Analysis of shape memory and superelastic zirconia samples at higher-powered spectroscopic sources such as synchrotron facilities would provide much more information on the extent of the martensitic transformation throughout the depth of the sample.

7.3. Thermally Anisotropic Materials for Space Optics

The final class of porous materials explored in this work was silicon-based porous ceramics for use as anisotropic thermal conductors in all SiC optical systems. Silicon oxycarbide derived from both polysiloxane and polycarbosilane was produced as a potential precursor for carbothermal reduction to SiC. While a range of pore morphologies was produced in polysiloxane-derived systems and anisotropic thermal conductivity was observed in anisotropic SiOC systems, the pore morphology did not survive attempts at carbothermal reduction. Although the reduced samples were found to have been fully converted to β-SiC, they were too fragile for further testing. Subsequently, a combined photopolymerization-freeze-casting procedure inspired by additive manufacturing techniques was developed to create porous, SiOC from polycarbosilane. The prolonged exposure to UV light did not significantly alter pore size, and robust porous SiOC with regular pore morphologies was created.

Future work with these systems could investigate creating SiC from both porous polysiloxane-derived and polycarbosilane-derived SiOC. As methyl-functionalized polysiloxane does not yield SiOC with enough C for conversion to SiC while preserving pore morphology, increasing the carbon content through addition of alternate carbon sources may yield more robust SiC structures. With regards to the polycarbosilane-based approach, while the preliminary results of regular pore morphology in polycarbosilane-derived SiOC were promising, scaling the UV-assisted freeze casting procedure to sizes comparable with those utilized in traditional freeze casting techniques and more pore morphologies would allow for deeper exploration of pore formation and solvent crystal behavior during the click-chemistry photoreaction. Finally, the polycarbosilane-derived SiOC can be exposed to the same high temperatures in inert environments as the polysiloxane-derived SiOC, and the chemistry and robusticity of the resulting porous structures compared. As the polycarbosilane-derived SiOC should have a higher C:O ratio than the polysiloxane-derived SiOC does, it may yield porous SiC with greater mechanical stability than the porous SiC produced in this work.

A p p e n d i x A

PEAK INTENSITY CALCULATION METHODS AND TEST SPECTRA

Calculating the V_m using Equations 2.1-4 yields poor fits to the V_m as calculated from XRD traces regardless of how the peak intensity value is obtained. Whether peak intensity values are taken through simple intensity measurements, intensity measurements with the background values subtracted, or through deconvolution of the various peaks present, the trend remains the same (Figure A.1).

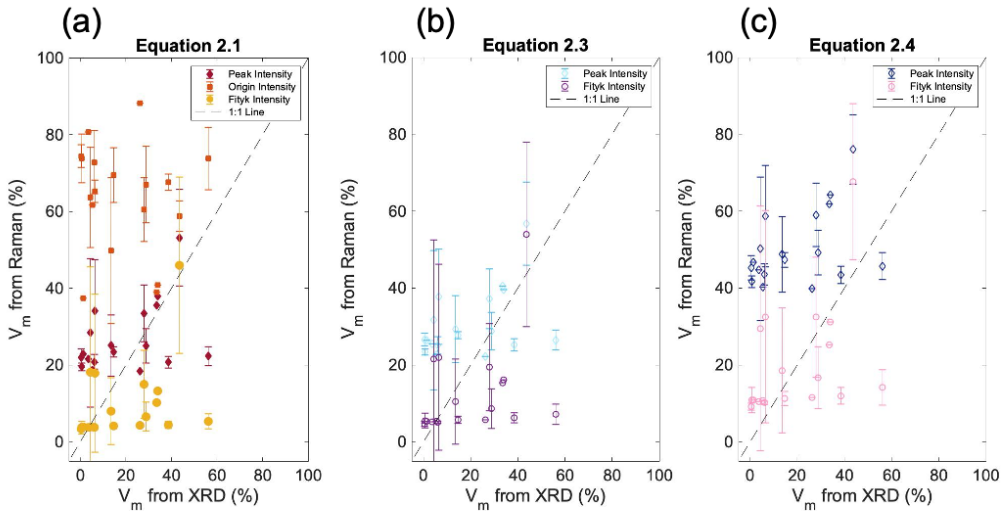

Figure A.1. Using peak intensities derived from the raw peak intensity and the peak intensity from spectra deconvoluted using OriginPro or Fityk software, monoclinic phase content from Raman spectra were calculated using (a) Equation 2.1, (b) 2.3, and (c) 2.4, compared to the monoclinic phase content as calculated through XRD traces using Equations 2.5-6. The line where the two values would be equal is shown in black.

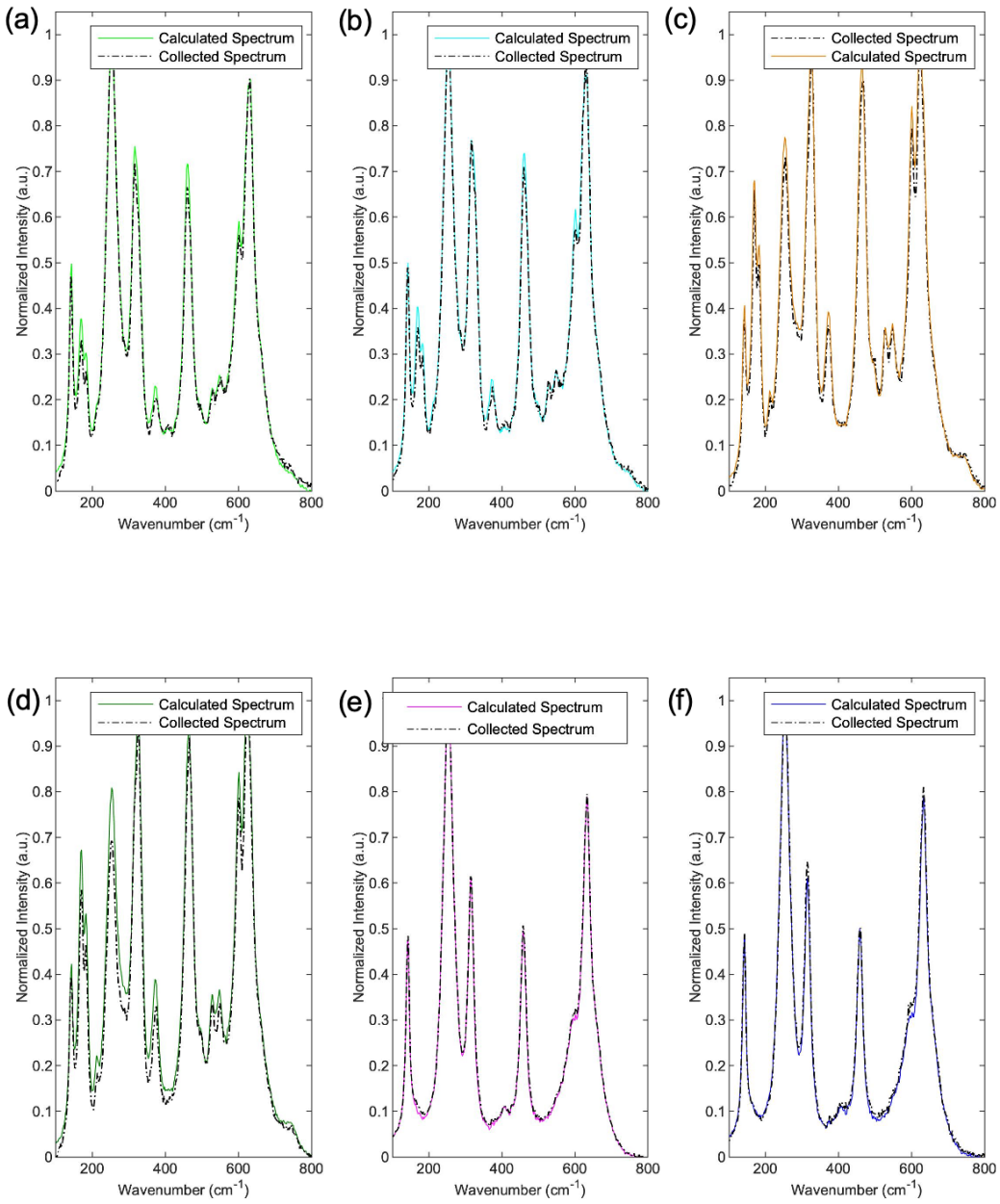

Figure A.2. Selected spectra of experimentally obtained test cases (dashed lines), with the composite spectrum corresponding to the calculated V_m overlaid (solid lines), in addition to those shown in Figure 2.8.

A p p e n d i x B

ADDITIONAL INFORMATION ON SHAPE MEMORY AND SUPERELASTIC CERIA-STABILIZED ZIRCONIA CERAMICS

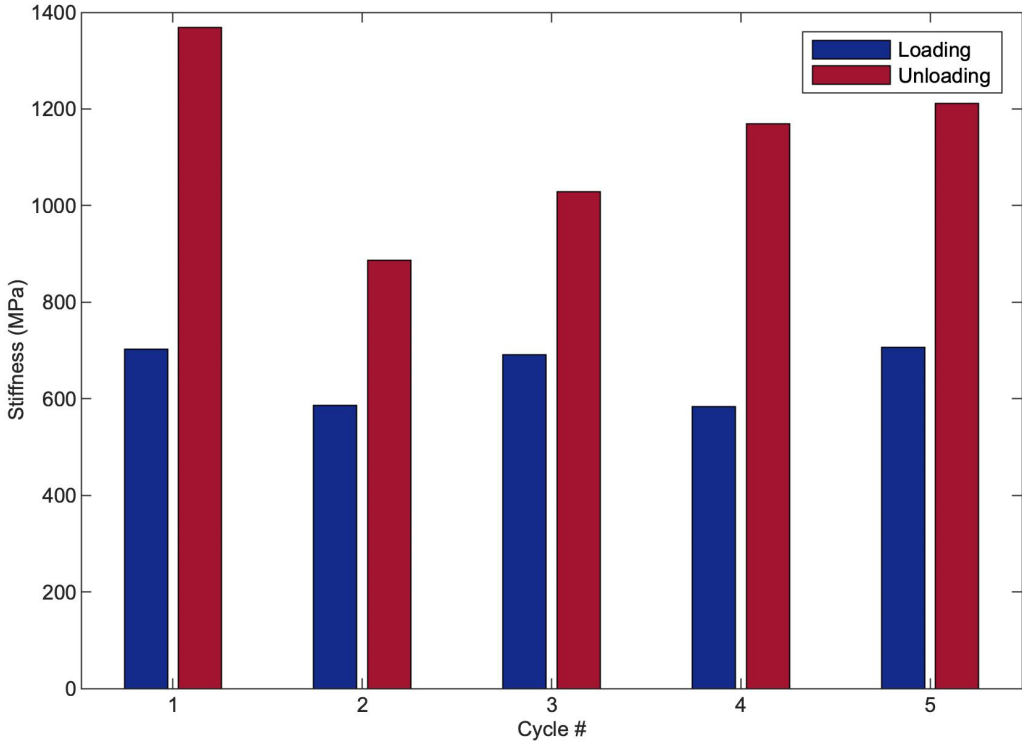

Figure B.1. Stiffness values of a 12.5 mol% CSZ sample on loading and unloading over multiple cycles, as calculated from the slope of the linear portion of the loading and unloading region of each cycle's stress-strain curve.

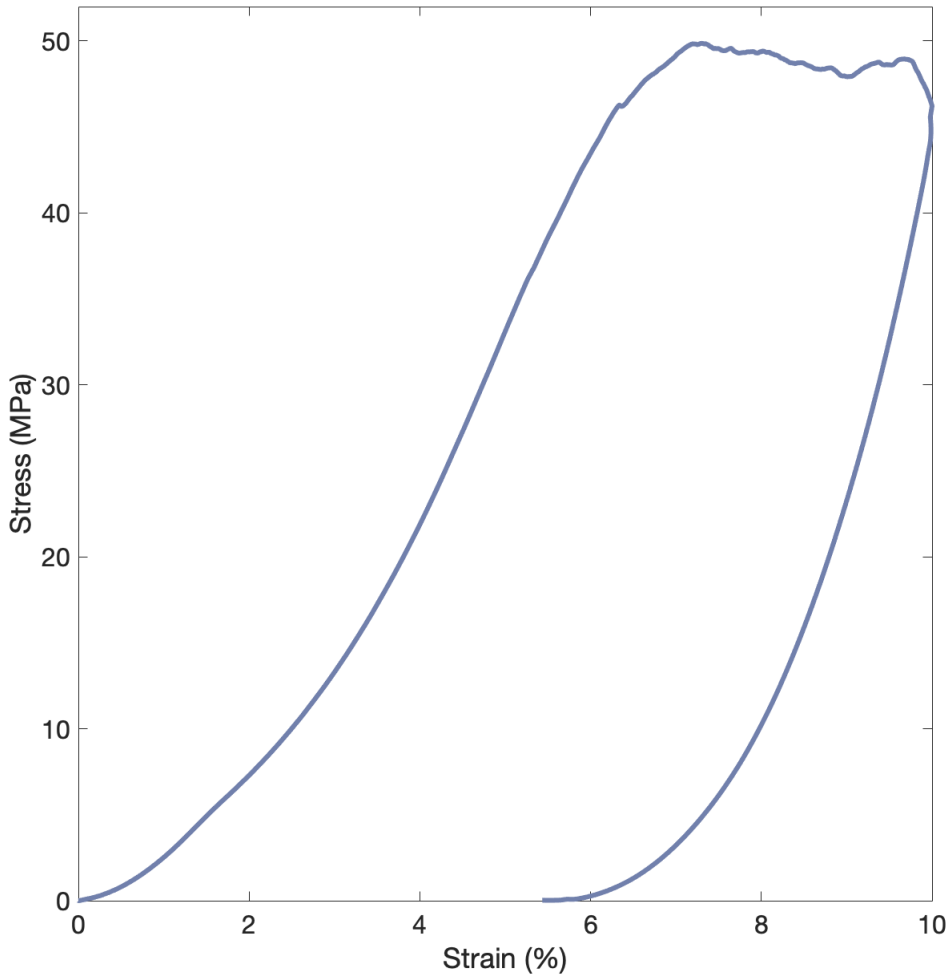

Figure B.2. Stress-strain plot of a 16.0 mol% CSZ sample indicates that a martensitic transformation from the tetragonal to the monoclinic phase has occurred over multiple different stress values, as is observed in 12.5 mol% CSZ samples.

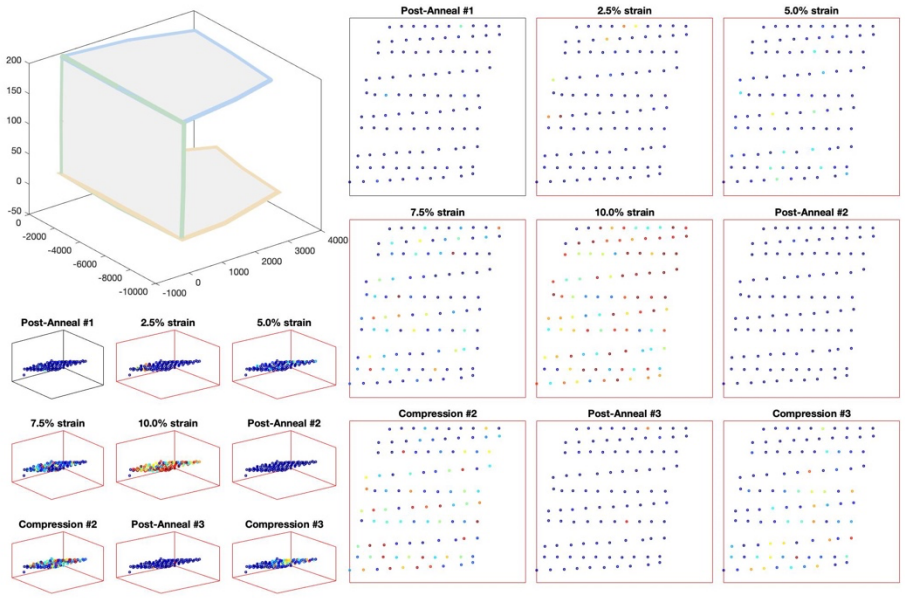

Figure B.3. By plotting V_m as obtained through Raman spectra as a function of the position on the sample at which each spectrum was collected, the phase content of a sample could be mapped across real space. In these examples, only the locations from Post-Anneal #1 are accurate, and the others reuse those same positions for these figures, although the spectra from those experiments were not taken from the same locations.

A p p e n d i x C

ADDITIONAL CONFOCAL AND SCANNING ELECTRON MICROSCOPY OF POROUS CRYOLITE CERAMICS

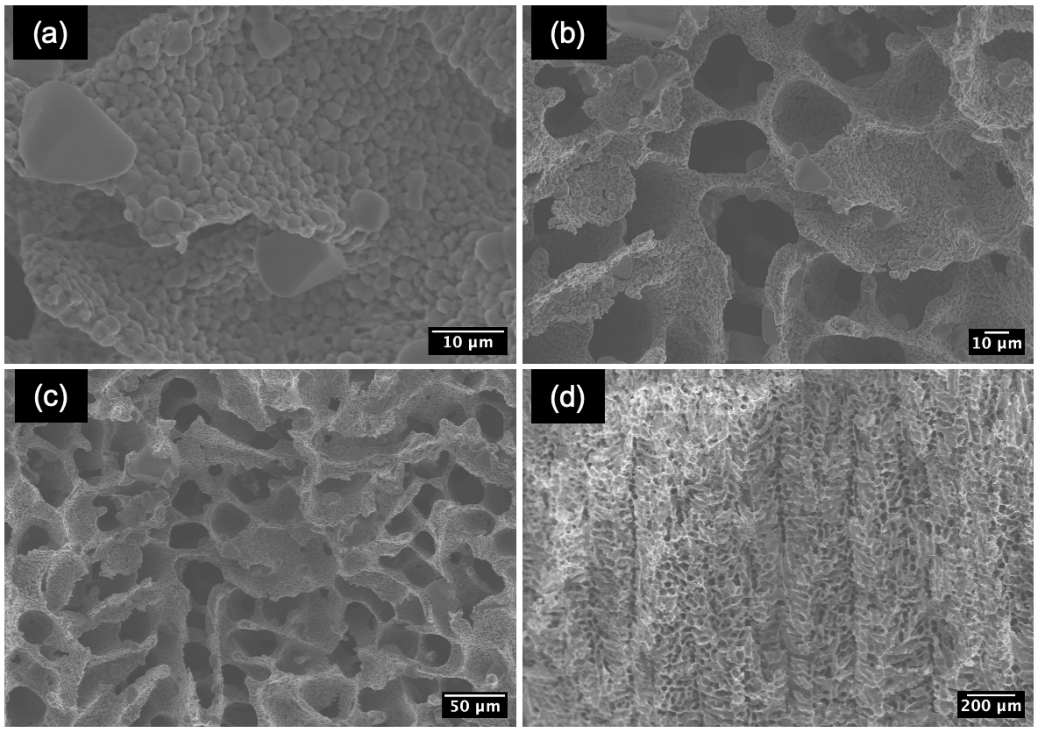

Figure C.1. Additional SEM images of a 12 vol% dendritic cryolite sample sintered at 900°C for 6 hours.

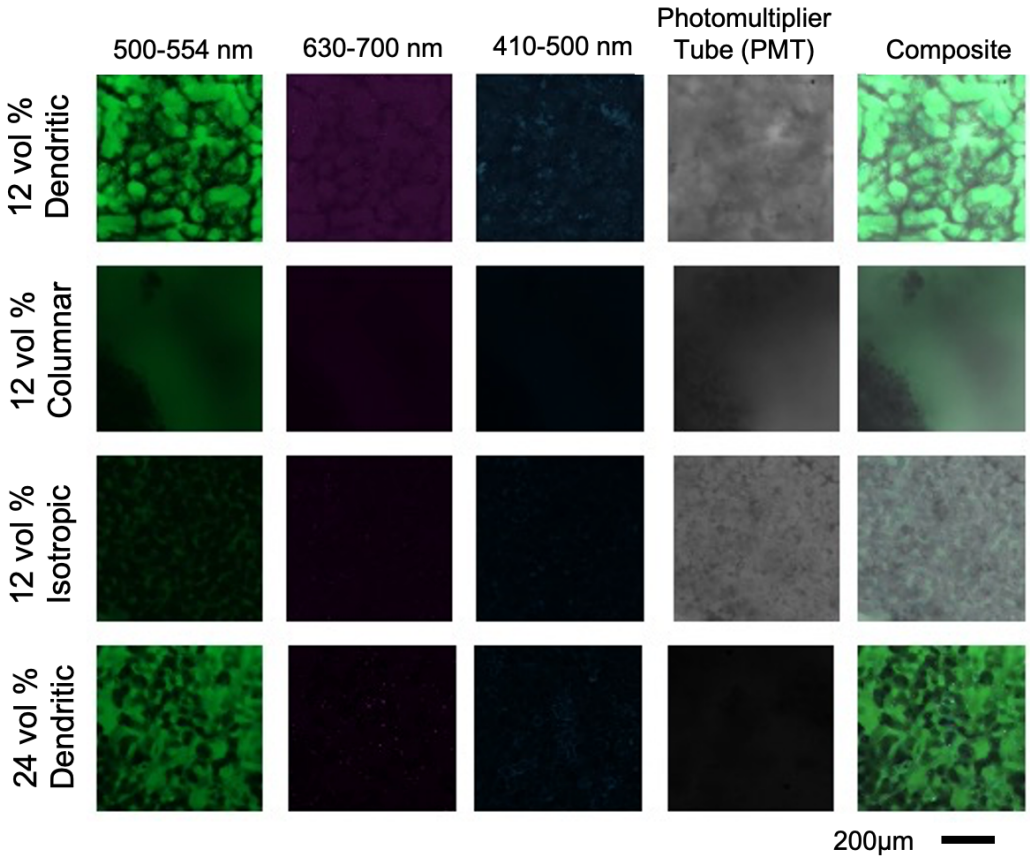

Figure C.2. Individual channel images of the cryolite coupons shown in Figure 4.7.

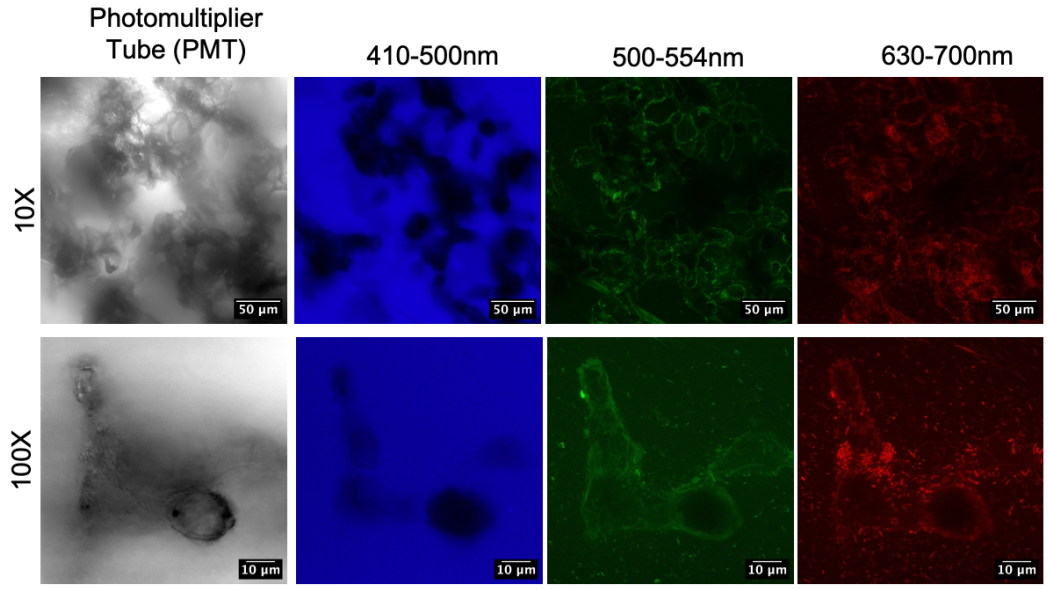

Figure C.3. Individual channel images of the cryolite coupon inoculated with Pseudoalteromonas bacteria shown in Figure 4.16.

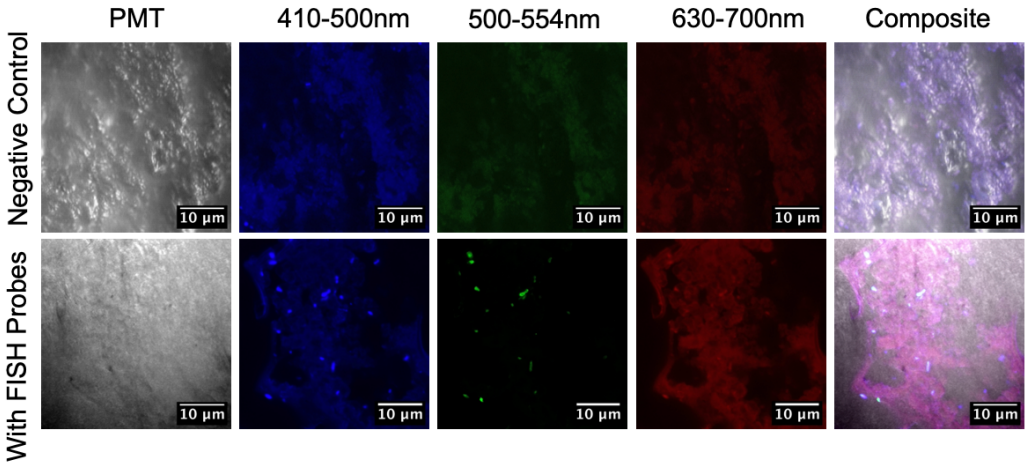

Figure C.4 Individual channel images of the negative control coupon (incubated without FISH probes) and the coupon incubated with FISH probes shown in Figure 4.17a.

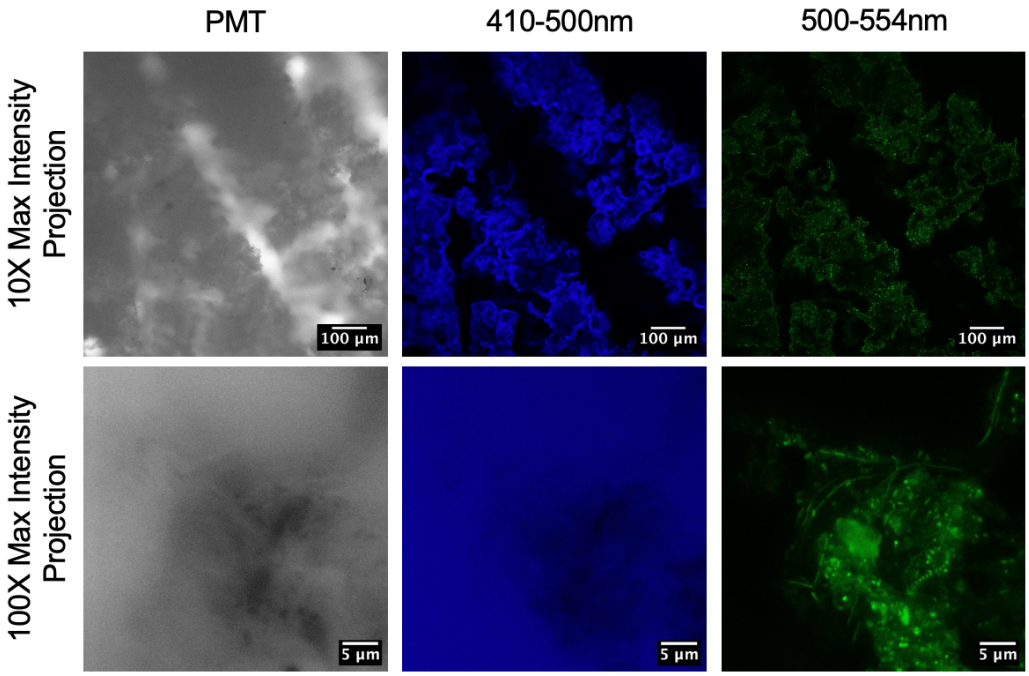

Figure C.5. Individual channel images of the 10X and 100X maximum intensity projections shown in Figure 4.17b

A p p e n d i x D

FREEZING PROFILES

Table D.1. Temperature, ramp, and soak inputs for columnar pore morphology through suspension-based freeze casting.

Columnar Pores (Suspension)					
Top			**Bottom**		
T (°C)	*Ramp (s)*	*Soak (s)*	*T (°C)*	*Ramp (s)*	*Soak (s)*
40	15	615	40	15	600
22.5	4200	1	6	15	1
5	3000	9999	-12	4320	1
-	-	-	-30	3086	9999
-	-	-	-	-	-
-	-	-	-	-	-
-	-	-	-	-	-
-	-	-	-	-	-

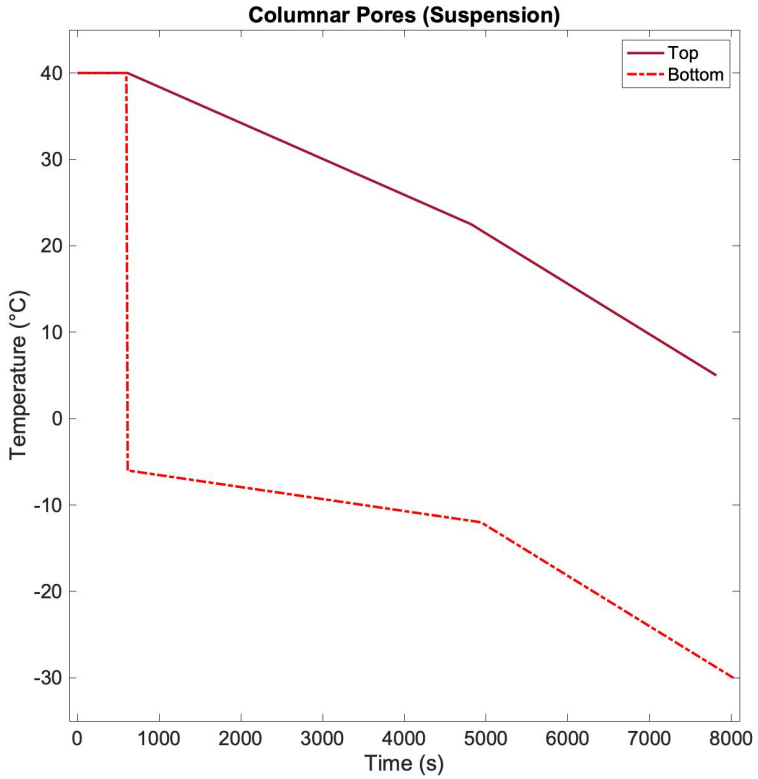

Figure D.1. Freezing profile to produce columnar pores through suspension-based freeze casting.

Table D.2. Temperature, ramp, and soak inputs for dendritic pore freezing profile.

Dendritic Pores					
Top			**Bottom**		
T (°C)	*Ramp (s)*	*Soak (s)*	*T (°C)*	*Ramp (s)*	*Soak (s)*
-	-	-	15	30	60
-	-	-	5	600	1
-	-	-	0	231	1
-	-	-	-5	187	1
-	-	-	-10	158	1
-	-	-	-15	143	1
-	-	-	-20	125	1
-	-	-	-30	222	9999

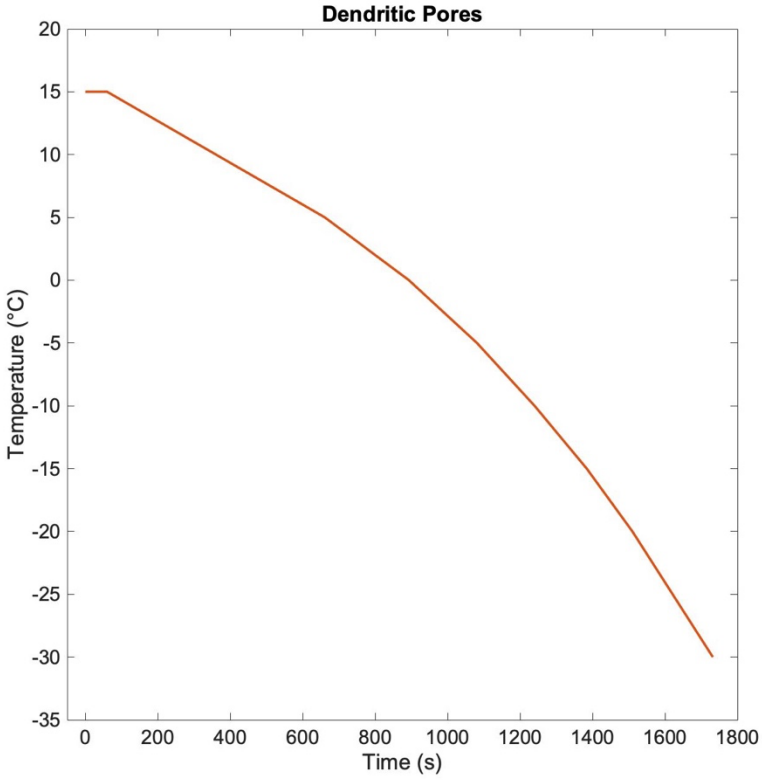

Figure D.2. Freezing profile to produce dendritic pores.

Table D.3. Temperature, ramp, and soak inputs for isotropic pore freezing profile.

Isotropic Pores					
Top			**Bottom**		
T (°C)	*Ramp (s)*	*Soak (s)*	*T (°C)*	*Ramp (s)*	*Soak (s)*
-	-	-	25	30	60
-	-	-	15	600	1
-	-	-	10	231	1
-	-	-	5	187	1
-	-	-	0	158	1
-	-	-	-5	143	1
-	-	-	-10	125	1
-	-	-	-20	222	9999

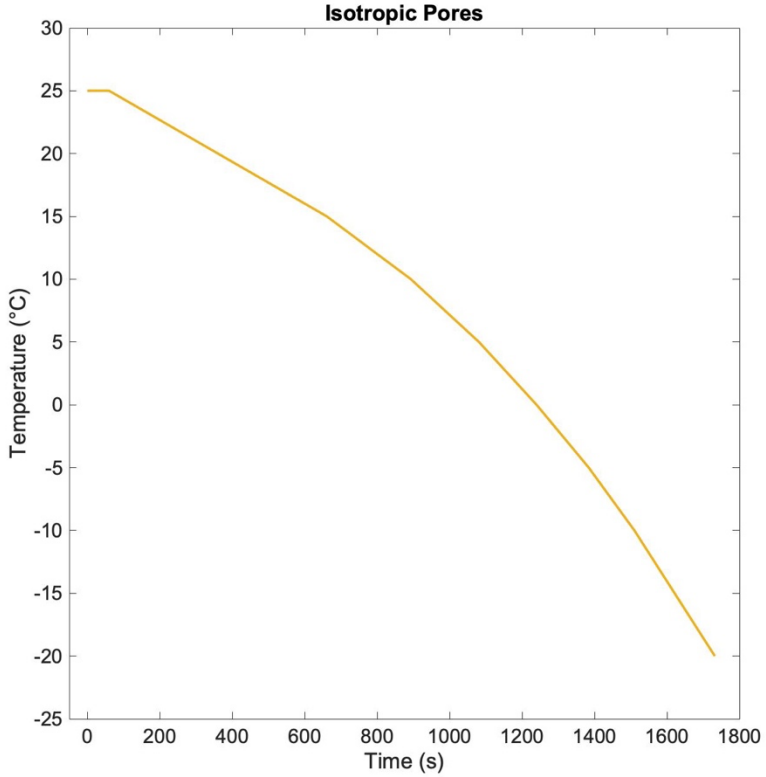

Figure D.3. Freezing profile to produce isotropic pores.

Table D.4. Temperature, ramp, and soak inputs for columnar pore morphology through solution-based freeze casting using coarsening.

Columnar Pores (Coarsened)					
Top			**Bottom**		
T (°C)	*Ramp (s)*	*Soak (s)*	*T (°C)*	*Ramp (s)*	*Soak (s)*
40	15	615	40	15	600
34	240	1	0	15	1
5	696	600	-15	300	1
4	420	9999	-25	300	1
4	1	9999	-30	75	861
-	-	-	4	120	3600
-	-	-	4	1	3600
-	-	-	-30	120	9999

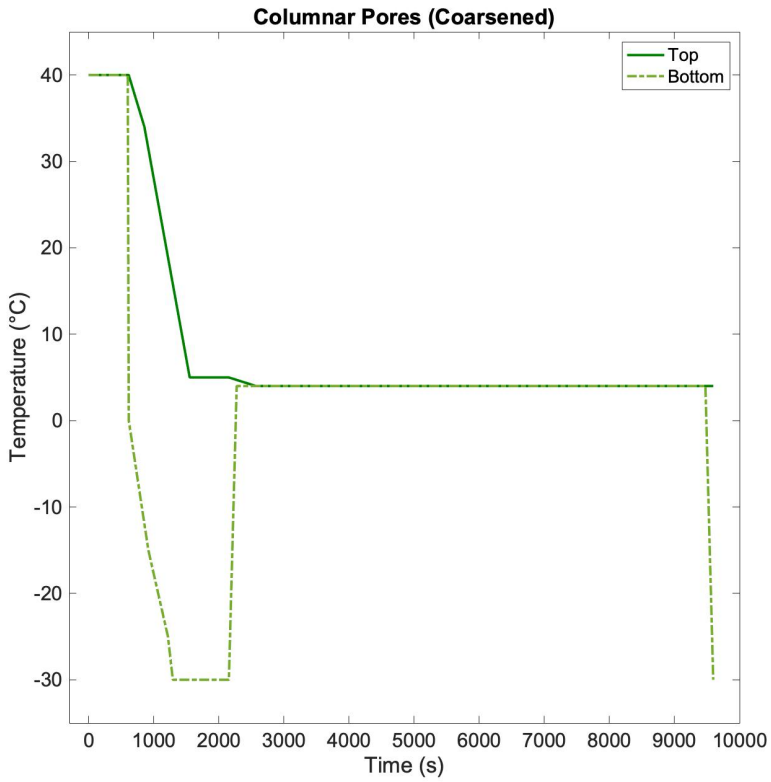

Figure D.4. Freezing profile to produce columnar pores through solution-based freeze casting and coarsening.

Table D.5. Temperature, ramp, and soak inputs for angled dendritic pore freezing profile.

Angled Dendritic Pores					
Top			**Bottom**		
T (°C)	*Ramp (s)*	*Soak (s)*	*T (°C)*	*Ramp (s)*	*Soak (s)*
-	-	-	15	30	60
-	-	-	10	455	1
-	-	-	5	227	1
-	-	-	-30	1061	9999
-	-	-	-	-	-
-	-	-	-	-	-
-	-	-	-	-	-
-	-	-	-	-	-

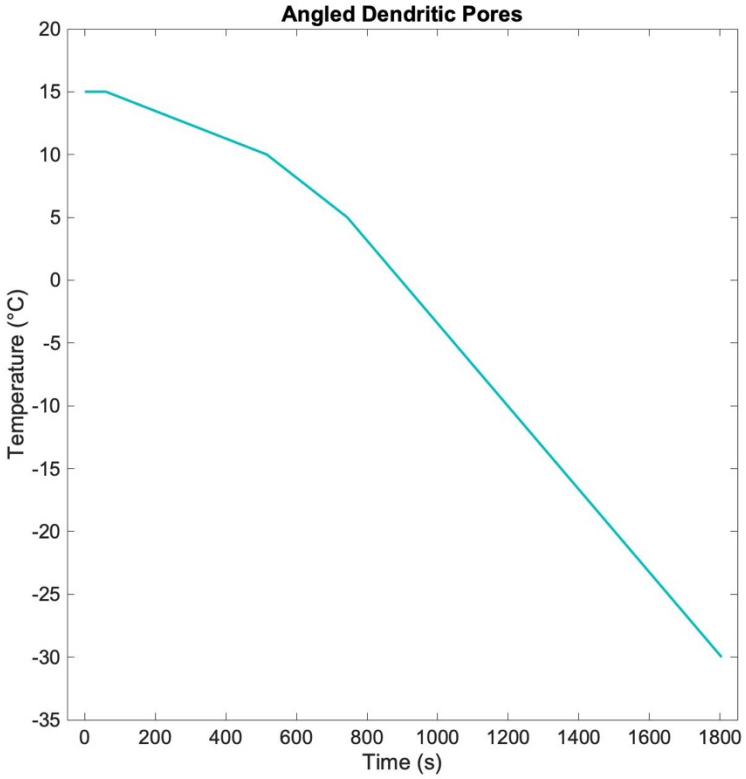

Figure D.5. Freezing profile to produce angled dendritic pores.

Table D.6. Temperature, ramp, and soak inputs for lamellar pore freezing profile.

Lamellar Pores					
Top			**Bottom**		
T (°C)	*Ramp (s)*	*Soak (s)*	*T (°C)*	*Ramp (s)*	*Soak (s)*
-	-	-	25	30	60
-	-	-	15	600	1
-	-	-	10	231	1
-	-	-	5	187	1
-	-	-	0	158	1
-	-	-	-10	286	1
-	-	-	-20	250	1
-	-	-	-30	222	9999

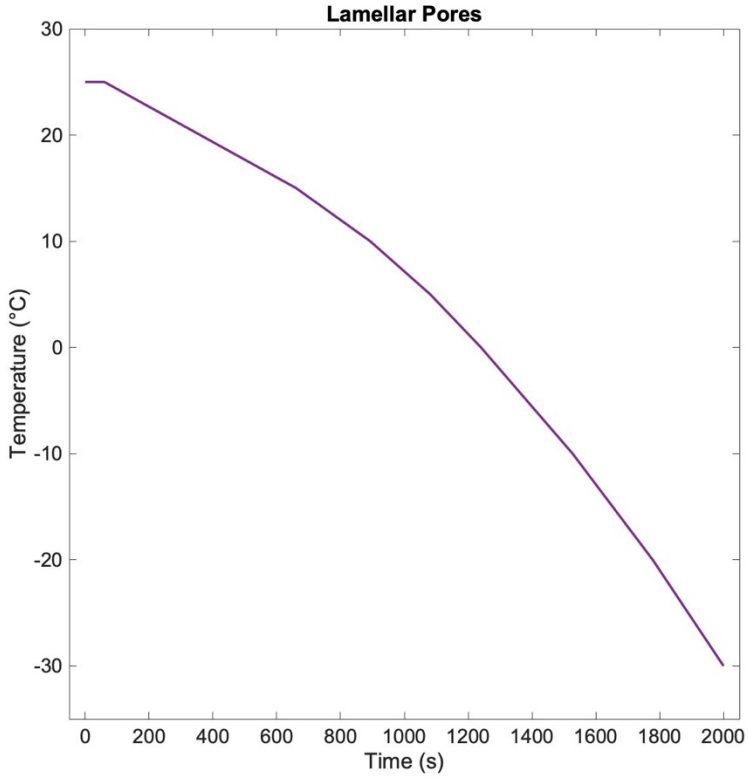

Figure D.6. Freezing profile to produce lamellar pores.